

ALMA MATER STUDIORUM  
UNIVERSITÀ DI BOLOGNA

---

---

Dottorato di Ricerca in Fisica  
Ciclo XXV

Settore Concorsuale di afferenza: 02/A1

Settore Scientifico disciplinare: FIS/04

MEASUREMENT OF THE DIFFERENTIAL CROSS  
SECTION OF  $t\bar{t}$  PAIRS IN  $pp$  COLLISION AT  
 $\sqrt{s} = 7\text{ TeV}$  WITH THE ATLAS DETECTOR AT THE  
LHC

Presentata da: Marino Romano

Coordinatore Dottorato:

Prof. Fabio Ortolani

Relatore:

Prof. Antonio Zoccoli

Correlatori:

Dott. Lorenzo Bellagamba

Dott. Graziano Bruni

---

---

Esame Finale - Anno 2013



---

## INTRODUCTION

The top quark is the heaviest known fundamental particle in nature, as well as the most recently discovered quark.

Its existence was suggested already in 1977 when its weak isospin partner, the  $b$ -quark, was discovered, and its mass was constrained from electroweak precision data in the following years. It was finally discovered in 1995 by the CDF and D0 experiments at the Fermilab Tevatron, a  $p\bar{p}$  collider at a centre-of-mass energy of  $\sqrt{s} = 1.8$  TeV. For 15 years the Tevatron has been the only place where top quarks were produced and studied directly. Since 2010 the top quark has been studied by both the ATLAS and CMS experiments at the Cern Large Hadron Collider (LHC), the world largest particle accelerator, colliding protons at a centre-of-mass energy of  $\sqrt{s} = 7$  TeV (and  $\sqrt{s} = 8$  TeV in 2012).

At hadron colliders the top quark can be produced in pairs ( $t\bar{t}$ ), via strong interaction, or singly, via electroweak processes, with the  $t\bar{t}$  production being dominant. In the Standard Model (SM) theoretical framework, top quarks are predicted to decay to a W-boson and a b-quark nearly 100% of the times. Events with a  $t\bar{t}$  pair can then be classified as “single-lepton”, “dilepton”,

---

or “all hadronic”, according to the decay of the two  $W$ -bosons: a pair of quarks or a lepton-neutrino pair. The most precise  $t\bar{t}$  production cross-section measurements both at the Tevatron and at the LHC colliders are performed selecting events in the single-lepton channel, combining a high branching ratio ( $\approx 30\%$  excluding the events with a  $\tau$  lepton) with the presence of a high  $p_T$  electron or muon allowing to trigger the events and to reduce the QCD multi-jet background.

The top-antitop production cross-section measurement at the LHC has been of central importance in the physics program of the two experiments during the past two years, for several reasons. Given these final states involving high energy jets, electrons, muons and missing transverse energy, measuring the  $t\bar{t}$  production cross-section is important to test the capability of the detector in reconstructing such complex signatures, which are also typical of many new physics processes. For the same reason  $t\bar{t}$  is an important background in many searches for new physics.

The uncertainties on the theoretical predictions on this measurement are now less than 10% and are in good agreement with the most recent measurements. In this scenario, considering also the rapidly increasing integrated luminosity, the focus is starting to switch to the “differential” measurements of the top properties, such as the cross section as function of the system kinematic variables. Comparing these kind of experimental measurements performed in different channels, allows a precision test of the predictions of perturbative QCD. New physics may also give rise to additional  $t\bar{t}$  production mechanisms or modifications of the top quark decay channels that can be discovered looking at the differential spectra, since the integrated cross section is already well-measured and compatible with the Standard Model prediction.

---

The analysis presented on this thesis is focused on the relative top-anti top production cross section  $1/\sigma \frac{d\sigma}{dX}$ <sup>1</sup> as a function of the mass, transverse momentum and rapidity of the system. The topology under study is the single-lepton channel. The analysis has been performed using a cut-based approach: events are been selected in order to reduce the background contribution and enhance the signal-over-background ratio. Once the reconstructed kinematic distribution are extracted, the cross section is calculated in the full phase space at the parton level via unfolding methods.

## Structure of the thesis

This thesis is divided in six chapters:

- in Chapter 1 a discussion on the current knowledge of the Standard Model and the top quark is presented;
- in Chapter 2 a brief description of the experimental apparatus (the collider and the detector) is presented;
- in Chapter 3 all the data and Monte Carlo samples used in this analysis are presented and discussed;
- the reconstructed object (i.e. the “ingredient” used in the analysis) are described in Chapter 4;
- the way the events are selected, the systematic uncertainties and the data/MC comparisons (control plots) are shown in Chapter 5;

---

<sup>1</sup>The relative, or normalized, differential cross section is affected by lower systematic errors, since many sources of uncertainty do not modify the shape of the reconstructed distributions, but only their normalization.

- 
- the actual measurement, and the final results, are then presented in Chapter 6.

Finally, in the conclusions, the summary of the analysis, as well as the open issues and plans for the future, are presented.

In appendix to this thesis, the data/MC comparisons using the Alpgen generators (Appendix A), the details on the break-down of the uncertainties (Appendix B) and a brief description of the measurement performed using the “two-tags selection (i.e. requiring at least two jets tagged as  $b$ -jets, Appendix C) are presented.

---

# CONTENTS

<b>Introduction</b>	<b>III</b>
<b>Contents</b>	<b>VII</b>
<b>1 The Top Quark</b>	<b>1</b>
1.1 The Standard Model of Particle Physics . . . . .	1
1.1.1 The Lagrangian of the Standard Model . . . . .	4
1.1.2 Fermion generations and mixings . . . . .	7
1.2 The top quark . . . . .	9
1.2.1 Top quark pair production . . . . .	10
1.2.2 Single top production . . . . .	14
1.2.3 Top quark pair decays . . . . .	16
1.2.4 Top quark mass . . . . .	19
<b>2 The LHC and the ATLAS experiment</b>	<b>23</b>
2.1 The Large Hadron Collider . . . . .	23
2.2 The ATLAS detector . . . . .	28
2.2.1 The magnet system . . . . .	30

## CONTENTS

---

2.2.2	The Inner Detector . . . . .	31
2.2.3	The calorimeters . . . . .	35
2.2.4	The Muon Spectrometer . . . . .	39
2.2.5	The luminosity detectors . . . . .	41
2.2.6	Trigger and data acquisition . . . . .	42
<b>3</b>	<b>Data and Monte Carlo samples</b>	<b>45</b>
3.1	Data samples . . . . .	45
3.2	Monte Carlo simulations . . . . .	47
3.2.1	Generation . . . . .	48
3.2.2	Simulation . . . . .	52
3.2.3	Monte-Carlo samples . . . . .	53
3.3	$t\bar{t}$ signal estimation . . . . .	58
3.4	Background estimation . . . . .	62
3.4.1	QCD background estimation . . . . .	64
3.4.2	$W$ +jets background normalization . . . . .	69
<b>4</b>	<b>Object definitions and selection</b>	<b>75</b>
4.1	Jets . . . . .	76
4.1.1	Jet reconstruction algorithms . . . . .	77
4.1.2	$b$ -tagging algorithms . . . . .	79
4.2	Electrons . . . . .	81
4.2.1	Electron reconstruction performance . . . . .	83
4.3	Muons . . . . .	85
4.3.1	Muon reconstruction performances . . . . .	88
4.4	Missing Transverse Energy . . . . .	91
4.4.1	$\cancel{E}_T$ reconstruction performance . . . . .	93
4.5	Trigger . . . . .	94

---

4.5.1	Electron trigger . . . . .	95
4.5.2	Muon trigger . . . . .	96
<b>5</b>	<b>Event selection and systematic uncertainties</b>	<b>101</b>
5.1	Selection cuts . . . . .	101
5.2	Systematic uncertainties . . . . .	102
5.2.1	Signal modeling . . . . .	103
5.2.2	Background modeling . . . . .	106
5.2.3	Detector modeling . . . . .	106
5.2.4	Luminosity . . . . .	109
5.3	Control plots . . . . .	109
5.3.1	Jet-related plots . . . . .	110
5.3.2	Lepton-related plots . . . . .	112
5.3.3	$\cancel{E}_T$ -related plots . . . . .	114
<b>6</b>	<b>Description of the measurement</b>	<b>117</b>
6.1	$t\bar{t}$ system reconstruction . . . . .	117
6.1.1	Performance of the fit . . . . .	120
6.1.2	Binning choice . . . . .	120
6.1.3	Reconstructed spectra . . . . .	124
6.2	Unfolding . . . . .	126
6.2.1	Simple matrix inversion . . . . .	128
6.2.2	Iterative Bayesian unfolding . . . . .	129
6.2.3	Single Value Decomposition . . . . .	130
6.2.4	Migration matrices and efficiencies . . . . .	131
6.2.5	Propagation of the uncertainties through the unfolding	136
6.2.6	Combination of the channels . . . . .	136
6.3	Results . . . . .	137

## CONTENTS

---

6.3.1	$\frac{1}{\sigma} \frac{d\sigma}{dM}$	138
6.3.2	$\frac{1}{\sigma} \frac{d\sigma}{dp_T}$	140
6.3.3	$\frac{1}{\sigma} \frac{d\sigma}{dY}$	146
<b>Conclusions</b>		<b>149</b>
<b>A Control plots with the Alpgen generator</b>		<b>153</b>
A.1	Jet-related plots	153
A.2	Lepton-related plots	154
A.3	$\cancel{E}_T$ -related plots	157
<b>B Uncertainties tables</b>		<b>159</b>
B.1	$\frac{1}{\sigma} \frac{d\sigma}{dm}$	160
B.2	$\frac{1}{\sigma} d\sigma/dp_T$	163
B.3	$\frac{1}{\sigma} d\sigma/dY$	165
<b>C Differential cross section using the two-tags selection</b>		<b>169</b>
C.1	Reconstructed spectra, efficiencies and migration matrices	170
C.2	Results	177
C.2.1	$\frac{1}{\sigma} \frac{d\sigma}{dM}$	177
C.2.2	$\frac{1}{\sigma} \frac{d\sigma}{dp_T}$	179
C.2.3	$\frac{1}{\sigma} \frac{d\sigma}{dY}$	181
<b>List of Figures</b>		<b>183</b>
<b>List of Tables</b>		<b>193</b>
<b>Bibliography</b>		<b>199</b>

---

---

# CHAPTER 1

---

## THE TOP QUARK

### 1.1 The Standard Model of Particle Physics

The interactions of the known fundamental spin-1/2 fermion constituents of matter, through the exchange of spin-1 gauge bosons, is successfully described by the Standard Model of elementary particle physics (SM). The fermions and gauge bosons included in the framework of the SM are listed in Fig. 1.1. Both quarks and leptons occur in pairs, differing by one unit of electric charge  $e = 1.60 \times 10^{-19}\text{C}$ , and are replicated in three generations with a strong hierarchy in mass. The top quark mass, for example, is measured to be five orders of magnitude larger than the mass of the electron. The origin of this flavor symmetry breaking and the consequent mass hierarchy are still not understood but can be accommodated in the SM, as shown in Sect. 1.1.1.

The SM is a particular quantum field theory, based on a set of fields corresponding to the known fermions and on the gauge symmetries  $SU(3)_c \otimes SU(2)_L \otimes U(1)_Y$ . It includes both the strong interaction and the electroweak

## Chapter 1. The Top Quark

Three Generations  
of Matter (Fermions)

	I	II	III	
mass→	2.4 MeV	1.27 GeV	171.2 GeV	0
charge→	$\frac{2}{3}$	$\frac{2}{3}$	$\frac{2}{3}$	0
spin→	$\frac{1}{2}$	$\frac{1}{2}$	$\frac{1}{2}$	1
name→	<b>u</b> up	<b>c</b> charm	<b>t</b> top	<b>γ</b> photon
	4.8 MeV	104 MeV	4.2 GeV	0
	$-\frac{1}{3}$	$-\frac{1}{3}$	$-\frac{1}{3}$	0
	$\frac{1}{2}$	$\frac{1}{2}$	$\frac{1}{2}$	1
Quarks	<b>d</b> down	<b>s</b> strange	<b>b</b> bottom	<b>g</b> gluon
	<2.2 eV	<0.17 MeV	<15.5 MeV	91.2 GeV
	0	0	0	0
	$\frac{1}{2}$	$\frac{1}{2}$	$\frac{1}{2}$	1
	<b>ν<sub>e</sub></b> electron neutrino	<b>ν<sub>μ</sub></b> muon neutrino	<b>ν<sub>τ</sub></b> tau neutrino	<b>Z</b> weak force
	0.511 MeV	105.7 MeV	1.777 GeV	80.4 GeV
	-1	-1	-1	±1
	$\frac{1}{2}$	$\frac{1}{2}$	$\frac{1}{2}$	1
Leptons	<b>e</b> electron	<b>μ</b> muon	<b>τ</b> tau	<b>W<sup>±</sup></b> weak force

Bosons (Forces)

**Figure 1.1** – The known fundamental fermions and gauge bosons and their properties: mass, charge and spin.

interaction theories. The gravitational force, on the contrary, cannot be included in the current formulation of this framework. In any case its strength is negligible compared to that of the other interactions at the typical energy scales of the particle physics experiments, since quantum gravity effects arise at Planck scale ( $\Lambda_{Planck} \approx 10^{19}$  GeV).

The theory of the strong interactions, coupling three different “color” charges carried by the quarks and the eight mass-less gauge bosons (gluons), is called Quantum Chromodynamics (QCD), and is based on the gauge group  $SU(3)_C$  [1, 2]. This is an exact symmetry, and the gluons carry both a color and an anti-color charge. At increasingly short distances (or large relative momenta), the interaction becomes weaker and weaker (asymptotic freedom), making possible a perturbative treatment.

Via the strong interaction, quarks can form bound color-singlet states called hadrons, consisting of either a quark and an anti-quark (mesons) or three quarks (baryons). The fact that only color-neutral states and no free quarks are observed in nature is referred to as the “confinement” of quarks in hadrons. This has the important experimental consequence that quarks

produced in high energy particles interactions manifest themselves as collimated showers of hadrons called “jets”. The energy and direction of a jet are correlated to the energy and direction of its parent quark. The process by which the quark evolves into a jet can be divided in two phases: the parton shower (the analogue to the QED bremsstrahlung radiation), which can be perturbatively calculated, and the fragmentation process, which is a non-perturbative process modeled using Monte Carlo (MC) techniques.

Due to its large mass, the top quark decays faster than the typical hadronization time of the QCD ( $\Gamma_t \gg \Lambda_{QCD}$ ), being the only quark that does not form bound states. Its decay offers the unique possibility to study the properties of an essentially bare quark. Top quark pair production, furthermore, is one of the dominant backgrounds in many BSM theories that include gravity (such as the SuGra extensions of the Supersymmetry models). A detailed study of the top production properties is therefore mandatory when performing studies on these models.

The theory of electroweak interactions was developed by Glashow, Weinberg and Salam [3, 4, 5] and is based on the  $SU(2)_L \otimes U(1)_Y$  gauge group of the weak left handed isospin  $T$  and hypercharge  $Y$ . Since the weak ( $V - A$ ) interaction only couples to left-handed particles, the fermion fields  $\Psi$  are decomposed into left-handed and right-handed fields  $\Psi_{L,R} = 1/\sqrt{2}(1 \mp \gamma_5)\Psi$ , arranged in weak isospin doublets ( $T = 1/2$ ) and singlets ( $T = 0$ ):

$$\text{first family: } \begin{pmatrix} \nu_e \\ e^- \end{pmatrix}_L \begin{pmatrix} u \\ d \end{pmatrix}_L \quad e_R^- \quad u_R \quad d_R$$

$$\text{second family: } \begin{pmatrix} \nu_\mu \\ \mu^- \end{pmatrix}_L \begin{pmatrix} c \\ s \end{pmatrix}_L \quad \mu_R^- \quad c_R \quad s_R$$

## Chapter 1. The Top Quark

---

$$\text{third family: } \begin{pmatrix} \nu_\tau \\ \tau^- \end{pmatrix}_L \begin{pmatrix} t \\ b \end{pmatrix}_L \tau_R^- t_R b_R.$$

Gauge invariance prevents the existence of explicit mass terms for the gauge bosons and the fermions. A minimal way to introduce these observed masses is to implement a spontaneous electroweak symmetry breaking (EWSB) at energies around the mass scale of the  $W$  and  $Z$  bosons, often referred to as the ‘‘Higgs mechanism’’ [6], by introducing an  $SU(2)$  doublet of complex scalar fields  $\phi = (\phi_+, \phi_0)^T$ .

### 1.1.1 The Lagrangian of the Standard Model

Once the gauge symmetries and the fields with their quantum numbers are provided, the Lagrangian of the Standard Model is fixed by requiring it to be gauge-invariant, local, and renormalizable. The SM Lagrangian can be factorized in the sum of four pieces:

$$\mathcal{L}_{SM} = \mathcal{L}_{Gauge} + \mathcal{L}_{Fermions} + \mathcal{L}_{Higgs} + \mathcal{L}_{Yukawa}. \quad (1.1)$$

The first piece describes the kinetic energy of the gauge bosons and their self-couplings:

$$\mathcal{L}_{Gauge} = -\frac{1}{2} \text{Tr } \mathbf{G}^{\mu\nu} \mathbf{G}_{\mu\nu} - \frac{1}{8} \text{Tr } \mathbf{W}^{\mu\nu} \mathbf{W}_{\mu\nu} - \frac{1}{4} \text{Tr } B^{\mu\nu} B_{\mu\nu}. \quad (1.2)$$

The second is the matter Lagrangian:

$$\begin{aligned} \mathcal{L}_{Fermions} = & i\bar{Q}_L^i \gamma^\mu D_\mu Q_L^i + i\bar{u}_R^i \gamma^\mu D_\mu u_R^i + \bar{d}_R^i \gamma^\mu D_\mu d_R^i + \\ & i\bar{L}_L^i \gamma^\mu D_\mu L_L^i + i\bar{e}_R^i \gamma^\mu D_\mu e_R^i, \end{aligned} \quad (1.3)$$

where  $Q$  and  $L$  are the quark and lepton doublets,  $u_R, d_R, e_R$  are the singlets. The sum over the three generations is implied. This formula contains the kinetic energy of the fermions and their interactions with the gauge fields, which are contained in the covariant derivative  $D_\mu$ , whose most complete form is:

$$D_\mu = \partial_\mu + ig_s \mathbf{G}_\mu + \frac{ig}{2} \mathbf{W}_\mu + \frac{ig'}{6} B_\mu. \quad (1.4)$$

This definition can be applied only to the isospin doublets  $Q^i$ , since the  $L^i$  doublets do not couple with the  $G$  field and the singlets don't couple with the  $W$  field.

The next term is the Higgs Lagrangian, given by:

$$\mathcal{L}_{Higgs} = D_\mu \phi^\dagger D_\mu \phi + \mu^2 \phi^\dagger \phi - \lambda (\phi^\dagger \phi)^2. \quad (1.5)$$

This piece contains the kinetic energy of the Higgs field, its gauge interactions, and the Higgs potential with its self-interactions Fig. 1.2. The quartic term, must be positive in order to make the Higgs potential lower bounded.

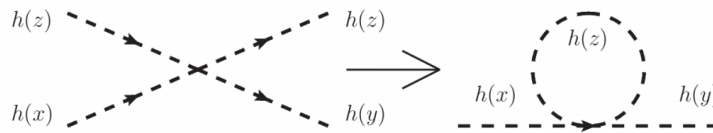


**Figure 1.2** – Higgs self-interactions Feynman diagrams.

The sign of the quadratic term is chosen such that the Higgs field has a non-zero vacuum-expectation value in the Higgs-field space given by

$$\langle \phi_0 \rangle = \frac{\mu}{2\lambda} \equiv \frac{v}{2}, \text{ with } v \approx 246 \text{ GeV}. \quad (1.6)$$

Gauge symmetries allow a specific expansion of the Higgs field around its

## Chapter 1. The Top Quark

---

minimum

$$\phi = \begin{pmatrix} 0 \\ \frac{v+H}{\sqrt{2}} \end{pmatrix}. \quad (1.7)$$

In this form, the  $D_\mu\phi^\dagger D_\mu\phi$  term in (1.5) introduces explicit mass terms for the gauge bosons. In particular, the masses of the physical  $W$  and  $Z$ -bosons can be written as:

$$\begin{aligned} M_W &= g\frac{v}{2} \\ M_Z &= \sqrt{g^2 + g'^2} v. \end{aligned} \quad (1.8)$$

The last piece of the Lagrangian is the Yukawa interaction of the Higgs field with the fermions:

$$\mathcal{L}_{Yukawa} = -\lambda_u^{ij} \bar{Q}_L^i \epsilon \phi^* u_R^j - \lambda_d^{ij} \bar{Q}_L^i \epsilon \phi^* d_R^j - \lambda_e^{ij} \bar{L}_L^i \epsilon \phi^* e_R^j + h.c., \quad (1.9)$$

where  $\epsilon = i\sigma_2$  is the totally antisymmetric tensor required to ensure each term to be electrically neutral and  $-\lambda_{u,d,e}^{ij}$  are  $3 \times 3$  complex matrices. They don't need to be diagonal, so their general form can allow mixings between the different fermion generations.

Using the expression of the Higgs field in (1.7) in the Yukawa Lagrangian (1.9), the masses of the fermions appear in the form

$$m_f = y_f \frac{v}{\sqrt{2}}, \quad (1.10)$$

where  $y_f$  represents the Yukawa coupling relative to the fermion  $f$  mass eigenstate, obtained by diagonalizing the Yukawa matrix  $\lambda^{ij}$ .

Since the top quark is the heaviest among the fermions, it is character-

ized by the largest Yukawa coupling,  $y_t \approx 1$ . This makes the top quark an important probe to access information on both the Higgs sector and new physics.

### 1.1.2 Fermion generations and mixings

As shown in (1.9) and (1.10), fermion families can mix. In the quark sector, the mixing between the weak eigenstates of the down-type quarks  $d'$ ,  $s'$  and  $b'$ , and the corresponding mass eigenstates  $d$ ,  $s$  and  $b$ , is described by the Cabibbo-Kobayashi-Maskawa (CKM) matrix [7, 8]:

$$\begin{pmatrix} d' \\ s' \\ b' \end{pmatrix} = \begin{pmatrix} V_{ud} & V_{us} & V_{ub} \\ V_{cd} & V_{cs} & V_{cb} \\ V_{td} & V_{ts} & V_{tb} \end{pmatrix} \begin{pmatrix} d \\ s \\ b \end{pmatrix} \quad (1.11)$$

Since the CKM matrix is not diagonal, charged current weak interactions can cause transitions between quark generations with coupling strengths with the  $W^\pm$  boson given by the above matrix elements. By convention, the mixing takes place between down-type quarks only, while the up-type mass matrix is diagonal.

This unitary matrix has diagonal entries close to unity and off-diagonal entries that are around 0.2 between the first and second generation, around 0.04 between the second and third generation and even smaller for the transition of the first to the third generation [9]. In particular, the matrix element  $V_{tb}$  is constrained indirectly making use of the unitarity of the CKM matrix and assuming three quark generations to be very close to 1:  $0.9990 < |V_{tb}| < 0.9992$  at 90% confidence level (C.L.).<sup>1</sup> This fact forces the top quark to couple

---

<sup>1</sup>Recently, direct measurements of  $V_{tb}$  have been made by CDF [10] and D0 [11] first and then ATLAS [12] and CMS [13] through the observation of the single top production.

## Chapter 1. The Top Quark

---

almost exclusively to bottom quarks. This affects both the top quark production, suppressing the electroweak single top production mechanisms with respect to the pair production one, and its decay, and makes the presence of  $b$ -quark jets in the final state a strong experimental signature in top searches.

In the lepton sector, if the neutrinos are assumed to be mass-less, such a mixing does not take place. However, from experimental evidence [9], neutrinos also have mass, which has led, among other things, to the introduction of an analogue leptonic mixing matrix, the Pontecorvo-Maki-Nakagawa-Sakata (PMNS) matrix [14, 15]. For the purpose of this thesis, a mixing in the lepton sector would have no effect, and therefore a mass-less neutrino SM formulation is assumed.

In summary, the SM is a unitary, renormalizable theory, that can be used to perturbatively calculate processes at high energies. It incorporates 18 parameters that have to be provided through experimental measurements:

- 9 Yukawa couplings for the fermion masses;
- 4 parameters for the CKM mixing matrix;
- 3 coupling constants  $g_S$ ,  $g$ ,  $g'$  for  $SU(3)_C$ ,  $SU(2)_L$  and  $U(1)_Y$ , respectively;
- 2 parameters from the EWSB:  $v$  and  $m_H$ .

At the currently accessible energy scales, the SM describes successfully the interactions of fundamental fermions and gauge bosons. Its predictions have been verified at recent colliders (SPS, LEP, Tevatron and LHC), with very high precision. Recently, ATLAS and CMS found a strong evidence of the presence of a Higgs-like boson with a mass around 126 GeV [16, 17].

---

Those measurements are in good agreement with the indirect determination, but suffer of larger uncertainty.

## 1.2 The top quark

As shown in Fig. 1.1, the top quark is the heaviest of the quarks, significantly heavier than the other quark in its generation, the bottom quark. Once the bottom quark was experimentally discovered in 1977, the existence of a charge- $2/3$  quark in the third quark generation was expected because the Standard Model is not a renormalizable gauge theory in the absence of the top quark. Diagrams containing so-called “triangle anomalies” like the one shown in Fig. 1.3, where an axial-vector current couples to two vector currents, cancel their contribution to any process, and thus avoid breaking the renormalizability of the SM, only if the sum of electric charges of all fermions circulating in the triangular loop is zero:  $\sum Q = -1 + 3 \times [2/3 + (-1/3)] = 0$  where  $-1$  is the electric charge of leptons, and  $2/3$ ,  $1/3$  are the charges of up- and down-type quarks, while the additional factor of three accounts for the three colors of each quark. It is evident that each complete generation of left-handed fermions has a zero sum of electric charges, while an incomplete third generation -one with a tau, a tau neutrino, three b-quarks, and no up-type partners of the b-quarks would contribute a non-zero total charge: triangle anomalies would thus make the SM non-renormalizable, hence useless. The top quark was eventually observed with the collision energies reached at the Tevatron collider. The top quark was the last quark discovered by both the CDF [18] and D0 [19] collaborations in 1995.

The top quark is special not only due to its large mass, but also due to its short lifetime. This means a free top quark produced in a collision decays before it hadronizes, i.e. there are no bound state hadrons made of top quarks. This allows to experimentally test the properties of the bare top quark itself through its decay products without diluting information in the hadronization process.

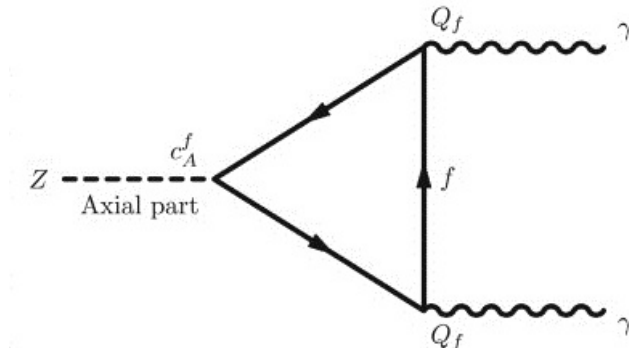


**Figure 1.3** – Feynman diagram leading to a triangular anomaly.

As the properties of the top quark are precisely predicted by the Standard Model, top quark physics provides a sensitive probe of the validity of the Standard Model and a tool to indirectly learn about the Higgs boson and to potentially discover physics beyond the Standard Model.

Studying top quark pair production is only possible in the data taken by the CDF and D0 experiments at the Tevatron accelerator and by the current experiments at the LHC, which can be considered as a “top quark factory” due to the high rate of top quark production ( $\approx 820000$  top-anti top pairs produced in 2011).

### 1.2.1 Top quark pair production

In  $p\bar{p}$  or  $pp$  collisions, top quarks can be produced individually or in pairs. The pair production occurs via the strong interaction. The leading order processes for the  $t\bar{t}$  production in the gluon fusion and quark anti-quark annihilation are shown in Fig. 1.4. Some examples of NLO diagrams are shown in Fig. 1.5. The relative contribution of these diagrams depends on the parton distribution functions (PDF). The PDFs describe the momentum distribution of the quarks and gluons that constitute the protons [20]. Each parton  $i$  carries a momentum fraction  $x_i$  in the hadron  $A$  and its momentum

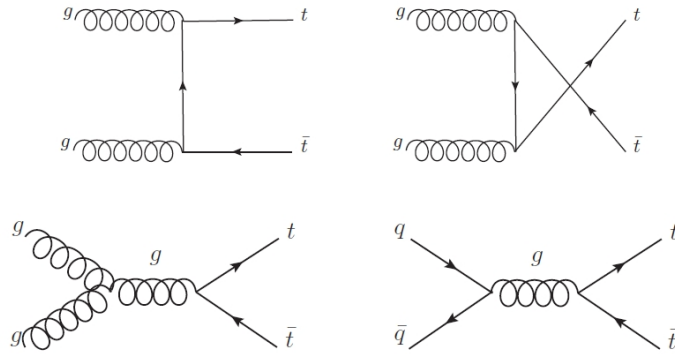


**Figure 1.4** – Leading-order Feynman diagrams for top-antitop pair production via gluon fusion processes and the quark-anti-quark annihilation process.

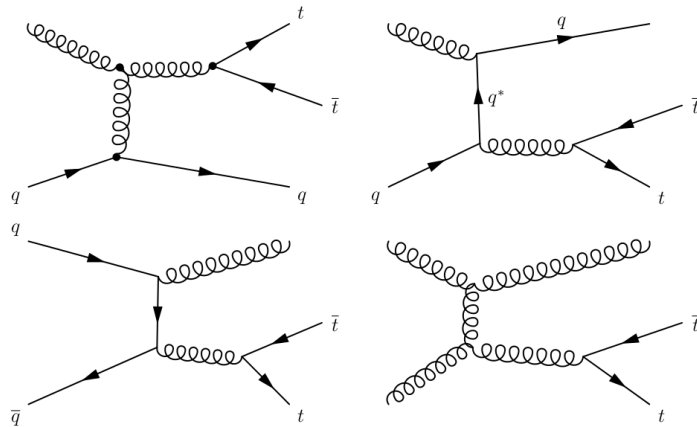


**Figure 1.5** – Examples of next-to-leading-order Feynman diagrams for top-antitop pair production via gluon fusion processes and the quark-anti-quark annihilation process.

## Chapter 1. The Top Quark

---

is given by  $p_i = x_i p_A$ . The cross sections are calculated as a convolution of the two PDFs  $f_{i/A}(x_i, \mu^2)$  and  $f_{j/B}(x_j, \mu^2)$  for the colliding hadrons ( $A, B$ ) and the factorized hard parton-parton cross section  $\hat{\sigma}_{ij}$ :

$$\sigma^{AB \rightarrow t\bar{t}+X}(\hat{s}, m_t) = \sum_{i,j=q,\bar{q},g} \int dx_i dx_j f_{i/A}(x_i, \mu_F^2) f_{j/B}(x_j, \mu_F^2) \hat{\sigma}^{ij \rightarrow t\bar{t}}(\hat{s}, m_t^2, \alpha_s(\mu_R^2), \mu_R^2). \quad (1.12)$$

The variable  $\hat{s}$  represents the square of the center-of-mass energy of the colliding partons  $\hat{s} = (p_i + p_j)^2 = (x_i p_A + x_j p_B)^2$ . The sum runs over all pairs of partons ( $i, j$ ) that contribute to the process. The PDF  $f_{i/A}(x_i, \mu_F^2)$  describes the probability density for finding a parton  $i$  inside the hadron  $A$  carrying a momentum fraction  $x_i$ .

The PDFs and  $\hat{\sigma}_{ij}$  have a residual dependence on the factorization and renormalization scales due to uncalculated higher orders [21]: the scale at which  $f_{i/A}$  and  $f_{j/B}$  PDFs are evaluated is the factorization scale ( $\mu_F^2$ ); the scale at which  $\alpha_s$  is evaluated is the renormalization scale ( $\mu_R^2$ ), and accounts for divergences coming from loop diagrams. Since both scales are to some extent arbitrary parameters they are chosen to be equal and in the case of top quark production, one typically evaluates the cross sections at  $\mu = m_t$ . The changes when varying  $\mu$  between  $m_t/2$  and  $2m_t$  are usually quoted as an indicative theoretical uncertainty due to unknown higher order contributions.

The PDFs are determined from fits to deep-inelastic-scattering (DIS) cross section measurements performed by a variety of experiments. The fits to the DIS data are performed by a number of different collaborations and are made available as software packages. Common choices are the MRST [22] and CTEQ [23] PDF fits.

The total cross section of top quark pair production has a significant dependence on the top quark mass and on the center-of-mass energy of the

colliding hadrons as shown in Fig. 1.6.

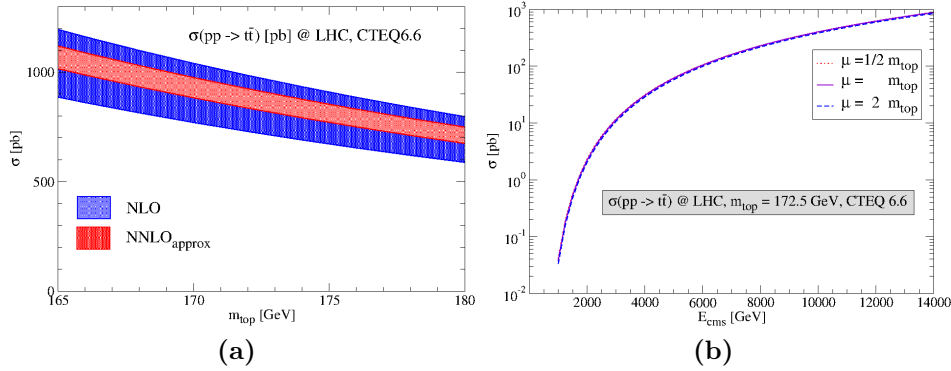


**Figure 1.6** – (a):  $t\bar{t}$  production cross section as a function of top mass at NLO (blue band) and NNLO (red band) in  $pp$  collisions at  $\sqrt{s} = 7$  TeV and (b):  $t\bar{t}$  production at the LHC as a function of the center of mass energy  $E_{cms}$  for  $m_t = 172.5$  GeV and for three different scales  $\mu = m_t/2, m_t, 2m_t$  [24]

The increase in rate shown in Fig. 1.6b can be understood by considering the structure of the proton. The proton is composed of three valence quarks (two up quarks and one down quark) bound together by gluons. The probability of finding a gluon with fraction  $x$  of the proton momentum grows extremely rapidly with decreasing  $x$ , as shown in Fig. 1.7. At threshold for the  $t\bar{t}$  production at Tevatron ( $\sqrt{s} \approx 2$  TeV), each of the two initial partons must carry a large fraction  $x \approx 0.2$  of the proton momentum, so the  $t\bar{t}$  production is mostly (80-90%) from collisions between valence quarks. At the LHC, the initial partons only need a small fraction  $x \approx 0.02$  of the proton momentum, so  $t\bar{t}$  production is mostly (80-90%) from collisions between gluons.

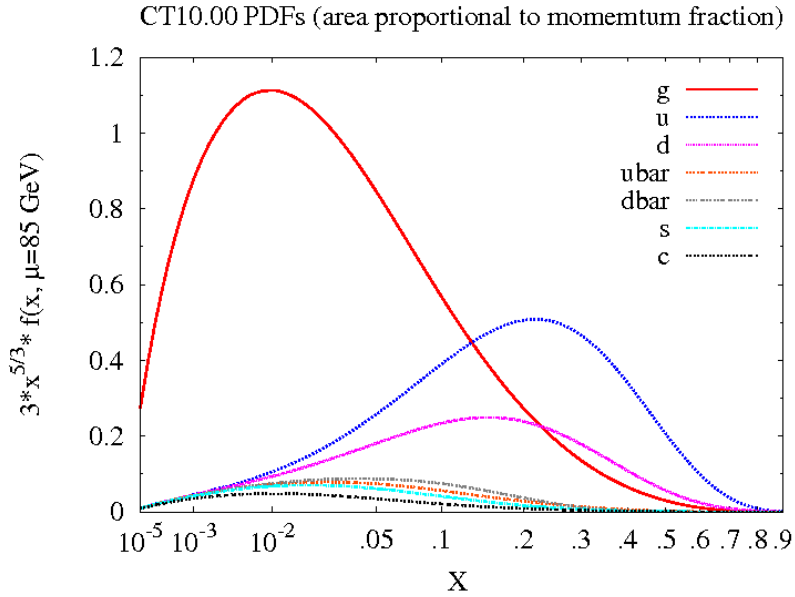


**Figure 1.7** – PDFs of quarks and gluons inside the proton, using CT10 parametrization with  $\mu_f = 80 \text{ GeV}$ [25].

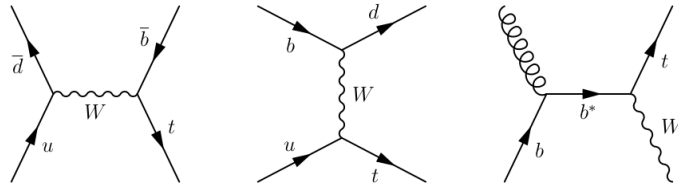


**Figure 1.8** – Single top production channels at leading order.

### 1.2.2 Single top production

Top quarks can also be produced as single quarks in electroweak interactions in  $pp$  and  $p\bar{p}$  collisions. Three different mechanisms contribute to single top quark production and their leading-order Feynman diagrams are shown in Fig. 1.8. The timelike process ( $s$ -channel) produces a bottom quark together with the single top quark, while in the spacelike production ( $t$ -channel) an additional, mostly light flavor, quark is produced. The third production mechanism is the production of a single top quark in association with an

on-shell (real)  $W$  boson ( $Wt$ -channel). In this channel there is an issue with the correct definition of the  $Wt$  cross section itself. At NLO and beyond there is a potentially large interference with top quark pair production, as shown in Fig. 1.9. However, it has been shown [26, 27] that this problem can be bypassed with particular kinematic cuts that suppress the  $t\bar{t}$  background in this interference, making possible a definition for the  $Wt$  production cross section.

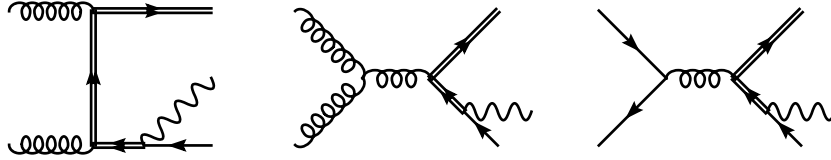


**Figure 1.9** – Examples of diagrams contributing to  $Wt$  production at NLO, in which a top-antitop pairs is produced with one of them decaying in  $Wb$ .

The first observation of single top quark production was achieved by the Tevatron experiments CDF and D0 in 2009 [10, 11] and was only possible applying several multivariate analysis techniques due to the low cross sections of the processes and large background contamination.

While at the typical Tevatron energies the  $Wt$ -channel has a negligible contribution to the combined single top quark production cross section, the contributions from the three production mechanisms are significantly different at the LHC. The spacelike production dominates, with major additional contributions from the  $Wt$ -channel and only minor contribution from the timelike production. The expected cross sections at  $\sqrt{s} = 7$  TeV are shown in Tab. 1.1.

Channel	$\sigma$ [pb]
$t$ -channel	$64.57 \pm 1.33(\text{scale})^{+1.38}_{-0.68}(\text{PDF})$
$Wt$	$15.74 \pm 0.40(\text{scale})^{+0.66}_{-0.68}(\text{PDF})$
$s$ -channel	$4.63 \pm 0.07(\text{scale})^{+0.12}_{-0.10}(\text{PDF})$

**Table 1.1** – Expected single top quark production cross sections in different channels at a center-of-mass energy of 7 TeV, given by approximate NNLO calculation by Kidonakis [28, 29, 30].

### 1.2.3 Top quark pair decays

Due to its extremely short life time, only the top quark decay products can be measured by the detectors. In the Standard Model, the only two-body decays of the top quark which are possible to lowest order are  $t \rightarrow b(s, d)W$ . Their rates are proportional to the squares of the CKM matrix elements  $|V_{tq}|^2$ .

The total decay width  $\Lambda_t$  of the top quark is given by the sum of the widths of these three decay modes. The analysis of data from weak decays of hadrons yields  $0.9990 < |V_{tb}| < 0.9992$  at 90% C.L., using the unitarity of the CKM matrix [9]. This implies that the total decay rate is completely dominated by  $t \rightarrow bW$ , as shown in Tab. 1.2, therefore the other decay channels are not considered in the following discussion.

Process	BR
$t \rightarrow bW$	0.998
$t \rightarrow sW$	$1.9 \times 10^{-3}$
$t \rightarrow dW$	$\sim 10^{-4}$

**Table 1.2** – Top decay branching ratios in the SM quarks.

In the Standard Model, including first order QCD corrections and neglecting terms of order  $m_b^2/m_t^2$ ,  $\alpha_s^2$  and  $(\alpha_s^2/\pi)m_W^2/m_t^2$ , the top quark total width

is [31]:

$$\Gamma_t = \frac{G_F m_t^3}{8\pi\sqrt{2}} |V_{tb}|^2 \left(1 - \frac{m_W^2}{m_t^2}\right)^2 \left(1 + 2\frac{m_W^2}{m_t^2}\right) \left[1 - \frac{2\alpha_s}{3\pi} \left(\frac{2\pi^2}{3} - \frac{5}{2}\right)\right], \quad (1.13)$$

where  $G_F = 1.167 \times 10^{-5} \text{ GeV}^{-2}$  is the Fermi constant.

The world average for the top decay width  $\Gamma_t = 1.99_{-0.55}^{+0.69} \text{ GeV}$  is compatible with the value predicted by (1.13)  $\Gamma_t = 1.29 \text{ GeV}$  assuming  $m_t = 171 \text{ GeV}$  and  $\alpha_s(M_Z) = 0.118$  [9].

Since the top quark decays almost exclusively to a  $W$ -boson and a  $b$ -quark, the  $t\bar{t}$  final state is determined by the decays of the two  $W$ -bosons from  $t$  and  $\bar{t}$ . In Fig. 1.10 the Feynman diagrams of  $t$  and  $\bar{t}$  quark decays are shown.

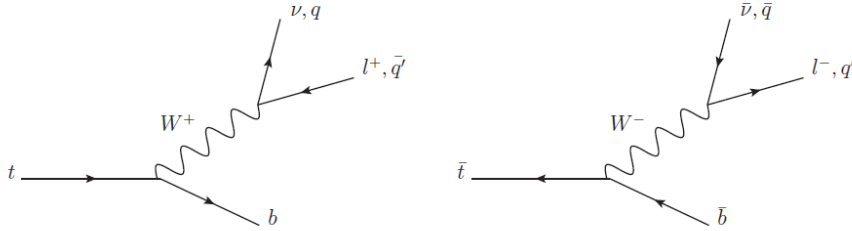


**Figure 1.10** – Top and anti-top decay chains.

$W$  bosons decay into either a pair of quarks, or into a lepton and a neutrino. A  $W$  boson hadronically decays into  $ud$  and  $cs$  pairs with three color degrees of freedom. The final states with  $cd$  and  $us$  are Cabibbo-suppressed. As a result, there are six hadronic final states for  $W$  boson decay. Furthermore, there are three additional final states from leptonically decaying  $W$  bosons, which decay into an electron, a muon or a tau lepton with corresponding flavored neutrinos. Counting both decay modes, there are nine possible  $W$  boson final states which are summarized in Tab. 1.3

The final states for the  $t\bar{t}$  events can be divided into three classes depending

Decay mode	Fraction
$W^\pm \rightarrow e^\pm \nu_e$	1/9
$W^\pm \rightarrow \mu^\pm \nu_\mu$	1/9
$W^\pm \rightarrow \tau^\pm \nu_\tau$	1/9
$W^\pm \rightarrow l^\pm \nu_l$	$3 \times 1/9 = 1/3$
$W^\pm \rightarrow q\bar{q}$	2/3

**Table 1.3** –  $W$  boson decay modes.

on the decay modes of two  $W$  bosons: dilepton mode, single lepton mode, full hadronic mode.

**Dilepton mode** In this channel both  $W$  bosons decay leptonically and the events consist of two oppositely charged leptons, two  $b$ -quarks and large missing transverse energy due to neutrinos in the final state. This is the cleanest channel from the background contamination point of view, since there are not many processes with two high transverse momentum leptons in the final state and significant missing transverse momentum. However, the presence of two neutrinos make the full reconstruction of the final state impossible and the branching ratio of the process is relatively small compared with other channels. It is only **10.3%** of the total which is sliced more finely into three channels with two same flavor leptons, each with a 1.2% branching fractions ( $ee$ ,  $\mu\mu$ ,  $\tau\tau$ ) and three channels with two different flavor leptons, each with 2.4% branching fraction ( $e\mu$ ,  $e\tau$ ,  $\mu\tau$ ). Experimentally only two leptons, electron and muon, can be directly observed. Due to its short life time, only the decay products of the tau lepton can be observed.

**Single-lepton mode** Here one  $W$  boson decays into leptons and the other decays into quarks. The final state is characterized by one lepton, two  $b$ -quarks, two light quarks from the hadronic  $W$  decay and relatively large

missing transverse energy. The branching ratio of this channel is quite high, **43.5%**, however at the same time the signal to background ratio is not so high as for the dilepton channel. In spite of the presence of one high transverse momentum lepton and quite large  $\cancel{E}_T$ , the processes as QCD or  $W$  boson production contribute to this channel as a not negligible source of background.

**Full hadronic mode** In this channel both  $W$  bosons decay hadronically.

The channel is characterized by the presence of two high- $p_T$   $b$ -quarks and four light quarks in the final state. This is the only channel where all final state constituents are available to be observed by the detector and the branching ratio is the highest, **46.2%**, but the lack of any high- $p_T$  lepton in the final state makes it difficult to suppress the contribution from background processes such as QCD multi-jet production.

#### 1.2.4 Top quark mass

The top quark mass,  $m_t$ , is a free parameter of the Standard Model and must be determined experimentally. A precise determination of  $m_t$  is important since quantum loops including top quarks induce large corrections to theory predictions for many precision electroweak observables, including the mass of the Higgs boson.

All electroweak quantities (mass, width and couplings of the  $W$  and the  $Z$  boson) depend in the SM only on five parameters. At leading order this dependence is reduced to only three parameters, two gauge couplings and the Higgs-field vacuum expectation value  $v$ . This three parameters can be determined by the three best-measured electroweak quantities: the electromagnetic coupling constant  $\alpha$ , measured in low-energy experiments, the Fermi

## Chapter 1. The Top Quark

---

constant  $G_F$ , determined from the  $\mu$  lifetime, and the mass of the Z-boson, measured in  $ee$  annihilation at LEP and SLC. By defining the electroweak mixing angle  $\theta_W$  through  $\sin^2 \theta_W \equiv 1 - m_W^2/m_Z^2$ , the  $W$  boson mass can be expressed as:

$$m_W^2 = \frac{\pi\alpha/\sqrt{2}G_F}{\sin^2 \theta_W (1 - \Delta r)}, \quad (1.14)$$

where  $\Delta r$  contains the one-loop corrections. Fig. 1.11 shows the top loop diagrams involved in  $\Delta r$ , whose contributions are:

$$(\Delta r)_{top} \approx -\frac{3G_F}{8\sqrt{2}\pi^2 \tan^2 \theta_W} m_t^2. \quad (1.15)$$

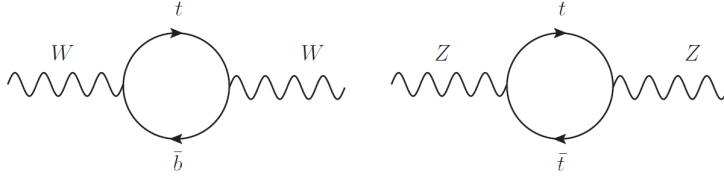


**Figure 1.11** – Virtual top quark loops contributing to the  $W$ - and  $Z$ -boson masses.

The top quark mass has been experimentally measured by the CDF and D0 collaborations with 0.5% accuracy. The measured top mass is [32]:

$$m_t = 173.2 \pm 0.6(stat) \pm 0.8(syst) \text{ GeV}. \quad (1.16)$$

Fig. 1.12 shows the most recent combination results of measurements from the Tevatron and LHC experiments [33].

The latest prediction from precision electroweak data yield is [34]:

$$m_t = 178.9_{-8.6}^{+11.7} \text{ GeV}. \quad (1.17)$$

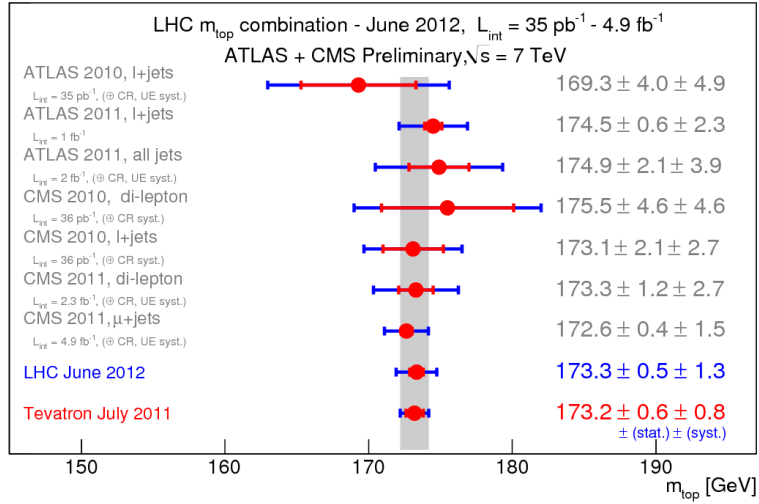


**Figure 1.12** – Overview of the  $m_t$  measurements from ATLAS and CMS, including the latest CDF and D0 combination.

The successful prediction of  $m_{t_{\text{top}}}$  without relying on its direct observation gives some confidence in the precision and predictive power of the radiative corrections in the SM. Therefore, the SM fit to the electroweak precision data including the direct measurements of  $m_{t_{\text{top}}}$  and  $M_W$  have been used to infer  $m_H$ .



---

---

## CHAPTER 2

---

### THE LHC AND THE ATLAS EXPERIMENT

#### 2.1 The Large Hadron Collider

The LHC [35] is currently the largest and highest-energy particle accelerator in the world. It's located at CERN, inside the 27 km long circular tunnel at a depth varying between 50 and 175 meters below the ground, which previously hosted the Large Electron Positron Collider (LEP). A schematic view of the facility is shown in Fig. 2.1

The LHC can provide both proton-proton ( $pp$ ) and heavy ion (HI) collisions. For  $pp$  collisions, the design luminosity is  $10^{34}\text{cm}^{-2}\text{s}^{-1}$  and the design center-of-mass energy for the collisions is 14 TeV. The LHC started its operations in 2008; during 2010 and 2011 runs, collisions at 7 TeV center-of-mass energy have been provided, in the 2012 the energy has been increased up to 8 TeV. The maximum instantaneous luminosity that has been reached in 2010 is slightly higher than  $2 \cdot 10^{32}\text{cm}^{-2}\text{s}^{-1}$ , while during 2011 run a peak of  $\approx 4 \cdot 10^{33}\text{cm}^{-2}\text{s}^{-1}$  has been achieved.

## Chapter 2. The LHC and the ATLAS experiment

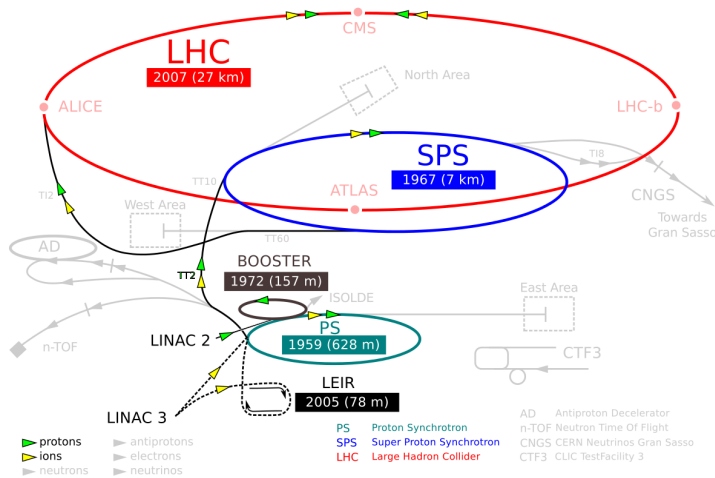


**Figure 2.1** – Schematic view of the CERN accelerator complex. Only the sections relevant for the LHC operations are highlighted with different colors.

HI collisions are designed with lead ions at an energy of 2.8 TeV per nucleon, reaching a design peak luminosity of  $10^{27} \text{cm}^{-2} \text{s}^{-1}$ . In 2010 HI collisions at 2.76 TeV per nucleon took place, reaching a peak instantaneous luminosity of  $30 \cdot 10^{24} \text{cm}^{-2} \text{s}^{-1}$ .

The LHC collider contains 1232 dipole magnets, which provide a magnetic dipole field of 8.33 T and keep particles in their orbits, and 392 quadrupole magnets for focusing the beams. The operating temperature of the magnets is 1.9 K, cooled by super-fluid helium. The proton beam is separated into bunches and each bunch contains  $\approx 10^{11}$  protons. Bunches have a spacing of 25 ns which corresponds to a collision frequency of 40 MHz. There are 2808 bunches per beam at the designed luminosity.

Before entering the LHC main ring, protons are accelerated up to 450 GeV by several pre-accelerators, which form the injector chain. Protons are created by an ion source which injects them into a radio-frequency (RF) cavity which accelerates them to 750 keV. After this, they are injected into the Linear Accelerator (LINAC) which brings their energy to 50 MeV. Next,

protons are transmitted to the Proton Synchrotron Booster (Booster) which increases the energy up to 1.4 GeV and sends them to the Proton Synchrotron (PS). Protons leave the PS with 25 GeV energy and enter the Super Proton Synchrotron (SPS) where their energy reaches 450 GeV. Afterwards, beams are directed to the LHC tunnel, where two separate proton beams circulating in opposite directions accelerate particles to the maximum value.

Four big experiments have been built around the collision points: ATLAS [36], CMS [37], LHCb [38] and ALICE [39]. ATLAS and CMS are general purpose experiments, designed to study high transverse momentum events for the search of the Higgs boson and other phenomena beyond the Standard Model (BSM). LHCb is designed especially to study b-physics, and ALICE for heavy ion collisions (HI), to study the formation of the so-called quark-gluon plasma.

Colliding particles are grouped together into a number of bunches, each containing  $\approx 10^{11}$  protons. The design number of bunches is 2808, so that interactions happen every 25 ns. During the commissioning phase, the number of colliding bunches has been progressively increased to reach the design value. At the end of 2010 the maximum number of colliding bunches has been 348, while 1092 has been then reached in June 2011.

The LHC started its operations on September 10th 2008, with the first beams circulating into the rings, in both directions, without collisions. After a commissioning phase, the first collisions were expected few days later. Unfortunately, on September 19th a major accident happened, due to a defective electrical connection between two magnets and 53 magnets were damaged. This caused a long stop of the machine, to do all the necessary reparations, to check the electrical connections and to improve the safety systems. During the Autumn 2009, after more than one year, the operations started again,

## Chapter 2. The LHC and the ATLAS experiment

---

with the first collisions at a center-of-mass energy of 900 GeV recorded by the four experiments on 23 November 2009.

After the 900 GeV collisions data taking, the center-of-mass energy was further increased to 2.36 TeV, beating the Tevatron's previous record of 0.98 TeV per beam and giving collisions at the highest energy ever reached before. After some months, on 30 March 2010, the first collisions at 7 TeV were registered, starting a new running period that went on until the beginning of November, when the LHC provided the first heavy ion collisions. After the lead ions collisions period and a technical stop during the winter,  $pp$  collisions have started again on 13 March 2011. At the end of the 2010  $pp$  running period, ATLAS accumulated an integrated luminosity of  $45 \text{ pb}^{-1}$  out of the total  $48.9 \text{ pb}^{-1}$  delivered by the LHC Fig. 2.2. Data taking then re-started

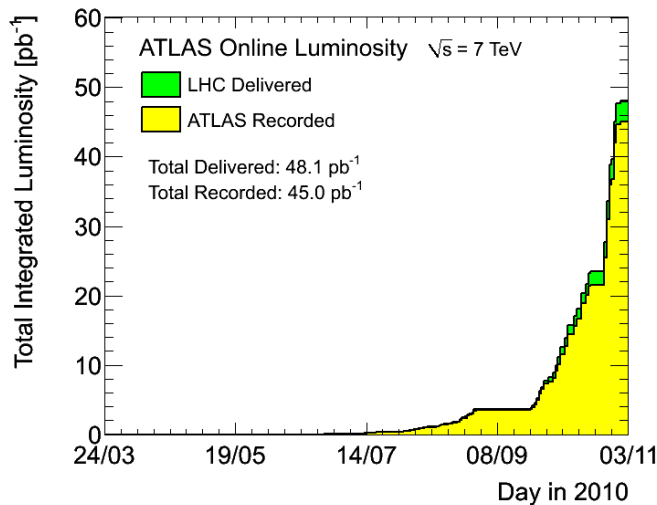


**Figure 2.2** – Online plot of the cumulative luminosity versus day delivered to (green), and recorded by ATLAS (yellow) during stable beams and for  $pp$  collisions at 7 TeV center-of-mass energy. The delivered luminosity accounts for the luminosity delivered from the start of stable beams until the LHC requests ATLAS to turn the sensitive detector off to allow a beam dump or beam studies.

in March 2011 until November 2011 accumulating  $5 \text{ fb}^{-1}$  of data (Fig. 2.3,

when another HI collisions period started to end the 2011 LHC run. In the

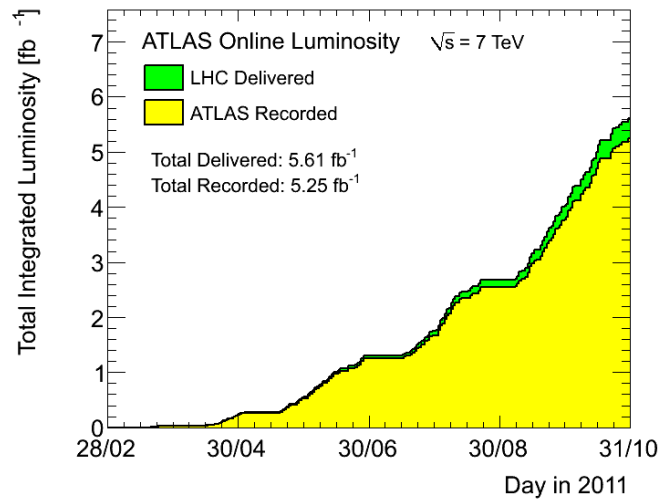


**Figure 2.3** – Cumulative luminosity versus day delivered to (green), and recorded by ATLAS (yellow) during stable beams and for pp collisions at 7 TeV center-of-mass energy in 2011.

2012 the center of mass energy was raised to 8 TeV. The current delivered luminosity for this run is shown in Fig. 2.4

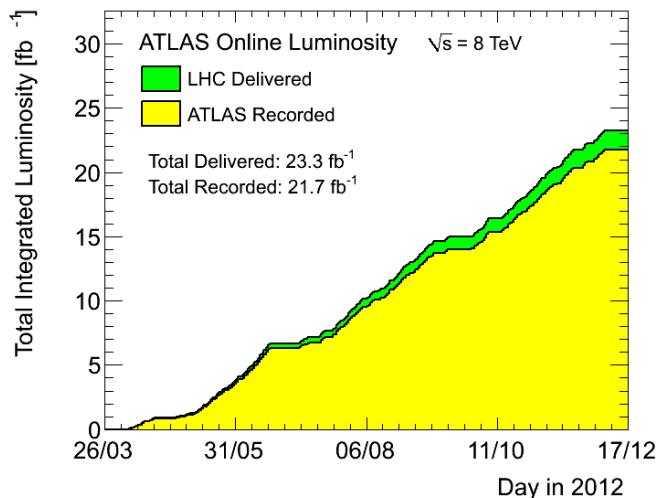


**Figure 2.4** – Cumulative luminosity versus day delivered to (green), and recorded by ATLAS (yellow) during stable beams and for pp collisions at 7 TeV center-of-mass energy in 2012 (snapshot taken on the 22th of october).

## 2.2 The ATLAS detector

The ATLAS (A Toroidal LHC ApparatuS) detector [36, 40, 41] is a multi-purpose particle detector 25 m high, 44 m long and weighting 7000 tons. A schematic overview of the apparatus is shown in Fig. 2.5. It is built around one of the interaction points of the LHC (Point 1) and composed of three main sub-detectors: the inner detector (ID), the calorimeter and the muon spectrometer (MS). The detector is divided into a barrel part and the two endcaps. The barrel is constructed from cylindrical layers around the beam axis while endcaps are perpendicular to the beam axis.

The barrel and two endcaps cover almost the full solid angle around the interaction point, which is defined as the origin of the coordinate system. The beam direction defines the  $z$ -axis and the  $x - y$  plane is transverse to the beam direction. The positive  $x$ -axis is defined as pointing from the interaction point to the center of the LHC ring and the positive  $y$ -axis is

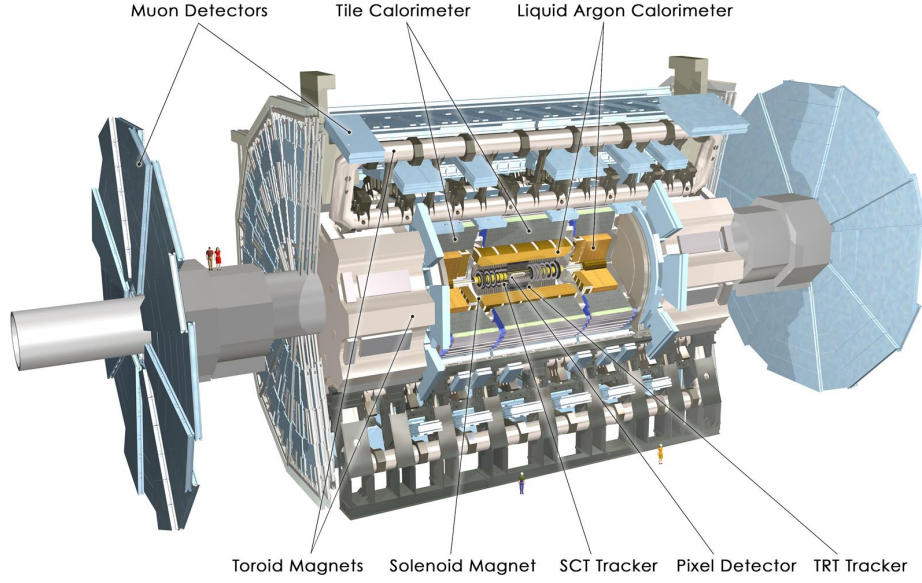


**Figure 2.5** – Sliced view of the ATLAS detector, with the indications of the main sub-systems.

defined as pointing upwards. The azimuthal angle  $\phi$  is measured around the beam axis, and the polar angle  $\theta$  is the angle from the beam axis. The *pseudorapidity* is defined as

$$\eta = -\ln \tan \theta/2 \quad (2.1)$$

and the rapidity as

$$y = \frac{E + p_z}{2(E - p_z)}. \quad (2.2)$$

The pseudorapidity tends to the rapidity in the limit of a mass-less particle. The distance between physics objects is usually defined in the  $\eta - \phi$  space as

$$\Delta R = \sqrt{(\Delta\eta)^2 + (\Delta\phi)^2} \quad (2.3)$$

### 2.2.1 The magnet system

The momentum of a charged particle is determined by measuring the curvature of its trajectory through the detector. To achieve this, all tracking devices need to be placed in a magnetic field to bend the particles' trajectories. The ATLAS detector contains a solenoid magnet to provide a magnetic field for the inner detector and barrel and endcap toroidal systems of eight magnet coils to induce the magnetic field inside the muon system. Both magnet systems consist of superconducting magnets, operating at a temperature of about 4.5 K.

#### The solenoid

The solenoid magnet covers the space between  $1.22 \text{ m} < r < 1.32 \text{ m}$  of the detector geometry, in between the inner detector and the calorimeter system. The main design constraint is therefore that the material budget of the magnet is reduced as much as possible to reduce energy losses of particles traversing it before reaching the calorimeters. Alongside the  $z$ -axis the solenoid covers a distance of 5.8 m. To further reduce the passive detector material the magnet is assembled inside the same vacuum vessel of the calorimeter. A magnetic field of 2 T is produced in the central region of the inner detector.

#### The toroid

Three independent air-core toroid systems (Fig. 2.6), each consisting of eight coils, are used in the barrel region ( $4.7 \text{ m} < r < 10.1 \text{ m}$ , length of 25.3 m) and endcap regions ( $0.8 \text{ m} < r < 5.4 \text{ m}$ , length of 5 m) on each side. The endcap toroids are rotated by  $22.5^\circ$  to ensure optimal bending power in the transition region. The magnetic field provided in the central part is 3.9 T

and grows to 4.1 T in the forward region. While each of the eight coils in the barrel is housed inside its own cryostat, the full endcap toroid system shares one cryostat on each side.

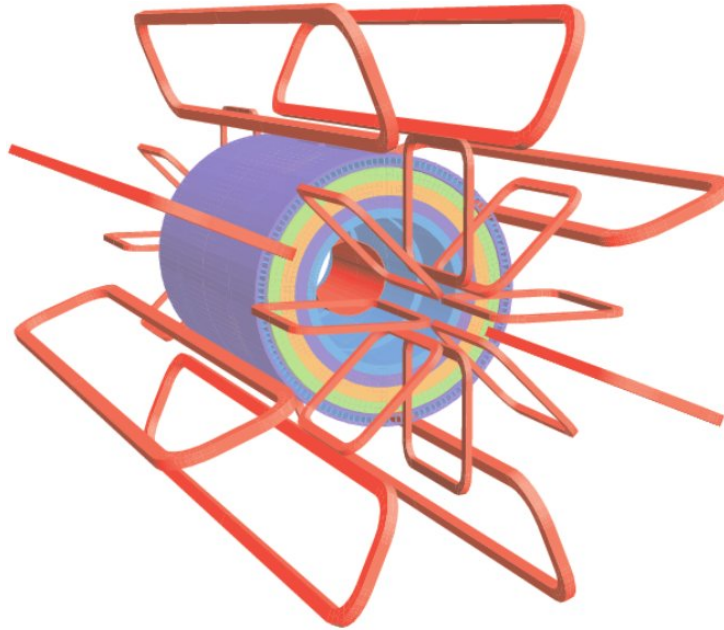


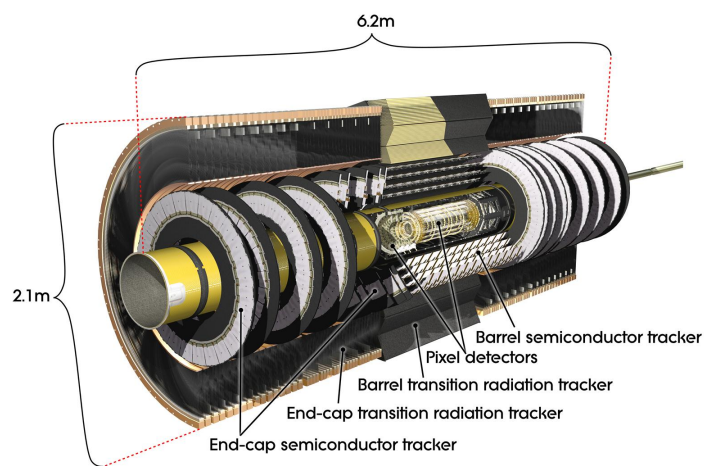
**Figure 2.6** – The ATLAS toroid magnetic system layout.

### 2.2.2 The Inner Detector

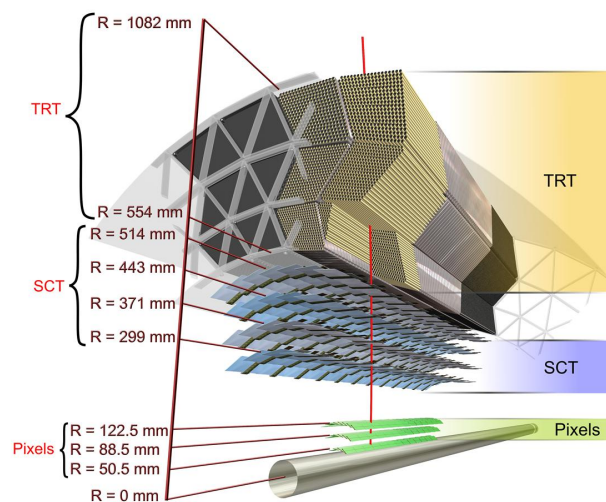
The Inner Detector (ID) is the innermost system of the ATLAS detector. Its schematic view is shown in Fig. 2.7.

It is composed of three sub-detectors: two silicon detectors, the Pixel Detector and the SemiConductor Tracker (SCT), and the Transition Radiation Tracker (TRT). It is embedded in an axial magnetic field of 2 T and its overall dimensions are 2.1 m in diameter and 6.2 m in length.

The ID measures the tracks produced by the passage of charged particles. It can measure the charged particles position and, making use of the the curvature of the trajectory due to the magnetic field, also their  $p_T$  and charge.



(a)



(b)

**Figure 2.7** – Longitudinal ((a)) and transversal ((b)) schematic view of the ATLAS inner systems.

In addition, thanks to the high precision of the track reconstruction, the ID is able to measure the position of the primary vertex in a collision, and to identify secondary vertexes due to pile-up or in flight decays of unstable particles.

A detailed description of the sub-detectors is given in the following subsections and a summary of their main characteristics is reported in Tab. 2.1.

Subdetector	Radius [cm]	Element size	Spatial resolution [ $\mu\text{m}$ ]	Hits/track	Readout channel
Pixel	5 – 12	$50 \mu\text{m} \times 400 \mu\text{m}$	$10(R - \phi) \times 115(z)$	3	$80 \times 106$
SCT	30 – 52	$80 \mu\text{m}$	$17(R - \phi) \times 580(z)$	8	$6 \times 106$
TRT	56 – 107	4 mm	130	30	$3.5 \times 105$

**Table 2.1** – Summary of the main characteristics of the three ATLAS ID sub-detectors.

### The Pixel detector

The Pixel Detector is the system closest to the interaction point and it is built directly around the beryllium beam pipe in order to provide the best possible primary and secondary vertex resolution. It is composed of three cylindrical layers in the barrel region (with a radius of 50.5 mm, 88.5 mm and 122.5 mm respectively) and two end-caps, each consisting of three disks (located at 495 mm, 580 mm and 650 mm from the detector center).

The Pixel Detector provides three precision measurement points for tracks with pseudorapidity  $|\eta| < 2.5$  and it has a full  $\phi$  coverage. The detector structure is made of low-mass carbon fibers and integrates the cooling system, resulting in a total contribution to the radiation length ( $X_0$ ) crossed by the particles produced in the collisions of about 3% per layer. Moreover, all the detector components are designed to sustain a radiation dose of  $\approx 500$  kGy, which is the one expected to be absorbed during the detector life time.

## Chapter 2. The LHC and the ATLAS experiment

---

The basic elements of the Pixel Detector are the silicon sensor “modules”, identical for barrel and disks. The  $250\ \mu\text{m}$  thick modules are divided into  $50\ \mu\text{m}$  wide and  $400\ \mu\text{m}$  long pixels, with 47232 pixels on each of the 1744 modules. The total number of channels for the whole detector is  $\approx 80.4$  millions.

### The SemiConductor Tracker

The SCT has quite similar functionality to the pixel detector, but is much larger in surface area than the pixel detector, which allows to measure tracks over longer distance. It consists of four cylindrical barrel layers with radial range between 30 cm and 51 cm and two endcaps with nine discs on each side of the barrel with radial range between 28 cm and 56 cm. There are 4088 modules made of four silicon microstrip sensors glued back to back with 40 mrad stereo angle. The strip pitch is about  $80\ \mu\text{m}$  with an intrinsic resolution of  $17 \times 580\ \mu\text{m}$ .

### The Transition Radiation Tracker

The TRT is the outermost system of the ID and its sensitive volume covers radial distances from 563 mm to 1066 mm. The detector consists of 298304 proportional drift tubes (straws), 4 mm in diameter, with a read out of  $\approx 351000$  electronic channels. The straws in the barrel region are arranged in three cylindrical layers and 32  $\phi$ -sectors. The straws in the end-cap regions are radially oriented and arranged in 80 wheel-like modular structures.

The TRT straw layout is designed so that charged particles with transverse momentum  $p_T > 0.5\ \text{GeV}$  and with pseudorapidity  $|\eta| < 2.0$  cross typically more than 30 straws. The TRT can also be used for particle identification. Its tubes are interleaved with layers of polypropylene fibers and foils: a

charged particle passing through the boundary region between materials with a different refraction index emits X-ray radiation. Since the photons created from transition radiation cause a considerably larger signal amplitude in the straws a distinction between the ionization from the initial charged particle and the transition radiation is possible. For this reason the straw read-out operates with two different thresholds to detect hits at the same time - a lower threshold to detect the charged particles from the main interaction and a higher threshold to detect the photons emitted due to transition radiation.

### **The cooling system**

For the Pixel Detector and the SCT, cooling is necessary to reduce the effect of the radiation damage on the silicon. Those two detectors share a cooling system, which uses  $C_3F_8$  fluid as a coolant. The target temperature for the silicon sensors after irradiation is  $0^\circ\text{C}$  for the Pixel Detector and  $-7^\circ\text{C}$  for the SCT. Because the TRT operates at room temperature, a set of insulators and heaters isolates the silicon detectors from the ATLAS environment.

### **2.2.3 The calorimeters**

The purpose of calorimeters is to measure the energy of charged and neutral particles with energy up to few TeV with high resolution and linearity. The calorimeter system consists of an electromagnetic (EM) calorimeter and hadronic calorimeters. Calorimeters cover the range of  $|\eta| < 4.9$  which is very important for the precise measurement of missing transverse energy. Fig. 2.8 shows an overview of the ATLAS calorimeters. Calorimeters must provide good containment for electromagnetic and hadronic showers, and must also limit punch-through into the muon system.

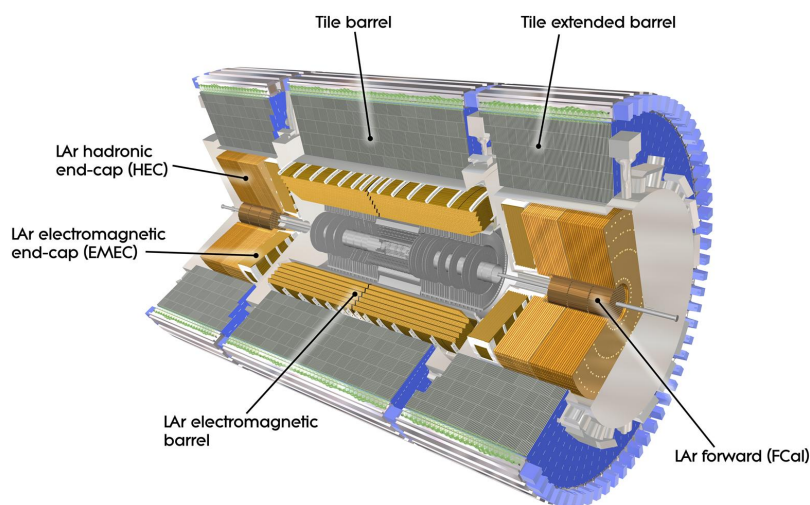


**Figure 2.8** – Schematic view of the ATLAS calorimeter system.

### The Electromagnetic Calorimeter

The EM calorimeter is a lead Liquid-Argon (LAr) detector. To ensure the maximum azimuthal coverage, the EM calorimeter was designed with an accordion geometry, as is a lead Liquid-Argon (LAr) detector. To ensure the maximum azimuthal coverage, the EM calorimeter was designed with an accordion geometry, as shown in Fig. 2.8: the readout electrodes and the lead absorbers are laid out radially and folded so that particles cannot cross the calorimeter without being detected. It is divided into one Barrel part ( $|\eta| < 1.475$ ) and two End-Caps ( $1.375 < |\eta| < 3.2$ ), each one with its own cryostat. The position of the central solenoid with respect to the EM calorimeter demands optimization of the material in order to achieve the desired calorimeter performance. As a consequence, the central solenoid and the LAr calorimeter share a unique vacuum vessel. The Barrel calorimeter consists of two identical half-barrels, separated by a small gap (4 mm) at  $z = 0$ . Each End-Cap is mechanically divided into two coaxial wheels: an

inner wheel covering the region  $1.375 < |\eta| < 2.5$ , and an outer wheel covering the region  $2.5 < |\eta| < 3.2$ .

Over the region devoted to precision physics ( $|\eta| < 2.5$ ), the EM calorimeter is segmented into three longitudinal parts: the strips, middle and back sections. While most of the electrons and photons energy is collected in the middle, the fine granularity of the strips is necessary to improve the  $\gamma - \pi^0$  discrimination and the back measures the tails of highly energetic electromagnetic showers, and helps to distinguish electromagnetic and hadronic deposits. For the End-Cap inner wheel, the calorimeter is segmented in two longitudinal sections and has a coarser lateral granularity than for the rest of the acceptance.

Since most of the central calorimetry sits behind the cryostat, the Solenoid and Inner Detector, EM showers begin to develop well before they are measured in the calorimeter. In order to take into account and correct for these losses, up to  $|\eta| = 1.8$  an additional presampler layer is mounted in front of the sampling portion of the calorimetry. The presampler is 11 mm (5 mm) thick in the Barrel (End-Cap) and includes fine segmentation in  $\eta$ . Differing from the rest of the calorimetry, the presampler has no absorber layer. It practically behaves almost like a single-layer LAr tracker.

The transition region between the Barrel and End-Cap EM calorimeters,  $1.37 < |\eta| < 1.52$ , is expected to have a poorer performance because of the higher amount of passive material in front; this region is often referred to as “crack region”. Electrons which are detected in that region are discarded for the purpose of this analysis.

### The Hadronic Calorimeter

The Hadronic Calorimeter is made with a variety of techniques depending on the region: Central, End-Cap and Forward.

In the central region there is the Tile Calorimeter (Tile), which is placed directly outside the EM calorimeter envelope. The Tile is a sampling calorimeter which uses steel as absorber and scintillating tiles as active material. It is divided into a Barrel ( $|\eta| < 1.0$ ) and two Extended Barrels ( $0.8 < |\eta| < 1.7$ ). Radially, the Tile calorimeter goes from an inner radius of 2.28 m to an outer radius of 4.25 m. It is longitudinally segmented in three layers of approximately 1.5, 4.1 and 1.8  $\lambda$  thickness for the Barrel and 1.5, 2.6, and 3.3  $\lambda$  for the Extended Barrel.

The Hadronic End-Cap Calorimeter (HEC) consists of two independent wheels for each end-cap, located directly behind the End-Cap EM calorimeter and sharing the same cryostats. It covers the region  $1.5 < |\eta| < 3.1$ , overlapping both with the Tiles and the Forward Calorimeter. The HEC uses the LAr technology. Each wheel is divided into two longitudinal segments, for a total of four layers per End-Cap. The wheels closest to the interaction point are built from 25 mm parallel Copper plates, while those further away use 50 mm Copper plates. The outer radius of the Copper plates is 2.03 m, while the inner radius is 0.475 m (except in the overlap region with the Forward Calorimeter where this radius becomes 0.372 m). The Copper plates are interleaved with 8.5 mm LAr gaps, providing the active medium for this sampling calorimeter.

### The Forward Calorimeters

The Forward Calorimeter (FCal) covers the  $3.1 < |\eta| < 4.9$  region and is another LAr based detector. Integrated into the End-Cap cryostats, it is

approximately  $10 \lambda$  thick, and consists of three 45 cm thick independent modules in each End-Cap: the absorber of the first module is Copper, which is optimized for electromagnetic measurements, while for the other two is Tungsten, which is used to measure predominantly the energy of hadronic interactions. Both materials have been chosen for their resistance to radiation. The region where the FCal is placed is very close to the beam pipe and the expected radiation dose is then very high. Therefore the electrode structure is different from the accordion geometry, consisting in a structure of concentric rods and tubes parallel to the beam axis. The LAr in the gap between the rod and the tube is the sensitive medium.

The performance of the calorimeter system is summarized in Tab. 2.2.

Detector component	Energy resolution ( $\sigma_E/E$ )	$\eta$ coverage
EM calorimeter	$10\% \times \sqrt{1 \text{ GeV}/E} \otimes 0.7\%$	$ \eta  < 3.2$ ( $< 2.5$ for the trigger)
Hadronic calorimetry		
Barrel and Endcap	$50\% \times \sqrt{1 \text{ GeV}/E} \otimes 3\%$	$ \eta  < 3.2$
Forward	$100\% \times \sqrt{1 \text{ GeV}/E} \otimes 3.1$	$3.1 <  \eta  < 4.9$

**Table 2.2** – Nominal detector performance specifics and coverage for the ATLAS calorimetric system.

### 2.2.4 The Muon Spectrometer

The MS is the largest and outermost subdetector of ATLAS and measures muon momenta within the  $|\eta| < 2.7$  region. The MS consists of two types of precision measurement chambers: Monitored Drift Tubes (MDT) and Cathode-Strip Chambers (CSC), and two types of trigger chambers: Resistive Plate Chambers (RPC) and Thin Gap Chambers (TGC). Fig. 2.9 shows a schematic view of the system.

The muon system has two different functions: it is needed for high precision tracking of muons and also for triggering on them. Muons frequently indicate

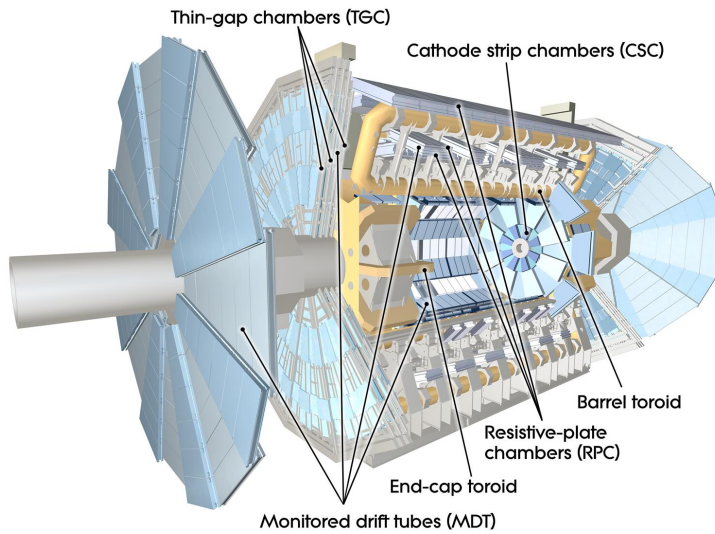


**Figure 2.9** – A sliced view of the ATLAS Muons Spectrometer.

an interesting event and, therefore, a muon-based trigger is useful for selecting some new physics signals. On the other hand, in order to precisely measure the decays of new particles, one needs to make accurate measurements of each muon's momentum.

The momentum measurement is based on the reconstruction of the muon's trajectories bent by a magnetic field. The large volume magnetic field is provided by the toroid magnetic system, as explained in Sect. 2.2.1. The momentum measurement is performed over most of the  $\eta$ -range by the Monitored Drift Tubes (MDT). At large  $\eta$  and close to the interaction point, Cathode Strip Chambers (CSC) with higher granularity are used: they have been designed to withstand the demanding rate and background conditions. The stringent requirements on the relative alignment of the muon chamber layers are obtained by the combination of precision mechanical-assembly techniques and optical alignment systems both within and between muon chambers.

The triggering function of the muon system covers the pseudorapidity range  $|\eta| < 2.4$ . Resistive Plate Chambers (RPC) are used in the barrel

and Thin Gap Chambers (TGC) in the end-cap regions. The trigger chambers for the MS fulfill a three-fold purpose: to provide bunch-crossing identification, to provide well-defined transverse momentum thresholds and to measure the muon coordinate in the direction orthogonal to that determined by the precision-tracking chambers.

The barrel chambers are positioned on three cylinders concentric with the beam axis, at radii of about 5, 7.5, and 10 m. They cover the pseudorapidity range  $|\eta| < 1$ . The end-cap chambers cover the range  $1 < |\eta| < 2.4$  and are arranged in four disks at distances of 7, 10, 14 and 21-23 m from the interaction point, concentric with the beam axis.

The MS reconstruction efficiency and resolution were measured using cosmic ray events in 2008 and 2009 [42]. The reconstruction efficiency, integrated over the detector acceptance, is  $\approx 94\%$ . At  $\eta = 0$  there is a gap in the detector for cable routing. If the region of the detector near this gap is excluded, the reconstruction efficiency is increased to 97%. The transverse momentum resolution determined from this data is:

$$\frac{\sigma_{p_T}}{p_T} = \frac{0.29 \text{ GeV}}{p_T} \otimes 0.043 \otimes \frac{p_T}{4.1 \text{ GeV}}$$

in the range  $5 \text{ GeV} < p_T < 400 \text{ GeV}$ .

### 2.2.5 The luminosity detectors

One measurement which is very important for almost every physics analysis is the luminosity measurement [43]. As it is a fundamental quantity, three different detectors help in its determination. At  $\pm 17$  m from the interaction region there is the LUCID (LUMinosity measurement using Cerenkov Integrating Detector). It detects inelastic  $pp$  scattering in the forward di-

rection and it is the main online relative-luminosity monitor for ATLAS. It is also used, before collisions are delivered by the LHC, to check the beam losses. For the beam monitoring, another detector has been inserted: the BCM (Beam condition Monitor). The other detector used for luminosity measurement is ALFA (Absolute Luminosity For ATLAS). It is located at  $\pm 240$  m from the interaction point. It consists of scintillating fiber trackers located inside Roman pots which are designed to approach as close as 1 mm from the beam. The last detector is ZDC (Zero-Degree Calorimeter). It is located at  $\pm 140$  m from the interaction point, just beyond the point where the common straight-section vacuum-pipe divides back into two independent beam-pipes. Neutral particles with  $|\eta| \geq 8.2$ , not being affected by the magnetic fields which bend the proton beams, are detected and measured by the ZDC modules.

### 2.2.6 Trigger and data acquisition

At the LHC design luminosity  $10^{34} \text{cm}^{-2} \text{s}^{-1}$  with 25 ns bunch spacing the crossing rate is 40 MHz. The data writing to storage however is limited to 200 Hz. This means that only 0.0005% of the total events can be saved. The trigger task of selecting and saving interesting physics processes for future offline analysis is then quite challenging.

The ATLAS trigger system [36] has three distinct levels: Level-1 (L1), Level-2 (L2), and the event filter level (EF). Each trigger level refines the decisions made at the previous level and, where necessary, applies additional selection criteria. The L2 and EF together form the High-Level Trigger (HLT). The L1 trigger is implemented using custom-made electronics, while the HLT is almost entirely based on commercially available computers and networking hardware. A block diagram of the trigger and data acquisition

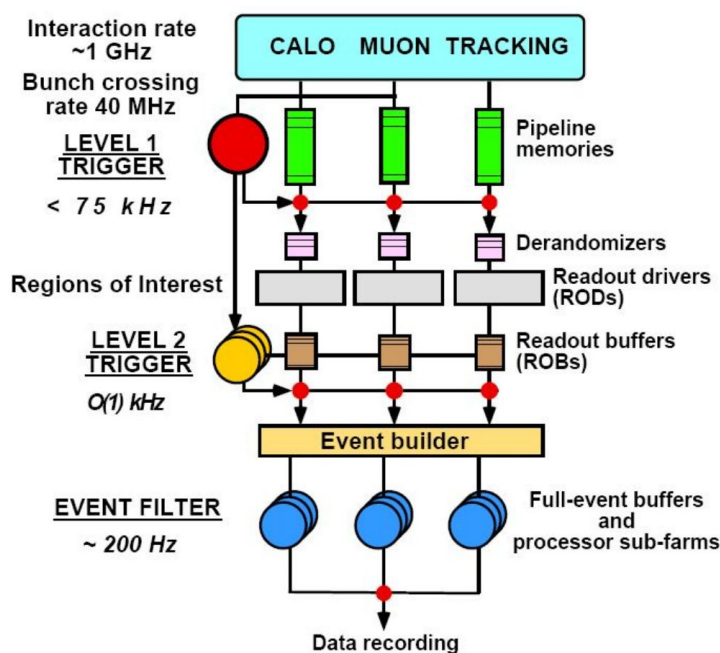


Figure 2.10 – ATLAS trigger and data acquisition system.

systems is shown in Fig. 2.10.

The L1 trigger searches for signatures from muons, electrons/photons, jets and  $\tau$ -leptons decaying into hadrons. It also selects events with large missing transverse energy and large total transverse energy. The L1 trigger uses reduced-granularity information from a subset of detectors: the RPC, TGC and calorimeter subsystems. It rejects the main part of low-energy events, reducing the rate to 75 kHz and makes a decision within  $2.5 \mu\text{s}$  after the bunch-crossing. Results from the L1 trigger are processed by the Central Trigger Processor (CTP), which implements a trigger “menu” made of trigger items corresponding to different thresholds and signatures. Events passing the L1 trigger selection are transferred to the next stages where all detector channels are read out to the Read Out Drivers (RODs) and then into Read Out Buffers (ROBs). The L1 trigger uses only the multiplicity of the triggered objects, the position information of the objects are not used. In each event,

## Chapter 2. The LHC and the ATLAS experiment

---

the L1 trigger also defines one or more Regions-of-Interest (RoI's), i.e. the spatial coordinates in  $\eta$  and  $\phi$ , of those regions where its selection process has identified interesting features. This information is subsequently used by the HLT.

The L2 trigger uses RoI information on coordinates, energy, and type of signatures to limit the amount of data which must be transferred from the detector readout. The L2 trigger reduces the event rate to below 3.5 kHz, with an average event processing time of approximately 40 ms. The information is stored in the ROBs until the L2 processing finishes. If the event is not rejected by the L2 trigger the events goes to the next trigger level, the EF, where the event building process starts.

The EF uses offline analysis procedures and completes the event building procedure. It reduces the event rate to approximately 200 Hz, with an average event processing time of order four seconds. The HLT algorithms use the full granularity and precision of calorimeter and muon chamber data, as well as the data from the inner detector, to refine the trigger selections. The EF, in addition to the selection, classifies the selected events according to the ATLAS physics streams. The same event can be stored in more than one streams, if several stream requirements are satisfied. The physics data streams are classified as electrons, muons, jets, photons, missing transverse energy,  $\tau$ -leptons and  $b$ -physics. In particular, for the purpose of analysis presented in this thesis, data from the electron and muon trigger streams are used.

---

---

## CHAPTER 3

---

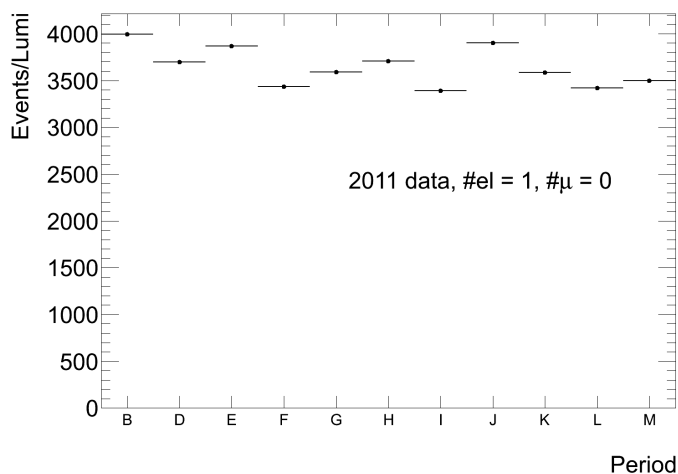
### DATA AND MONTE CARLO SAMPLES

#### 3.1 Data samples

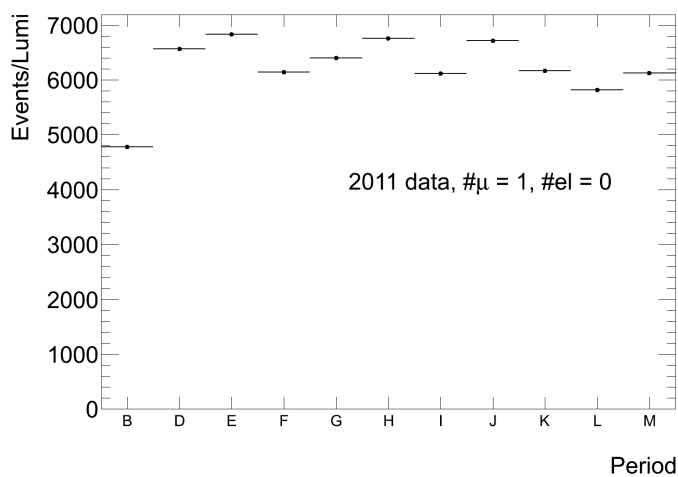
Only data for which all the subsystems described in Sect. 2.2 are fully operational are used in the analysis. Applying these requirements to the  $\sqrt{s} = 7 \text{ TeV}$   $pp$  collision data taken in stable beam conditions during the 2011 LHC run, results in a data sample of  $4.7 \text{ fb}^{-1}$ .

The luminosity is determined from proton scattering measurements and Van der Meer scans, with a relative uncertainty of 3.4% for 2011 data [44].

Data samples are divided in several data-taking periods, characterized by different beam and detector conditions. Fig. 3.1 shows the number of selected events in 2011 data, applying only the “lepton veto” described in Chapter 5 as a function of the data-taking periods considered for the analysis, divided by the integrated luminosity shown in Tab. 3.1. These plots are useful to check the stability of the event selection efficiency and its dependence on the different beam and detector conditions.



(a)



(b)

**Figure 3.1** – Number of events per period divided by the luminosity of the period requiring exactly one good electron and no muons (a) and requiring exactly one good muon and no electrons (b). The definitions of “good” electrons and muons are presented in Chapter 4.

Period	Integrated Luminosity ( $\text{pb}^{-1}$ )
B	17
D	179
E	50
F	152
G	560
H	278
I	399
J	233
K	660
L	1568
M	1121
Total	5217

**Table 3.1** – The luminosity delivered by LHC divided per data period for the 2011 data taking.

## 3.2 Monte Carlo simulations

The purpose of Monte-Carlo (MC) generators is the simulation of processes resulting from hard interactions due to inelastic scattering processes, which are called “events”. Events in MC are generated according to the theoretical predicted cross sections. Simulated MC samples serve a broad range of purposes: they can be used to test theoretical models against the detector response, develop analysis strategy, estimate efficiencies, resolutions of the reconstructed objects, validate reconstruction algorithms, evaluate statistical and systematic uncertainties and so on.

The event simulation process is usually divided into two steps:

- Generation of the event by calculating the production process originating from an inelastic  $pp$  scattering and immediate decays into a final state of stable particles.
- Simulation of the detector geometry and digitization of the energy de-

posited in the sensitive regions of the detector in order to reproduce the real detector response.

### 3.2.1 Generation

The generation of the events consists in the production of a series of particles through a simulation process. Every event generator produces a set of stable particles (like electrons, muons, pions and photons) and many unstable particles (like quarks and gluons).

The major part of the generators are designed for LO calculations. Among these are the AcerMC [45] and Alpgen [46]. There are matrix element generators designed for next-to-leading order (NLO) calculations such as MC@NLO [47, 48] and Powheg [49]. For parton showering and hadronization Pythia [50] and Herwig [51] and for multiple interactions Herwig by the interface to Jimmy [52] can be used. There are many other generators available, but only those which are used for this analysis have been included in this discussion.

Usually the generation of simulated physical events is done in several steps:

- hard process;
- parton shower;
- hadronization;
- decay;
- multiple interaction and beam remnants (also known as minimum bias collisions).

Fig. 3.2 show the schematic workflow of a typical Monte Carlo event generation.

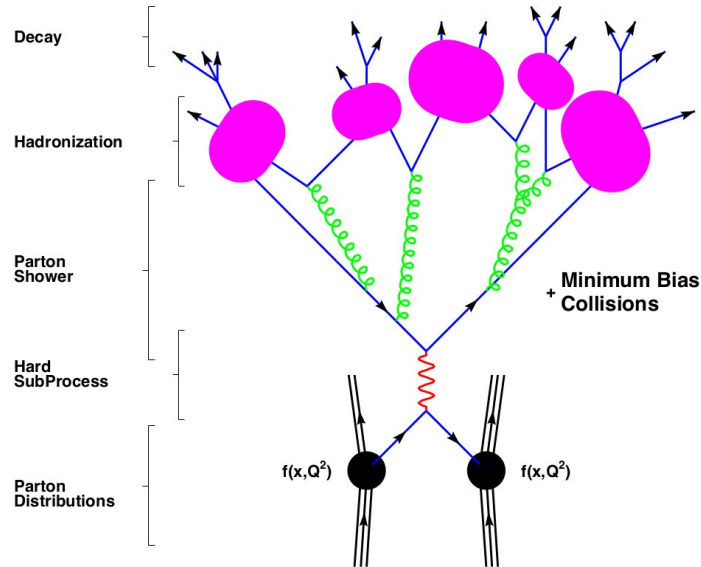


**Figure 3.2** – Schematic workflow of a typical Monte Carlo event generation.

### Hard process

The Hard Process is the most theoretically understood part of the interaction. The simulation of this part is usually done with fixed-order perturbative matrix elements, which describe the transitions between the initial and final state in Feynman diagrams. At the LO, the squared matrix elements are positive definite, so all complications involving the regularization of matrix elements are avoided, and the codes are based either on the direct computation of the relevant Feynman diagrams or on the solutions of the underlying classical field theory [53]. Tree-level matrix element generators can be automated and used for generation of arbitrary or specific processes. On the contrary, Next-to-Leading-Order calculations are more difficult to automate, because the real and virtual contributions which are considered have equal and opposite divergences, and so generators need to know ahead the way to carry on the hadronization level.

### Parton shower

Once the hard scattering partons are produced they will irradiate energetic gluons, just like accelerated electrical charges irradiate photons (Fig. 3.3). This process links the highly virtual state from the hard scattering to the initial (space-like emission) and final (time-like emission) observable state, and goes on until the virtuality of the generated shower becomes too small to be treated by the perturbative QCD (pQCD) [54].

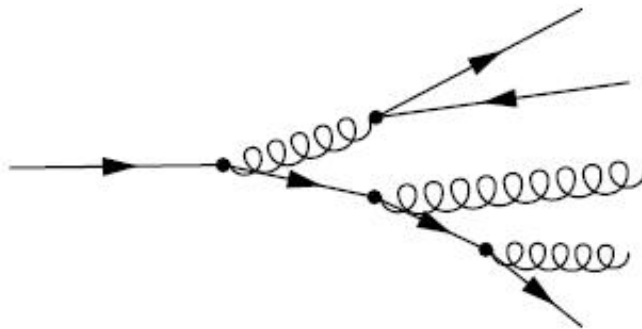


**Figure 3.3** – Example of parton shower.

### Hadronization

This step is typically non-perturbative and therefore is described only by phenomenological models. In Pythia [50], for example, it's implemented the model called “Lund Model” [55] (other models exist, like the “Cluster Model” implemented in Herwig [51]). This model is based on the approximation in which, at large distances, the field lines between the two partons tend to get “packed” in “strings”, resulting in an effective potential that is linear at a first approximation:

$$V(R) = V_0 + \kappa R - \frac{e}{R} + \frac{f}{R^2}, \quad (3.1)$$

where  $\kappa \approx 1 \text{ GeV/fm}$ . Therefore, quark-antiquark pairs can be produced by tunnel-effect with a probability  $\approx \exp[-b(m_q^2 + p_T^2)]$ .

### Multiple interactions and additional processes

The underlying structure of the event, beam remnants, multi-parton interactions, initial and final state radiations (ISR/FSR), and pile-up, are superimposed to the hard scattering process. Beam remnants are the parts of hadrons which did not participate in the hard scattering process. Multi-parton interactions happen when, beside the two partons involved in the hard scattering, other partons from the colliding protons interact producing additional activity. ISR/FSR are the emissions associated with incoming and outgoing particles, respectively. Lastly, due to the large number of particles per bunch, more than one collision can occur simultaneously. The presence of more than one interaction in the same bunch crossing is called pile-up. Pile-up includes also such effects as beam halo, beam gas, cavern background events detector responses to long-lived particles, as well as overlapping detector responses from interactions of neighboring bunch crossings, called out-of-time pile-up.

### The challenge of the *matching*

The simulations produced with the Monte Carlo generator at the Matrix Element level, need to be interfaced with a parton shower MC to describe the soft QCD emission (collinear region). In Tab. 3.2 are shown the main features of these two types of approach for the multi-parton final states generation.

Since these two approaches describe different regions of the parameter space, it can happen that the same configuration could be described both at ME level ( $n + 1$  partons) and PS ( $n$  partons + one soft emission). It's therefore necessary to correctly handle overlaps in order to avoid double

<b>Matrix Element</b>	<b>Parton shower</b>
Correct description far from the collinear region	Correct description in the soft/collinear approximations
Fixed final state multiplicity	No limits to the multiplicities
Can simulate hard jet emission	Can't simulate hard jet emission
Heavily CPU-demanding	Lightweight and fast to run

**Table 3.2** – Features and differences between the ME and PS generators.

countings. The procedures that allow this kind of checks are called “matching algorithms”. For the samples used in this analysis, the “MLM” approach has been adopted [56].

### 3.2.2 Simulation

The detector response is simulated by transporting generated events through the detector using the simulation toolkit `GEANT4` [57]. It provides models for physics and infrastructure for particle propagation through a detector geometry. The energies deposited in the sensitive portions of the detector are recorded as “hits” containing the energy deposition, position, and time.

The digitization takes the hit output from simulated events; hard scattering signal, underlying event, pile-up, and converts it into detector responses. The information of each subdetector can be presented in either an object-based format or in a format identical to the output of the ATLAS data acquisition system, i.e. similar to the real detector output (raw data). This allows to process both simulated and “real” data using the same ATLAS trigger and reconstruction packages [58].

### 3.2.3 Monte-Carlo samples

The generation of  $t\bar{t}$  signal and single top events uses the MC@NLO software with the CTEQ6.6 PDF set [23], with the top mass set to 172.5 GeV. The  $t\bar{t}$  production cross section is normalized to 164.57 pb using the approximate Next-to-Next Leading Order QCD (aNNLO QCD) calculation provided by HATHOR [59]. On the truth level the sample is filtered for single-lepton and dilepton decay final states, which means at least one of the  $W$ -bosons from top quark should decay to a neutrino and an electron, a muon or a tau. Single top quark production includes the  $t$ ,  $Wt$  and  $s$  channels and the cross section is normalized to the MC@NLO predicted cross section using the “diagram removal scheme” final state [26].

The generation of  $Z$ +jets events uses the Alpgen MC generator, using the MLM matching scheme and PDF set CTEQ6L1 in a phase space restricted to  $10 < m_{ll} < 40$  GeV and  $40 < m_{ll} < 2000$  GeV regions. These samples are normalized with an NLO/LO  $k$ -factor of 1.25. These  $k$ -factors are used to scale the cross section from LO simulations to higher order.  $Z$ +jets samples used for the analysis include also the full Drell-Yan contribution from the  $\gamma^* \rightarrow ll$  process and take the  $Z/\gamma^*$  interference into account.

The relative small background due to diboson  $WW/WZ/ZZ$  events is modeled using the Alpgen generator (using Herwig for the hadronization and Jimmy for the underlying event model), normalized with appropriate  $k$ -factors of 1.26 ( $WW$ ), 1.28 ( $WZ$ ) and 1.30 ( $ZZ$ ).

Details on the MC samples used are shown in Tabs. 3.3-3.8. A complete description of the MC samples used for signal and background is given in [60].

### Chapter 3. Data and Monte Carlo samples

---

ID	Description	ME + PS	$\sigma$ [pb]	$k$ -factor
105200	No full-had	MC@NLO+Herwig/Jimmy	80.11	1.12
105860	No full-had	Powheg+Herwig	79.12	1.13
105861	No full-had	Powheg+Pythia	79.12	1.13
117862	No full-had, I/FSR max	AcerMC+Pythia	41.01	2.208
117863	No full-had, I/FSR min	AcerMC+Pythia	58.23	2.209

**Table 3.3** –  $t\bar{t}$  samples which do not include all hadronic decays (No full-had). The 105200 sample is used for the nominal analysis, the others are used for systematic evaluation.

ID	Description	ME + PS	$\sigma$ [pb]	$k$ -factor
117360	Single top ( $t$ -chan) $\rightarrow e\nu$	AcerMC+Pythia	8.06	0.865
117361	Single top ( $t$ -chan) $\rightarrow \mu\nu$	AcerMC+Pythia	8.06	0.865
117362	Single top ( $t$ -chan) $\rightarrow \tau\nu$	AcerMC+Pythia	8.05	0.866
108343	Single top ( $s$ -chan) $\rightarrow e\nu$	MC@NLO+Herwig/Jimmy	0.47	1.064
108344	Single top ( $s$ -chan) $\rightarrow \mu\nu$	MC@NLO+Herwig/Jimmy	0.47	1.064
108345	Single top ( $s$ -chan) $\rightarrow \tau\nu$	MC@NLO+Herwig/Jimmy	0.47	1.064
108346	Single top ( $Wt$ -chan) inclusive	MC@NLO+Herwig/Jimmy	14.59	1.079

**Table 3.4** – Single top samples.

ID	Description	ME + PS	$\sigma$ [pb]	$k$ -factor
116250/107650	$Z(\rightarrow ee) + 0p$	Alpgen+Herwig	3055.2 / 668.3	1.25
116251/107651	$Z(\rightarrow ee) + 1p$	Alpgen+Herwig	84.9 / 134.4	1.25
116252/107652	$Z(\rightarrow ee) + 2p$	Alpgen+Herwig	41.4 / 40.5	1.25
116253/107653	$Z(\rightarrow ee) + 3p$	Alpgen+Herwig	8.4 / 11.2	1.25
116254/107654	$Z(\rightarrow ee) + 4p$	Alpgen+Herwig	1.9 / 2.9	1.25
116255/107655	$Z(\rightarrow ee) + 5p$	Alpgen+Herwig	0.5/0.8	1.25
116260/107660	$Z(\rightarrow \mu\mu) + 0p$	Alpgen+Herwig	3054.9 / 668.7	1.25
116261/107661	$Z(\rightarrow \mu\mu) + 1p$	Alpgen+Herwig	84.9 / 134.1	1.25
116262/107662	$Z(\rightarrow \mu\mu) + 2p$	Alpgen+Herwig	41.5 / 40.3	1.25
116263/107663	$Z(\rightarrow \mu\mu) + 3p$	Alpgen+Herwig	8.4 / 11.2	1.25
116264/107664	$Z(\rightarrow \mu\mu) + 4p$	Alpgen+Herwig	1.9 / 2.8	1.25
116265/107665	$Z(\rightarrow \mu\mu) + 5p$	Alpgen+Herwig	0.5 / 0.8	1.25
116270/107670	$Z(\rightarrow \tau\tau) + 0p$	Alpgen+Herwig	3055.1 / 668.4	1.25
116271/107671	$Z(\rightarrow \tau\tau) + 1p$	Alpgen+Herwig	84.9 / 134.8	1.25
116272/107672	$Z(\rightarrow \tau\tau) + 2p$	Alpgen+Herwig	41.4 / 40.4	1.25
116273/107673	$Z(\rightarrow \tau\tau) + 3p$	Alpgen+Herwig	8.4 / 11.3	1.25
116274/107674	$Z(\rightarrow \tau\tau) + 4p$	Alpgen+Herwig	1.9 / 2.8	1.25
116270/107670	$Z(\rightarrow \tau\tau) + 5p$	Alpgen+Herwig	0.5 / 0.8	1.25

**Table 3.5** –  $Z/\gamma^*$ +jets samples with phase space cuts  $10 \text{ GeV} < m_{ll} < 40 \text{ GeV}$  (left) and  $m_{ll} > 40 \text{ GeV}$ (right).

### Chapter 3. Data and Monte Carlo samples

ID	Description	ME + PS	$\sigma$ [pb]	$k$ -factor
107860	$W \rightarrow e\nu + 0p$	Alpgen+Herwig/Jimmy	6930.50	1.196
107861	$W \rightarrow e\nu + 1p$	Alpgen+Herwig/Jimmy	1305.30	1.196
107862	$W \rightarrow e\nu + 2p$	Alpgen+Herwig/Jimmy	378.13	1.196
107863	$W \rightarrow e\nu + 3p$	Alpgen+Herwig/Jimmy	101.86	1.196
107864	$W \rightarrow e\nu + 4p$	Alpgen+Herwig/Jimmy	25.68	1.196
107865	$W \rightarrow e\nu + 5p$	Alpgen+Herwig/Jimmy	6.99	1.196
107690	$W \rightarrow \mu\nu + 0p$	Alpgen+Herwig/Jimmy	6932.40	1.195
107691	$W \rightarrow \mu\nu + 1p$	Alpgen+Herwig/Jimmy	1305.90	1.195
107692	$W \rightarrow \mu\nu + 2p$	Alpgen+Herwig/Jimmy	378.07	1.195
107693	$W \rightarrow \mu\nu + 3p$	Alpgen+Herwig/Jimmy	101.85	1.195
107694	$W \rightarrow \mu\nu + 4p$	Alpgen+Herwig/Jimmy	25.72	1.195
107695	$W \rightarrow \mu\nu + 5p$	Alpgen+Herwig/Jimmy	7.00	1.195
107700	$W \rightarrow \tau\nu + 0p$	Alpgen+Herwig/Jimmy	6931.80	1.195
107701	$W \rightarrow \tau\nu + 1p$	Alpgen+Herwig/Jimmy	1304.90	1.195
107702	$W \rightarrow \tau\nu + 2p$	Alpgen+Herwig/Jimmy	377.93	1.195
107703	$W \rightarrow \tau\nu + 3p$	Alpgen+Herwig/Jimmy	101.96	1.195
107704	$W \rightarrow \tau\nu + 4p$	Alpgen+Herwig/Jimmy	25.71	1.195
107705	$W \rightarrow \tau\nu + 5p$	Alpgen+Herwig/Jimmy	7.00	1.195

**Table 3.6** – Samples including  $W$  + light jets,  $W$  + charm (mass-less charm) and  $W$  +  $bb$  (where the  $bb$  pair is produced in the parton shower).

ID	Description	ME + PS	$\sigma$ [pb]	$k$ -factor
117293	$W \rightarrow c + 0p$ inclusive	Alpgen+Herwig/Jimmy	644.4	1.20
117294	$W \rightarrow c + 1p$ inclusive	Alpgen+Herwig/Jimmy	205.0	1.20
117295	$W \rightarrow c + 2p$ inclusive	Alpgen+Herwig/Jimmy	50.8	1.20
117296	$W \rightarrow c + 3p$ inclusive	Alpgen+Herwig/Jimmy	11.4	1.20
117297	$W \rightarrow c + 5p$ inclusive	Alpgen+Herwig/Jimmy	2.8	1.20
117284	$W \rightarrow cc + 0p$ inclusive	Alpgen+Herwig/Jimmy	127.53	1.20
117285	$W \rightarrow cc + 1p$ inclusive	Alpgen+Herwig/Jimmy	104.68	1.20
117286	$W \rightarrow cc + 2p$ inclusive	Alpgen+Herwig/Jimmy	52.08	1.20
117287	$W \rightarrow cc + 3p$ inclusive	Alpgen+Herwig/Jimmy	16.96	1.20
107280	$W \rightarrow bb + 0p$ inclusive	Alpgen+Herwig/Jimmy	47.35	1.200
107281	$W \rightarrow bb + 1p$ inclusive	Alpgen+Herwig/Jimmy	35.76	1.200
107282	$W \rightarrow bb + 2p$ inclusive	Alpgen+Herwig/Jimmy	17.33	1.200
107283	$W \rightarrow bb + 3p$ inclusive	Alpgen+Herwig/Jimmy	7.61	1.200

**Table 3.7** – Samples including  $W$  + heavy quarks ( $c$  and  $b$ ). “Inclusive” means that the  $W$  can decay in either an electron, muon or tauon and a neutrino

ID	Description	ME + PS	$\sigma$ [pb]	$k$ -factor
105985	$WW$	Herwig	11.5003	1.48
105986	$ZZ$	Herwig	0.9722	1.30
105987	$WZ$	Herwig	3.4641	1.60

**Table 3.8** – Samples including  $WW/WZ/ZZ$ , filtered requiring one lepton with  $p_T > 10$  GeV and  $|\eta| < 2.8$ .

### 3.3 $t\bar{t}$ signal estimation

As shown in Sect. 3.2.3, top quark pair production is simulated using the MC@NLO event generator interfaced with HERWIG and JIMMY to model the parton showering and the underlying event.

The assumed central value for the top quark mass is  $m_t = 172.5$  GeV. The sample is split into a subsample including only the all-hadronic decay channel, not used in the analysis<sup>1</sup>, and another sample containing the dileptonic and the lepton+jets channels.

While MC@NLO predicts an inclusive top quark pair production cross section at NLO plus parton shower, more precise predictions for the total rate of top quark pair production are available at approximate NNLO, so the simulated  $t\bar{t}$  sample is rescaled via a  $k$ -factor to the prediction from the aNNLO QCD calculations evaluated with the Hathor framework [59],  $\sigma_{t\bar{t}} = 164.6 \pm 9.3(\text{scale}) \pm 6.5(\text{PDF})$  pb.

Beside the NLO prediction, the nominal sample of top pair events was generated also using the ALPGEN generator and CTEQ6L1 PDF set. The sample was generated for  $t\bar{t}$  with zero to four exclusive and five inclusive additional light partons. Parton showering and fragmentation was performed by HERWIG. The MLM parton-jet matching scheme was applied (ETCLUS 20 GeV, RCLUS 0.7, ETACCLUS 6.0) to avoid double counting of configurations generated by both the parton shower and the matrix-element calculation.

In addition to this central sample used for the design of the analysis, several samples are generated with varied settings and generators to estimate systematic uncertainties caused by the differences between models. To study the differences between available signal generators,  $t\bar{t}$  production is also mod-

---

<sup>1</sup>The all-hadronic  $t\bar{t}$  decay channel generates a final state (6 jets, in the “tree level picture”) that, for the sake of this analysis, is not discernible from the multijet QCD .

eled using POWHEG, interfaced both with HERWIG/JIMMY and PYTHIA, and Alpgen, interfaced with HERWIG/JIMMY.

In particular, beside the NLO prediction, the analysis has been performed using also the nominal sample of top pair events generated using the ALPGEN generator and CTEQ6L1 PDF set. The sample was generated for  $t\bar{t}$  with zero to four exclusive and five inclusive additional light partons. Parton showering and fragmentation was performed by HERWIG. The MLM parton-jet matching scheme was applied (ETCLUS 20 GeV, RCLUS 0.7, ETACCLUS 6.0) to avoid double counting of configurations generated by both the parton shower and the matrix-element calculation. The Alpgen generator provides a more precise description of the events with high jet multiplicities, as shown in Fig. 3.4 and Fig. 3.5. This phase space region is crucial for the sake of this analysis, since the  $t\bar{t}$  kinematic variables, especially the  $p_T$  Fig. 3.6, are strongly dependent on the description of the extra parton emissions. In particular, the low  $p_T$  region is strongly dependent by the parton shower modeling, in the extreme case of events generated without parton shower the spectrum is exactly  $\delta(0)$  due to the transverse momentum conservation (red line in Fig. 3.6); in the higher  $p_T$  region, on the contrary, the hard parton emission plays a major role, and thus Alpgen is expected to provide a better description.

Since none of the NLO generators for  $t\bar{t}$  production allows for variation of the amount of initial- and final-state-radiation, AcerMC samples with PYTHIA showering are generated where the ISR (PARP(67), PARP(64)), and FSR (PARP(72), PARJ(82)) parameters in PYTHIA are varied by a factor 1/2 and 2 (see Fig. 3.7 for an explanation of their meaning), centered around the Perugia 2011C tune [62]. The PDF set MRST2007LO\*\* is used in the generation of these samples.

## Chapter 3. Data and Monte Carlo samples

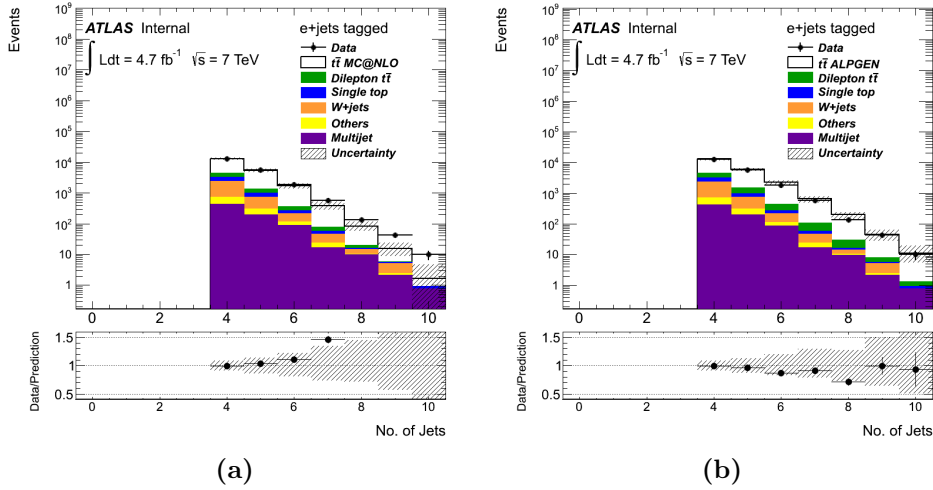


**Figure 3.4** – Number of jets spectra in the electron channel after the one-tag selection (as described in Chapter 5) using the MC@NLO generator (a) and the Alpgen generator (b) to model the signal.

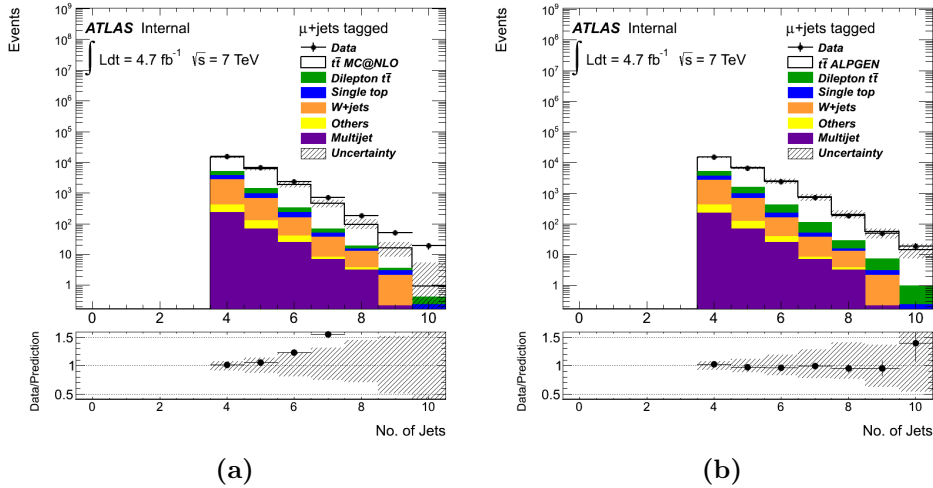


**Figure 3.5** – Number of jets spectra in the muon channel after the one-tag selection (as described in Chapter 5) using the MC@NLO generator (a) and the Alpgen generator (b) to model the signal.

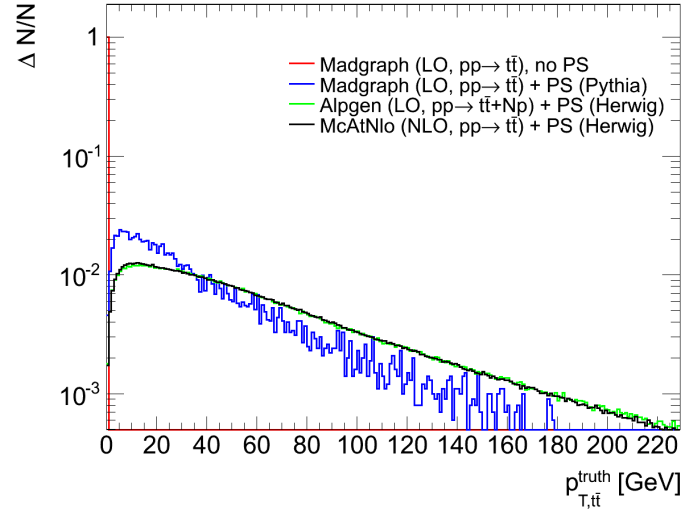


**Figure 3.6** –  $t\bar{t}$   $p_T$  spectra using Madgraph [61] without (red) and with (blue) parton shower, Alpgen+Herwig (green) and MC@NLO+Herwig (black).

- PARP(67): controls high-pt ISR branchings phase-space;  
ISR branchings with  $p_{Tevol} > m_{dip}/2 * PARP(67)$  are power suppressed by a factor  $(m_{dip}/(2p_{Tevol}))^{**2}$
- PARP(64): multiplicative factor of the mom. scale<sup>2</sup> in running  $\alpha_s$  used in ISR
- PARP(72): multiplicative factor of the  $\lambda_{QCD}$  in running  $\alpha_s$  used in FSR central param. setting is motivated by ATLAS FSR QCD jet shapes, variations correspond to \*1/2 and \*1.5 central value
- PARJ(82): FSR low-pt cutoff

**Figure 3.7** – Meaning of the Pythia parameters used for the up and down variations.

### 3.4 Background estimation

Usually, two basic categories of background processes can be defined: physics backgrounds and instrumental backgrounds. Physics backgrounds are those processes that are characterized by the same final state as the signal events. Instrumental backgrounds are those instead which mimic the signal final state due to a detector effect, resulting in a mis-identification of some of the final state objects. Although the mis-identification rates are typically very small, instrumental backgrounds can still significantly contribute to the final selected samples due to the very large production cross-sections.

Instrumental backgrounds are generally estimated using control data samples, while physics backgrounds are estimated using MC simulations, re-normalized using higher order theoretical calculations (as explained in Sect. 3.2.3) or data-driven methods. Examples of instrumental background for the  $t\bar{t}$  signal in the single lepton channel are the QCD multi-jet and  $W$ +jet processes (which might be also physics background).

The inclusive QCD process  $pp \rightarrow$  jets has a production cross-section which is about nine orders of magnitude larger than the  $t\bar{t}$  one. The jets come mainly from light quarks ( $u$ -,  $d$ -,  $s$ -quarks) or gluons;  $b$ -quark jets are produced in a few percent of these events. For semi-leptonic final states, the QCD background is sometimes referred to as “fake lepton” background. It is a consequence of the mis-identification of a jet as an isolated high energy lepton and of a mismeasurement of the  $\cancel{E}_T$  that makes the event fall into the selected sample. This is especially the case for the electron + jets selection, while for the muon + jets the contamination is mainly due to “true” non-prompt muons coming from heavy-quark decays. If  $b$ -quark jet identification is required, a further mis-identification of one of the light quark or gluon jets is also necessary in order for the event to survive all selection criteria.

The  $W$ +jets process has a production cross-section about three orders of magnitude greater than the  $t\bar{t}$  process and is the most important background for the  $t\bar{t}$  semileptonic final state. When the  $W$  decays leptonically, there are a high energy lepton and  $\cancel{E}_T$  in the event. If the  $b$ -tag requirement is dropped, this background appears as a physics background, while after a  $b$ -tag selection,  $W$ +jet events can contribute both as instrumental background, when the  $W$  is produced in association with light jets only (and therefore to pass the selection cuts one of the jets has to be mis-identified as  $b$ -jet), and as physics background, when at least one of the jets is originated from a heavy  $b$  or  $c$ -quark (the so called “ $W$  +heavy flavor” production shown in Tab. 3.7). The shapes of the distributions for  $W$ +jet events is taken from MC simulation, while their normalization is extracted from the data (exploiting the charge asymmetry in  $W$  production) since there are large theoretical uncertainties involved. These uncertainties arise since complete calculations of the  $W + 3$  jets and  $W + 4$  jets cross sections, including heavy flavor contributions, are unavailable and current estimates rely on a mixture of partial calculations at lower orders and parton shower MC models to extrapolate to larger jet multiplicities.

A related background,  $Z$ +jets, has a production cross-section roughly a factor of ten smaller than the  $W$ +jets background. It can contribute to the selected sample if the  $Z$  decays to  $e^+e^-$  or  $\mu^+\mu^-$  and one of the leptons escapes undetected giving rise to fake  $\cancel{E}_T$ . This effect is dominated by the limited geometric acceptance of the detector and is estimated using MC simulation as shown in Tab. 3.5. Moreover,  $Z \rightarrow \tau^+\tau^-$  events, when one of the  $\tau$  leptons decays leptonically and the second one hadronically, can present a very signal-like final state. Once the relevant branching fractions are included, this turns out to be a small background and is estimated from

MC.

The production of a single top quark via electroweak interactions has a production cross section about a factor of two smaller than the  $t\bar{t}$  production. These single top events have usually final states with a smaller number of jets than  $t\bar{t}$  and their contribution to the high jet multiplicity samples is small. On the contrary, in the low jet multiplicity control samples their contribution is important, especially after the  $b$ -tag requirement. The single top background is estimated using MC simulation and normalized using the theory predicted cross-section.

The diboson processes  $pp \rightarrow WW, WZ, ZZ$  have small cross-sections and usually don't contribute significantly to the high jet multiplicity samples, but their contribution is still taken into account using MC simulation normalized by using the theoretical predictions.

### 3.4.1 QCD background estimation

$t\bar{t}$  decays are selected through their high  $p_T$  leptons in the final state. While semi-leptonic electroweak processes can produce real electrons or muons (prompt leptons from  $W$  and  $Z$  decays) passing these selections, there is an additional component from mis-identified leptons or “fake leptons”, called QCD background.

The dominant sources of these fake leptons are from:

- semi-leptonic  $B$ -hadron decays;
- long lived weakly decaying states such as  $\pi^\pm$  or  $K$  mesons;
- electrons from photons conversions or direct photons;
- mis-identification of hadronic jets.

While the probability of a multi-jet event passing the selection is very low, the production cross-section for multi-jet events is orders of magnitude above that of the  $t\bar{t}$ . These background sources are also highly detector dependent. Therefore, data-driven methods are the most appropriate to estimate the rate of fake leptons in an analysis.

### **The Matrix Method**

The Matrix Method (MM), has been extensively used at the Tevatron [63] and is based on selecting two categories of events using “loose” and “tight” lepton selection requirements. This method is in principle valid for every event selection based on single-lepton identification and can be extended to di-lepton selections as well [64].

The tight lepton selection is usually the standard lepton selection used in the analysis, described in Chapter 4, while the loose one is obtained reducing some of the lepton identification requirements. In this way, all the leptons passing the tight selection (“tight leptons”) are also passing the loose lepton selection (they are “loose leptons” as well).

Based on these loose and tight lepton selections, one can distinguish between a loose and a tight event selection, differing only in the lepton identification criteria.

It is important to note that, even if the tight lepton selection is actually a subset of the loose one, this is not necessarily the case for the corresponding event selection. Indeed, if the event selection includes a lepton veto (i.e. a requirement of the form “exactly N lepton” or “no more than N leptons”), it might happen that some events are passing the tight selection without passing the loose one. This is the case when, i.e. for the  $e$ +jets selection, there are two electrons in the event, one passing the tight selection, and the other one

### Chapter 3. Data and Monte Carlo samples

---

passing the loose selection but not the tight one; this event has exactly one tight electron, and is therefore passing the tight event selection, but on the other hand it has two loose electrons, which means that it's not passing the loose event selection, which is requiring “exactly one” loose electron. In this case, these events are not considered, since the tight events must be a subset of loose events.

The number of selected events in each sample ( $N^{loose}$  and  $N^{tight}$ ) can be expressed as a linear combination of the numbers of events with real and fake leptons, in such a way that the following system of equations can be defined (hence the name “Matrix Method”):

$$\begin{aligned} N^{loose} &= N_{real}^{loose} + N_{fake}^{loose} \\ N^{tight} &= N_{real}^{tight} + N_{fake}^{tight} \end{aligned} \quad (3.2)$$

where  $N_{real(fake)}^{loose}$  and  $N_{real(fake)}^{tight}$  is the number of events passing the loose and tight selection, containing a real(fake) lepton. By defining the “real” and “fake” efficiency

$$\begin{aligned} \epsilon_{real} &= \frac{N_{real}^{tight}}{N_{real}^{loose}} \\ \epsilon_{fake} &= \frac{N_{fake}^{tight}}{N_{fake}^{loose}} \end{aligned} \quad (3.3)$$

one can re-write (3.2)

$$N^{tight} = \epsilon_{real} N_{real}^{loose} + \epsilon_{fake} N_{fake}^{loose} \quad (3.4)$$

In particular, the number of “tight” events coming from “fake” leptons (the definition of our QCD background) can be expressed by solving the system

(3.2) using (3.4) :

$$N_{fake}^{tight} = \frac{\epsilon_{fake}}{\epsilon_{real} - \epsilon_{fake}} (\epsilon_{real} N^{loose} - N^{tight}). \quad (3.5)$$

Once  $N^{tight}$  and  $N^{loose}$  are extracted from the “tight” and “loose” samples, the only missing variables are the efficiencies  $\epsilon_{real}$  and  $\epsilon_{fake}$ . Usually, both the efficiencies are dependent on the lepton  $\eta$  and  $p_T$ . The  $p_T - \eta$  grid used in this analysis is shown in Tab. 3.9. In this analysis, electrons which are in the cracks between the barrel and the endcaps of the electromagnetic calorimeter are removed, so the efficiency in those regions is set to 0.

$\eta^{grid}$	-2.47, -2.37, -2.01, -1.81, -1.52, -1.37, -0.8, -0.6, -0.1, 0, 0.1, 0.6, 0.8, 1.37, 1.52, 1.81, 2.01, 2.37, 2.47
$p_T^{grid}$ [GeV]	25, 30, 35, 40, > 45

**Table 3.9** – Binning definition in  $p_T - \eta$  space for the determination of  $\epsilon_{real/fake}$ .

To make this method actually usable in the analysis, (3.5) can be generalized in order to obtain a weight  $w_i$  to be applied to the data events passing the “loose” selection:

$$w_i = \frac{\epsilon_{fake}}{\epsilon_{real} - \epsilon_{fake}} (\epsilon_{real} isLoose(i) - isTight(i)), \quad (3.6)$$

where  $isLoose/isTight$  is a boolean value that indicates if the event passes the loose/tight selection. These weights are built in such a way that their sum running on all the data events is  $N_{fake}^{tight}$ .

**Real efficiency determination** The measurement of the lepton identification efficiency  $\epsilon_{real}$  is derived through the tag-and-probe method with a sample of  $Z \rightarrow e^+e^-$  events. The sample of  $Z$  events is selected following the same cleaning as for top studies, the only exception being that

### Chapter 3. Data and Monte Carlo samples

---

the overlap removal procedure is applied with loose leptons. No specific requirement on the amount of jet activity in the event is considered. Events with two loose leptons are selected. The tag is a well-identified lepton passing the Tight requirement.

For each pair of electrons, the invariant mass is calculated. A total of nearly two millions probes are finally available in the electron channels for the extraction of the identification efficiency. Pairs of same-sign and opposite sign charges are then considered separately.

Different background subtraction methods can be applied. They are all based on the peak structure of the invariant mass distribution:

- removal of same-sign events in the signal region (OS-SS),
- side-band method on same-sign events,
- fit using a model for the signal (Breit-Wigner convoluted with a Crystal-ball function) and for the background (convolution of a Gaussian and an exponential decay) components.

The first method assumes the lepton charges are uncorrelated in background events.

The side-band method relies on the background having a linear shape over the considered invariant mass range. In this case, the invariant mass distributions for opposite-sign and same-sign pairs at the denominator and numerator levels are divided in three regions A, B and C. The number of background events in region B and its uncertainty are estimated from the extrapolation of the side-bands A and C of the same-sign distribution.

Lastly, for the extraction of the efficiency with fits, one assumes the

functions used model well the signal and the different background components. Two fits need to be performed: one for the probe at loose level (denominator) and one for the probe at tight level (numerator). The efficiency is then computed taking the ratio of the estimated number of signal events under the Z-boson peak in the two selections.

The main systematics on the efficiency measurements are linked to the contamination of the sample of probes by background. To assess the precision of its subtraction, different variations of the probe selection have been used to change the level of the background and different methods to estimate it.

**Fake efficiency determination** The fake efficiencies are estimated in a sample with at least one jet ( $p_T > 25$  GeV) and exactly one loose lepton. A minimum distance between the jet with highest  $p_T$  and the lepton of  $\Delta R(\text{leading jet}, \text{lepton}) \geq 0.7$  is required. The efficiency  $\epsilon_{fake}$  is equivalent to the fraction of loose probe candidates passing the tight cut. It is measured in a control region with  $\cancel{E}_T < 20$  GeV in order to enhance the sample in QCD jets. Other  $\cancel{E}_T$  regions are used to estimate the corresponding systematic uncertainty.

### 3.4.2 $W$ +jets background normalization

Since the theoretical uncertainties on the estimate of the  $W$ +jets background for high jet multiplicities (especially after  $b$ -tag selection) are large, data-driven methods that combine measurements from several control sample are used.

The approach described here consists in two steps. The first step is to get an estimate of the number of  $W$ +jets events  $N_j$  after a specific selection

## Chapter 3. Data and Monte Carlo samples

---

without including any  $b$ -tagging requirement ( $W_{pretag}^{N_j}$ ) with the method described in the following section. As a second step, needed for the  $W$ +jets background estimation in a  $b$ -tag sample, the pretag estimate is extrapolated to the corresponding  $b$ -tag selection ( $W_{tagged}^{N_j}$ ) by multiplying it by an appropriate factor  $f_{tag}^{N_j}$  (“ $W$ -tagging rate”). In such a way, one can write:

$$W_{tagged}^{N_j} = W_{pretag}^{N_j} \cdot f_{tag}^{N_j} \quad (3.7)$$

### The Charge Asymmetry Method

The “Charge Asymmetry” approach is based on the fact that, in  $pp$  collisions, while the  $t\bar{t}$  production is associated to the same number of positive and negative lepton candidates (is “charge-symmetric”), the  $W$ +jets production is characterized by an excess of positive leptons (is “charge-asymmetric”). Infact, positively charged  $W$ -bosons can be produced from parton level processes such as  $u\bar{d} \rightarrow W^+$  or  $c\bar{s} \rightarrow W^+$  whose cross section depends upon products of PDFs such as  $u(x_1) \cdot \bar{d}(x_2)$ . On the other hand, the production of negatively charged  $W$ -bosons from, e.g.,  $d\bar{u} \rightarrow W^-$  depends upon the  $d(x_1) \cdot \bar{u}(x_2)$  PDF product. The PDFs of up and down valence quarks are different in a proton, hence there is a charge asymmetry.

The cross-section ratio,  $R = \sigma(pp \rightarrow W^+)/\sigma(pp \rightarrow W^-)$  is relatively well understood [65]. The main theoretical uncertainty on  $R$  is due to the PDF uncertainties, so that  $R$  is predicted to within a few percent at LHC energies, i.e. better than the prediction of the cross section for  $W$ -bosons produced in association with three or more jets. One can therefore use the theoretical prediction for  $R$  to measure the  $W$ +jets background for the  $t\bar{t}$  production in the  $l$ +jets channel.

The amount of  $W$ -bosons in a given sample can be expressed as:

$$(W^+ + W^-) = \left( \frac{W^+ + W^-}{W^+ - W^-} \right)_{MC} \cdot (D^+ - D^-) = \frac{R + 1}{R - 1} \cdot (D^+ - D^-) \quad (3.8)$$

where  $D^+(D^-)$  are the data events with a positive (negative) lepton, and  $R$  is evaluated using the kinematic selection of the MC sample.

The formula is valid due to the fact that the processes  $t\bar{t}$ , QCD and  $Z$ +jets are symmetric, so that  $W^+ - W^- \approx D^+ - D^-$  is a good approximation. However, other important processes like single top and diboson production are charge-asymmetric as well, so they have to be taken into account and subtracted from  $D^+$  and  $D^-$ , according to the sign of the reconstructed lepton.

### **$W$ +jets flavor composition**

Like the overall  $W$ +jets normalization, also its heavy flavor composition, i.e. the fraction of  $Wb\bar{b}$ ,  $Wc\bar{c}$  and  $Wc$  events, suffers from a big uncertainty from MC simulation. Knowing these heavy flavor fractions (HFFs) in  $W$ +jets is essential to extract the  $W$ +jets background after a  $b$ -tag selection.

The determination of the  $W$  HFF in the high jet multiplicity region is difficult due to the significant amount of  $t\bar{t}$  contamination. A common solution to the problem is to measure the HFF in the 1- and 2-jet bins and extrapolate to the signal region using the MC simulation.

To determine the HFFs in the 1- and 2-jet bins in data, a “tag-counting” method is used. Basically, it consists in a comparison of the pretag and  $b$ -tagged samples between data and MC. Counting the number of events in data and subtracting the number of expected non- $W$  background events ( $t\bar{t}$ , single top,  $Z$ +jets, diboson and QCD) in different jet multiplicity and  $b$ -tag bins,

### Chapter 3. Data and Monte Carlo samples

---

keeping from MC some constraint (the ratio between the HFFs in 1- and 2-jet bins, the ratio between  $Wb\bar{b}$  and  $Wc\bar{c}$  fractions and the tagging probability for each specific flavor type), a set of data-driven correction factors for the different flavor fractions in the MC simulation can be extracted.

This method suffers of the following systematic uncertainties:

- cross-section uncertainties for  $t\bar{t}$ , single top,  $Z$ +jets and diboson;
- QCD normalization uncertainty;
- $b$ - and light-tagging efficiency uncertainty;
- jet energy scale.

The second step consists in extrapolating the obtained HFF scale factors (SFs) from the 1- and 2-jet bin to higher jet multiplicity bins. The HFFs in MC are simply scaled by the same SFs, and an uncertainty obtained from MC is assigned. To assess the MC uncertainties associated with the HFF extrapolation, ALPGEN generator parameters are varied in both  $W$ +light and heavy flavor simultaneously, and the results are checked using NLO event generator.

This analysis is performed for the full 2011 dataset, combining the  $e$ +jet and  $\mu$ +jet samples to reduce the statistical uncertainty. Results and related uncertainties are summarized in Tab. 3.10 and Tab. 3.11 respectively.

jet bin	$K_{bb}$	$K_c$	$K_{light}$
1 jet	1.156	1.106	0.976
2 jet	1.104	1.095	0.966
3 jet	1.097	1.088	0.960
4 jet	1.091	1.082	0.955

**Table 3.10** – Heavy flavor fraction in the  $W$ +jets sample for the 2011 dataset.

Source	$K_{bb}(\%)$	$K_c(\%)$	$K_{light}(\%)$
$t\bar{t}$ cross section	16/-16	-5.1/5.2	-1.1/1.2
$K_{bb}$ (stat)	-3.2/3.2	0.39/-0.39	0.39/-0.39
$K_c$ (stat)	0.34/-0.34	-1.6/1.6	0.34/-0.34
$K_{light}$ (stat)	0.52/-0.51	0.52/-0.51	-0.2/0.2
$W_{bb}W_{cc}$ jet	9.2/-8	-8.4/7.2	0.61/-0.5
$W_c$ jet	28/-50	-24/44	1.5/-3
$Wt$ cross section	17/-17	-4.6/4.7	-1.4/1.4
Single top cross section	6.9/-6.9	-1.5/1.5	-0.7/0.7
$Z$ cross section	-4/4.5	-1.4/1.4	0.95/-1
$WW/ZZ/WZ$ cross section	0.14/-0.14	-0.025/0.024	-0.015/0.016
QCD	6.9/-7.6	1.3/-1.3	-1.4/1.5
Pratagged QCD	-11/12	-0.0039/-0.32	1.7/-1.8
Jet Energy Scale	-9.6/11	-2/-0.43	2.1/-1.9
Symmetrized jet energy resolution	2.3/-2.3	-4.6/4.6	0.82/-0.82
$b$ -tag efficiency	74/-65	-17/17	-7.2/5.9
$b$ -tag mis-identification	-2.6/2.6	1.1/-1.1	0.15/-0.15
Total uncertainty	+85/-88	+49/-32	+7.3/-8.7

**Table 3.11** – Main uncertainties on the heavy flavor fraction in the  $W$ +jets sample for the 2011 dataset.



---

---

## CHAPTER 4

---

### OBJECT DEFINITIONS AND SELECTION

In this chapter, I'll describe the way the physics objects are reconstructed in ATLAS. Assuming a “leading order” picture of the topology of the events under study (Fig. 4.1), the reconstructed objects of interest are:

- the jets from the hadronic decay of the  $W$  (and  $b$ -jets originating directly from the top);
- the leptons (electrons, and muons);
- the missing transverse energy ( $\cancel{E}_T$ ) carried out by the invisible neutrino.

Only the objects used in this analysis are considered here, and only general reconstruction and identification algorithms used in ATLAS are described, while the specific kinematic cuts chosen for the analysis are discussed in Sect. 5.1. A detailed description and definition of the objects used in this analysis can be found in [66].

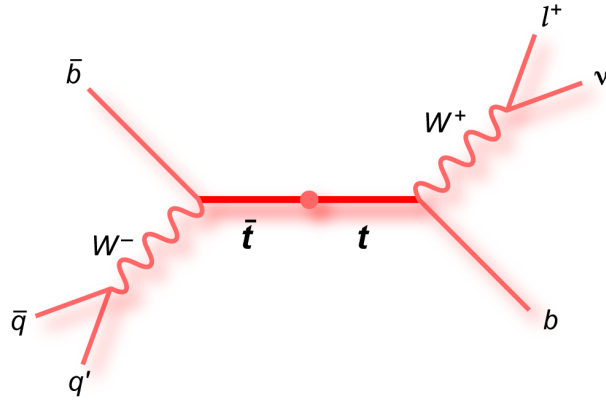


**Figure 4.1** – Leading order Feynman diagram of the “semileptonic”  $t\bar{t}$  topology.

## 4.1 Jets

Hadronic particles deposit their energies mainly in the calorimeter system. In an attempt to resolve particles coming from the hard scatter, these energy deposits may be grouped into objects called jets.

The “anti- $k_T$ ” algorithm [67] with  $\Delta R = 0.4$  is used to reconstruct the jets. Jets are required to have  $p_T > 25 \text{ GeV}$  and  $|\eta| < 2.5$ . Since reconstructed electrons might also be reconstructed as jets in the calorimeter, any jet overlapping with a selected electron within a cone of  $\Delta R = 0.2$  is removed from the list of jets.

A cut on the “jet vertex fraction” variable is applied: this variable represents the fraction of the tracks associated to the jets that are matched to the primary vertex. The threshold is 0.75 and this cut is needed to avoid the contamination due to the high-pileup.

Jet quality criteria are applied to identify those jets not associated to in-time real energy deposits in the calorimeters (bad jets) due to various sources as hardware problems in the calorimeter, the LHC beam conditions, and the atmospheric muon-ray induced showers. When a bad jet is found, the whole

event is discarded.

### 4.1.1 Jet reconstruction algorithms

In ATLAS the so called anti- $k_T$  algorithm [67] has been adopted as default. It is part of the wider class of “Cluster Algorithms”, based upon pair-wise clustering of the initial constituents.<sup>1</sup> Two “distances” are defined:  $d_{ij}$  between objects  $i$  and  $j$  and  $d_{iB}$  between object  $i$  and the beam ( $B$ ):

$$d_{ij} = \min(k_{T,i}^{2p}, k_{T,j}^{2p}) \cdot \frac{\Delta R_{ij}^2}{\Delta R_0^2} \quad (4.1)$$

$$d_{iB} = k_{T,i}^{2p}, \quad (4.2)$$

where  $\Delta R_{ij}^2 = (\phi_i - \phi_j)^2 + (y_i - y_j)^2$  ( $\phi_i$  and  $y_i$  being the azimuthal angle and rapidity of object  $i$ ) and  $k_{t,i}$  is the transverse momentum of  $i$ . The clustering proceeds by identifying the smallest distance among all the entities in the event:

- if it is  $d_{ij}$ ,  $i$  and  $j$  are combined in a single objects,
- if it is  $d_{iB}$ ,  $i$  is considered as a single jet and it is removed from the list of entities.

This algorithm relies on two parameters:  $\Delta R_0$  and  $p$ . For large values of  $\Delta R$ , the  $d_{ij}$  are smaller, and thus more merging takes place before jets are complete (jets get “wider”). The  $p$  parameter, instead, causes a preferred

---

<sup>1</sup>For the definition of these constituents, it’s not very convenient to use individual calo cell signals, because they can be negative, due to noise effects, and because it is difficult to determine the source of the signal without using also the information from neighbor cells. Cells have thus to be collected into larger objects like towers or topological clusters (topoclusters). The jets considered in this thesis are built starting from topoclusters. Unlike calorimeter towers, that are built projecting the cell energy onto a two-dimensional grid in  $\eta - \phi$  space, topological clusters reconstruct three-dimensional energy deposits. Starting from seed cells with high signal-to-noise ratio, neighboring cells with a signal-to-noise ratio above a certain threshold are iteratively added to the cluster.

## Chapter 4. Object definitions and selection

---

ordering of clustering: if the sign of  $p$  is positive, clusters with lower energy will be merged first, if it's negative the clustering will start from higher energy clusters. In the anti- $k_T$  algorithm  $p = -1$  (hence the name “anti”), meaning that objects with high relative momentum  $k_T$  are merged first.

### Jet energy calibration

The ATLAS calorimeters are non-compensating, and the energy of hadronic particles is underestimated. In order to correctly reconstruct the energy of the jets, a calibration procedure is needed. ATLAS has developed several calibration schemes with different levels of complexity.

The jets used in this analysis are calibrated using the simplest scheme, the so called “EMJES” because it is applied on top of the EM scale. The goal of the Jet Energy Scale (JES) calibration is to correct the energy and momentum of jets measured in the calorimeter, using as reference the kinematics of the corresponding jets in the MC simulation. The jet energy scale calibration is derived as a global function depending on  $p_T$  and  $\eta$ . JES calibration is one of the major sources of systematic uncertainty and will be further discussed in Sect. 5.2.3.

Furthermore, a pile-up subtraction scheme that accounts for the effect of both in-time and out-of-time pile-up is applied to jets at the EM scale. This correction is parametrized according to the number of primary vertices in an event ( $N_{PV}$ ) and the number of average interactions in a luminosity block ( $\mu$ ), in bins of jet pseudorapidity  $\eta$ .

## Jet energy resolution

The jet energy resolution (JER) measured with the di-jet balance<sup>2</sup> and the bi-sector<sup>3</sup> techniques in data and Monte Carlo agrees within uncertainty. For this reason, no systematic smearing is applied to jets in Monte Carlo simulation for central value measurements. The uncertainty on the jet energy resolution is evaluated by smearing jets according to the systematic uncertainties of the resolution measurement in the full 2011 dataset.

### 4.1.2 $b$ -tagging algorithms

The aim of  $b$ -tagging algorithms is to identify jets containing  $b$ -flavored hadrons. For each selected jet they provide  $b$ -weights reflecting the probability that it originates from a  $b$ -quark. The discrimination of  $b$ -quark jets from light quark jets is made possible mainly by the relatively long life time of  $b$ -flavored hadrons, resulting in a significant flight path length  $L$  of the order of some millimeter. This leads to measurable secondary vertices and impact parameters of the decay products.

The transverse impact parameter  $d_0$  is defined as the distance in the transverse plane  $(x, y)$  between the point of the closest approach of a track to the primary vertex (i.e. the impact parameter) and the primary vertex itself; the

---

<sup>2</sup>The di-jet balance method for the determination of the jet  $p_T$  resolution is based on momentum conservation in the transverse plane. It works properly in the ideal case where only two jets with the same particle level transverse momentum are present in the event. Jets at particle level are defined as those composed by stable interacting particles with a lifetime longer than 10 ps but excluding muons and neutrinos, that have not yet been passed through the simulation of the ATLAS detector.

<sup>3</sup>The bi-sector method is based on the definition of an imbalance (transverse) vector,  $\mathbf{P}_T$ , which is defined as the vector sum of the two leading jets in the di-jet event. This vector is projected along an orthogonal coordinate system in the transverse plane,  $(\psi, \eta)$ , where  $\eta$  corresponds to the azimuthal angular bi-sector of the di-jet system while the  $\psi$ -axis is defined as the one orthogonal to the  $\eta$ -axis. For a perfectly balanced di-jet event,  $\mathbf{P}_T = 0$ .

## Chapter 4. Object definitions and selection

---

longitudinal component  $z_0$  is the z-coordinate of this point. Various  $b$ -tagging algorithms are used in ATLAS, based on these discrimination variables ( $L$ ,  $d_0$  and  $z_0$ ), on secondary vertex properties and on the presence of leptons within  $b$ -quark jets. Each tagging algorithm defines a “weight”  $w$ , associated to the probability for a given jet to have been originated from a  $b$ -quark. For each tagging algorithm, different “working points”, i.e. different threshold on the  $w$  variable, can be used. The choice of the working point sets the tagging efficiencies for  $b$ -,  $c$ - and light quark jets.

For the sake of this analysis, the MV1 algorithm with a working point of 70% efficiency is used. The MV1 algorithm is a neural network-based algorithm that uses the output weights of SV1 and JetFitterCombNN [68] as inputs.

**SV1** The SV1 tagging algorithm is based on the reconstruction of secondary vertices from tracks within a jet. The search of the secondary starts by building all two-track pairs that form a good vertex, using only tracks associated to the jet and far enough from the primary vertex. Vertices compatible with a primary vertex or material interaction are rejected. All tracks from the remaining two-track vertices are combined into a single inclusive vertex. The vertex decay length significance  $L/\sigma(L)$  measured in 3D and signed with respect to the jet direction can be used as a discriminating variable between  $b$ -jets and light jets. To increase the discriminating power, the tagging algorithm SV1 takes advantage of three of the vertex properties: the invariant mass of all tracks associated to the vertex, the ratio of the sum of the energies of the tracks in the vertex to the sum of the energies of all tracks in the jet, and the number of two-track vertices. These variables are combined using a likelihood ratio technique. SV1 relies on a 2D-distribution of

the two first variables and a 1D-distribution of the number of two-track vertices. In addition the distance  $\Delta R$  between the jet axis and the line joining the primary vertex to the secondary one is used.

**JetFitterCombNN** The JetFitterCombinedNN algorithm is the combination of two tagging algorithms: JetFitter and IP3D. JetFitter exploits the topology of weak  $b$ - and  $c$ -hadron decays inside the jet, using a Kalman Filter to define a common line on which the primary vertex and the  $b$ - and  $c$ -hadron decay vertices lie, as well as their position on this line, giving an approximated flight path for the  $b$ -hadron. The discrimination between  $b$ -,  $c$ - and light jets is based on a likelihood which uses the masses, momenta, flight-length significances and track multiplicities of the reconstructed vertices as inputs.

The IP3D algorithm uses a likelihood ratio technique in which input variables are compared to predefined smoothed and normalized distributions for both the  $b$ - and light jet hypotheses, obtained from Monte Carlo simulation. The distributions in this case are two-dimensional histograms of the signed transverse impact parameter significance  $d_0/\sigma(d_0)$  and longitudinal impact parameter significance  $z_0/\sigma(z_0)$  of tracks, taking advantage of the correlations between the two variables.

## 4.2 Electrons

Electron reconstruction and identification algorithms are designed to achieve both a large background rejection and a high and uniform efficiency for isolated high-energy ( $E_T > 20$  GeV) electrons over the full acceptance of the detector. Isolated electrons need to be separated from hadron decays in QCD jets and from secondary electrons originating mostly from photon conversions

## Chapter 4. Object definitions and selection

---

in the tracker material.

Electron reconstruction is based on the identification of a set of clusters in the EM Calorimeter [69]. For each reconstructed cluster, the reconstruction algorithm tries to find a matching track in the Inner Detector. While the energy of the electron is determined using the calorimeter information, the more precise angular information from the ID track is used to evaluate the trajectory.

The baseline ATLAS electron identification algorithm relies on variables which deliver good separation between isolated electrons and fake signatures from QCD jets. These variables include information from the calorimeter, the tracker and the matching between tracker and calorimeter. Cuts are applied on the energy in the Had Calorimeter inside the electron cone, on the shape of the electromagnetic shower, on the track impact parameter, on the number of hits in the different layers of the ID, on the difference between the calorimeter cluster and the extrapolated track positions in  $\eta$  and  $\phi$ , on the ratio of the cluster energy to the track momentum ratio. Electrons passing all the following identification requirements are called tight electrons, while loose and medium electrons pass only some of the listed requirements:

- “LAr error == 0” (0:OK, 1:Noise Burst, 2:Data Integrity Error + time veto around identified noise bursts);
- “tight++” ID flag: this flag is built by looking at the shower shapes in the calorimeter, the matching of the cluster to the associated track and at the number of hits in the inner part of the tracker. The tight++ operating point provides efficiencies  $\approx 78\%$  for  $Z$  electrons with a small dependence on the number of interactions/crossing;
- author== 1 or author== 3. author== 1 means that the object has

been found by only the standard (cluster based) electron reconstruction algorithm. `author==3` means that the object has been found by the standard (cluster based) and the track-based algorithms;

- $|z_0(vs\ PV)| < 2\text{mm}$ :  $z_0(vs\ PV)$  is the projection on the  $z$ -axis of the track impact parameter respect to the Primary Vertex;
- $E_T > 25\text{ GeV}$ , where  $E_T = E_{cluster} / \cosh \eta_{track}$
- $0 < |\eta_{cluster}| < 2.47$  excluding  $1.37 < |\eta_{cluster}| < 1.52$ : this takes in account the EM calo acceptance, as described in Sect. 2.2.3;
- isolation cuts ‘Etcone20’ and ‘Ptcone30’ @ 90%: ‘Etcone20’ is a variable built summing the  $E_T$  deposited in the calorimeter towers in a cone of radius  $\Delta R = 0.2$  around the electron position. ‘Ptcone30’ is an analogue variable built by summing the  $p_T$  of the tracks in the ID around a cone of  $\Delta R = 0.3$ . The working points for these cuts are tabulated in a  $\eta - p_T$  grid, characterized by an efficiency of 90%;
- $\Delta R(e, jet) > 0.4$  after the electron-jet overlap removal (as explained in Sect. 4.1), since the electron scale factors from are calibrated for  $\Delta R(e, jet) > 0.4$ ;
- `OQ_flag&1446==0`. The Object Quality Flag is a 32bit word: for each electron all the cells of the cluster are analyzed and if any important problem is found, then the corresponding bit is set to 1.

### 4.2.1 Electron reconstruction performance

Besides improving the quality of the electron reconstruction, the isolation cut is very effective in selecting those electrons that are coming from the

## Chapter 4. Object definitions and selection

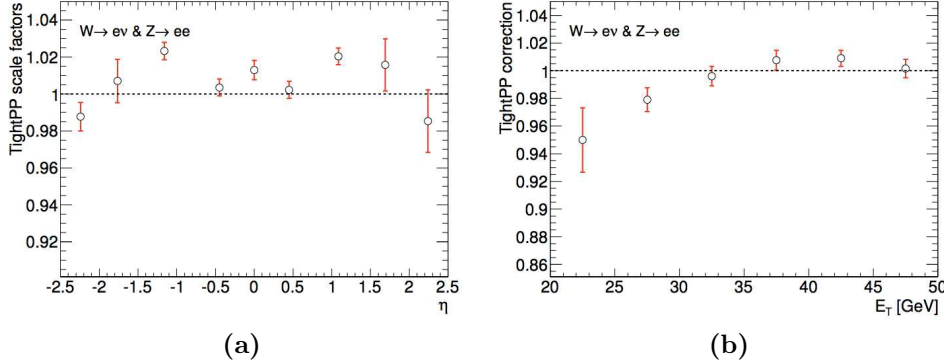


**Figure 4.2** – Electron “tight++” scale factor as a function of the  $\eta$  (a) and  $E_T$  (b) of the electron.

$W$ -boson decay while removing the electrons coming from the hadron decays within a hadronic jet. The latter electrons are expected to be characterized by electromagnetic clusters having on average a greater energy, because they are likely to be contaminated by the others nearby calorimeter energy deposits.

The electron reconstruction efficiencies are measured with the Tag & Probe method, using  $Z \rightarrow e^+e^-$  samples. The scale factors, defined as  $\epsilon_{data}/\epsilon_{MC}$  are calculated in 9  $\eta$  bins. In particular, the “Tight++” scale factors are binned in 9  $\eta$  bins with  $E_T$ -corrections in 6  $E_T$  bins, as shown in Fig. 4.2. The main source of the systematic uncertainties comes from the background subtraction in data for both sample, and is much more in the endcap regions than in the barrel ones.

The dependence of the reconstruction efficiencies on the pile-up conditions can be evaluated by integrating them over  $\eta$  and  $E_T$  and measuring them as a function of the number of reconstructed vertices, as shown in Fig. 4.3.

The energy scales of electrons are calculated using  $Z \rightarrow e^+e^-$ ,  $J/\psi \rightarrow e^+e^-$  or  $E/P$  studies with isolated electrons from  $W \rightarrow e\nu$ . The data energy scale is corrected as a function of  $\eta_{cl}$ ,  $\phi_{cl}$  and  $E_T$  of the electrons and systematic uncertainties are within  $\pm(1 - 1.5)\%$  for the  $|\eta_{cl}| < 2.47$  range. In this re-

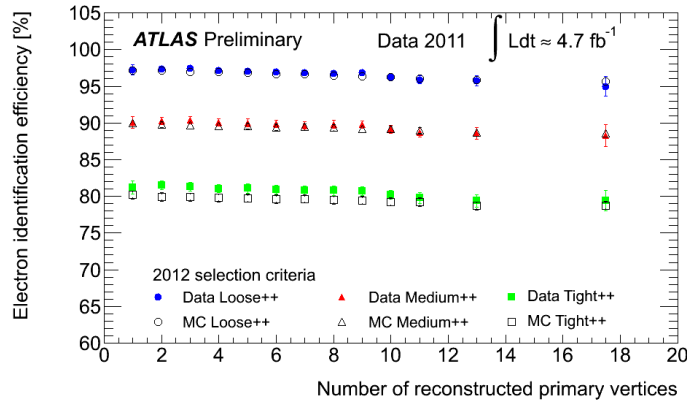


**Figure 4.3** – Electron reconstruction efficiencies shown for different number of reconstructed primary vertices, going from 1 to 10 in bins of unit size and then wider bins 11-12, 13-14 and 15-20.

gion the dominant uncertainties arise from the interactions with the detector material and the presampler energy scale, but there are also uncertainties on the event selection, pile-up, and hardware modeling. ling.

## 4.3 Muons

Muon reconstruction is based on information from the Muon Spectrometer, the Inner Detector and the calorimeters. Different kinds of muon candidates can be built, depending on how the detector information is used in the reconstruction, as shown schematically in Fig. 4.4. In the analysis described in this thesis, the so called combined muons are used. The information from the MS and from the ID is combined through a fit to the hits in the two sub-detectors to derive the muon momentum and direction.

The two main reconstruction algorithms used in ATLAS are STACO [70] and MuId [71]. Both muon combination algorithms create combined tracks out of pairs of MS-only and ID-only tracks. To do this, a  $\chi^2$  match is used and corrections are made for energy loss in the calorimeters. However, the

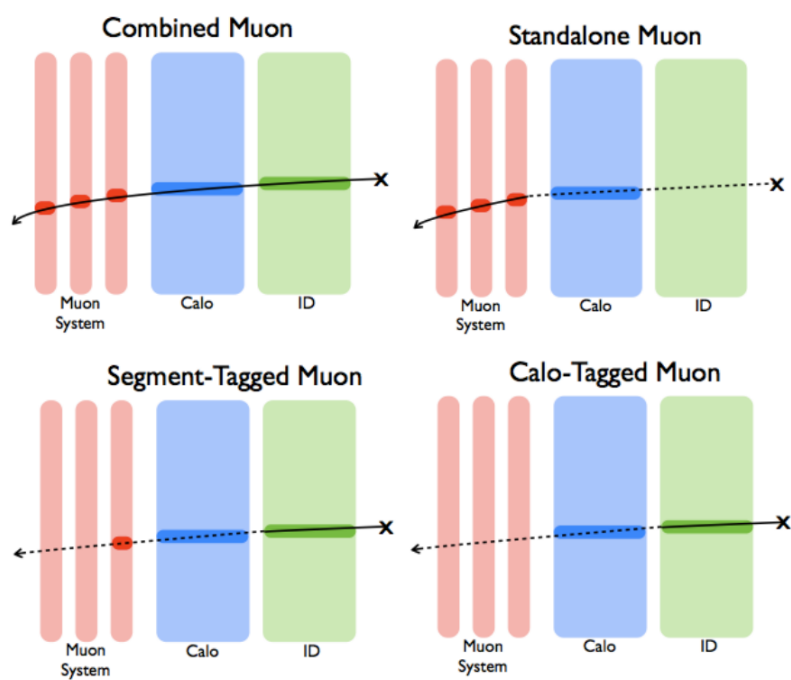


**Figure 4.4** – Schematic representation of the different muon reconstructions methods.

two algorithms handle the combined track in a slightly different way:

- STACO does a statistical combination of the track vectors to obtain the combined track vector;
- MuId re-fits the combined track, starting from the ID track and then adding MS measurements.

The two algorithms have shown very similar performances and can be both used for the analysis. In the analysis described in this thesis, muons reconstructed with MuId algorithm are used and selected applying the following requirements:

- “tight” muon ID flag. The tight flag requires the candidate muon to be:
  - combined (see Fig. 4.4);
  - OR standalone at  $|\eta| > 2.5$  AND has at least three MDT+CSC stations;
  - OR fitted by MuGirl<sup>4</sup> with extended track AND (at least two MDT+CSC stations OR less than six MDT+CSC holes on track);
- additional hit requirements in the Inner Detector;
- $|z_0(vs PV)| < 2\text{mm}$ ;
- isolation:
  - $Ptcone30 < 2.5\text{ GeV}$ ;

---

<sup>4</sup>MuGirl performs a search for segments (short tracklets inside one layer of the muon spectrometer) and tracks in the muon spectrometer using an inner detector track as seed. If the full track refit is successful a Combined Muon is made. If the track refit is not successful a Tagged Muon is made.

## Chapter 4. Object definitions and selection

---

- $Etcone20 < 4 \text{ GeV}$
- $\Delta R(muon, jet) > 0.4$ , where only jets with  $p_T > 25 \text{ GeV}$  and  $|jvf| > 0.75$  are considered.

### 4.3.1 Muon reconstruction performances

In the muon reconstruction, the introduction of an isolation condition is particularly effective in separating the muons originating from the boson decay (prompt muons) from the ones coming from the decays of hadrons in hadronic jets. Fig. 4.5a, shows the number of reconstructed muons as a function of the transverse energy (not associated to the muon) in a  $\Delta R = 0.2$  cone (etcone20) for two classes of reconstructed muons: muons coming from a  $Z$ -boson decay (red line histogram) and muons originating from an hadronic jet (green filled histogram). For the signal, the process  $Z \rightarrow \mu\mu$  has been used, because of its very clear signature. In addition, a constraint on the invariant mass of the reconstructed di-muon system has been imposed: its difference from the very well known  $Z$  boson mass must be at maximum 15 GeV. From this plot, one can see that a cut at  $etcone20 < 4 \text{ GeV}$  is very effective in isolating prompt muons and rejecting most of the muons coming from hadronic jets. The data (black dots) confirm the goodness of the simulations.

Muons originated within jets can also have associated tracks in the inner detector. For the same considerations of above, we will consider the sum of the transverse momentum of all the tracks within a radius of  $\Delta R = 0.3$  (ptcone30) around the muon, and this sum must be lower than 2.5 GeV, as shown in Fig. 4.5b. The efficiencies of the cuts based on those two variables are shown in Fig. 4.6.

In addition to the cuts on the isolation quantities, there is also a re-

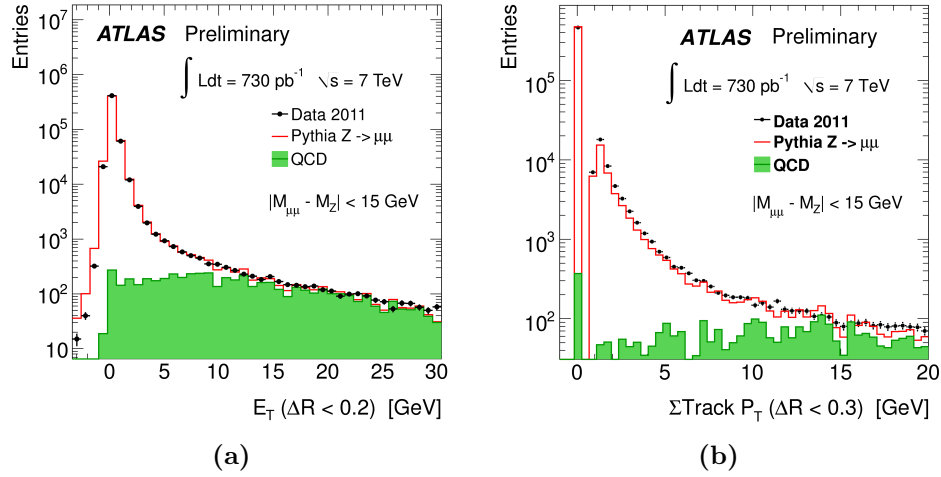


**Figure 4.5** – Number of muons with respect to the etcone20 (a) and ptcone30 (b) variable.

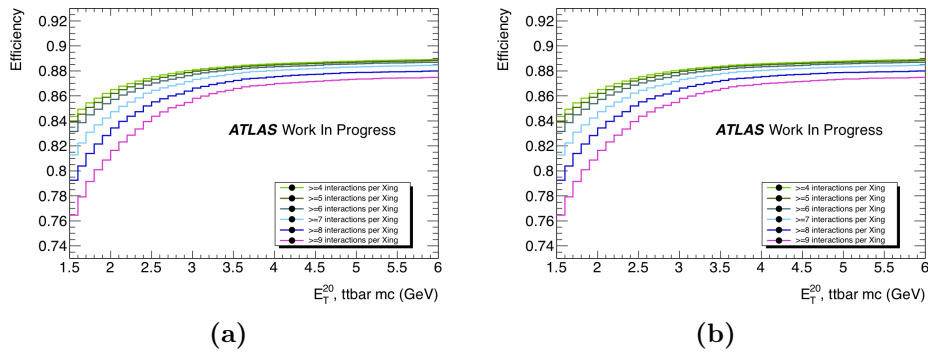


**Figure 4.6** – Efficiency of the etcone20 (requiring ptcone30 < 2.5 GeV) (a) and ptcone30 (requiring etcone20 < 4 GeV) (b) selections, evaluated on the  $t\bar{t}$  MC sample [66].

## Chapter 4. Object definitions and selection

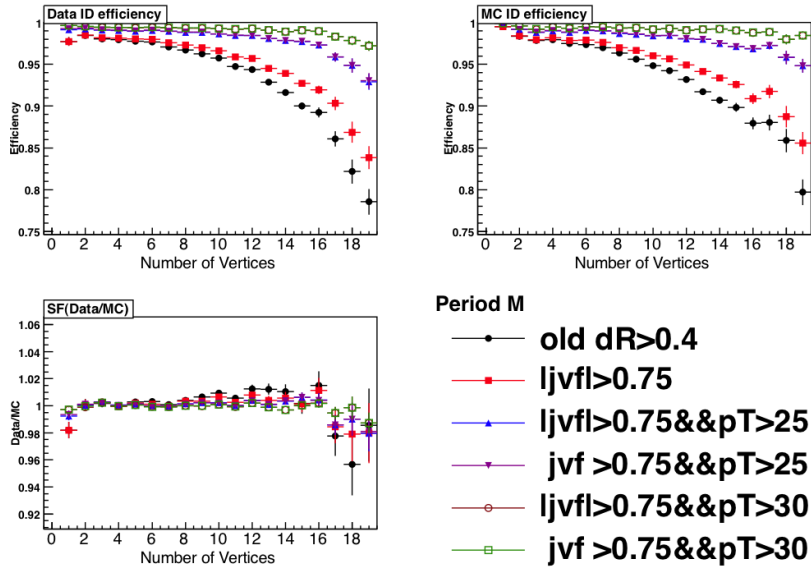


**Figure 4.7** – Efficiency of the possible  $\Delta R(\mu, j)$  requirements as a function of the number of vertices in the event, measured with the tag-and-probe method in  $Z$  events.

quirement on the muon-jet separation  $\Delta R(\mu, j) > 0.4$  from any jet with  $p_T > 25$  GeV. In the high luminosity periods, because of the high pileup, this cut becomes inefficient due to additional low  $p_T$  jets from the additional  $pp$  interactions. To solve this issue, a study has been performed on the efficiency of the  $\Delta R$  requirement as measured in the  $Z$  events along with variations of the requirement where the jet vertex fraction (JVF) selection is applied and where the jet  $p_T$  threshold is increased. As shown in Fig. 4.7, the pileup dependence is mostly removed by using only jets with  $p_T > 25$  GeV and  $|JVF| > 0.75$ .

The resulting scale factors, defined as the ratio  $\epsilon_{data}/\epsilon_{MC}$ , after these requirements are evaluated separately in the B-I, J-K and L-M data periods and are within 1% of unity, as shown in Fig. 4.8.

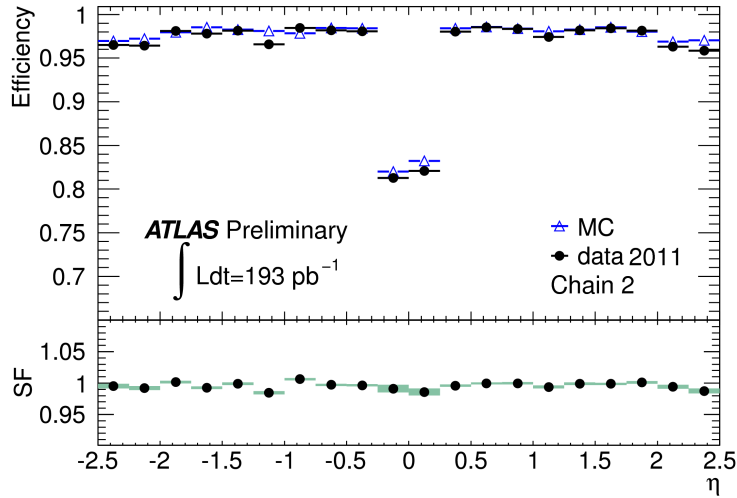


Figure 4.8 – Muon reconstruction efficiency as a function of  $\eta$ .

## 4.4 Missing Transverse Energy

Neutrinos, as well as possible BSM particles which are expected not to interact with the detector, can be reconstructed using the difference between the initial state and final state total momentum. In hadron colliders, the initial momentum of the colliding partons along the beam axis is not known a priori,<sup>5</sup> so that the amount of total missing energy cannot be determined. However, the initial momentum transverse to the beam axis is in good approximation zero, so that the missing transverse energy ( $\cancel{E}_T$ ) can be measured.

The measurement of the  $\cancel{E}_T$  in an event with a top quark pair decaying semileptonically gives the possibility to infer the energy of the neutrino, coming from the leptonic  $W$ -boson decay.

The  $\cancel{E}_T$  reconstruction presently used in ATLAS for physics analysis, includes contributions from transverse energy deposits in the calorimeters, cor-

<sup>5</sup>Also the final total momentum along the beam direction cannot be determined due to final state particles which escape detection at very large values of  $|\eta|$  inside the beam pipe.

## Chapter 4. Object definitions and selection

---

rections for energy losses in the cryostat and measured muons. Its components along the coordinate axes in the  $xy$ -plane are:

$$\cancel{E}_{x(y)} = \cancel{E}_{x(y)}^{calo} + \cancel{E}_{x(y)}^{cryo} + \cancel{E}_{x(y)}^{\mu} \quad (4.3)$$

therefore

$$\cancel{E}_T = \sqrt{\cancel{E}_x^2 + \cancel{E}_y^2}. \quad (4.4)$$

The calorimeter term in (4.3) is built starting from the calorimeter cells over the range  $|\eta| < 4.9$ . Only cells belonging to topological clusters are considered. The most refined scheme developed in ATLAS calibrates cells energy on the base of the reconstructed high-pT physics object they belong to: electrons, photons, hadronically decaying  $\tau$ -leptons, jets and muons. Depending on the type of associated object, the cells are separately and independently calibrated. The calorimeter term components is then evaluated by summing different terms:

$$\cancel{E}_{x(y)}^{calo} = \cancel{E}_{x(y)}^e + \cancel{E}_{x(y)}^{\gamma} + \cancel{E}_{x(y)}^{\tau} + \cancel{E}_{x(y)}^{jets} + \cancel{E}_{x(y)}^{\mu(cal)} + \cancel{E}_{x(y)}^{CellOut}, \quad (4.5)$$

where each term is calculated from the negative sum of cell energies calibrated according to the corresponding objects. The  $\cancel{E}_{x(y)}^{\mu(cal)}$  term is the contribution to  $\cancel{E}_{x(y)}^{calo}$  lost by muons in the calorimeter. The  $\cancel{E}_{x(y)}^{CellOut}$  term is calculated from the cells in topoclusters which are not included in the reconstructed objects.

The  $\cancel{E}_{x(y)}^{\mu}$  term in (4.3) is directly calculated using the information from the ID and MS for the isolated muons in  $|\eta| < 2.5$ , and using the information from the MS for non-isolated muons or muons outside the ID  $\eta$  range.

The cryostat between the LAr barrel electromagnetic calorimeter and the Tile barrel hadronic calorimeter has a thickness of about half an interaction length and it can lead to significant energy losses in hadronic showers. The  $\cancel{E}_{x(y)}^{cryo}$  term, calculated by using the correlation of energies between the last layer of the LAr calorimeter and the first layer of the Had calorimeter, takes into account this lost energy.

#### 4.4.1 $\cancel{E}_T$ reconstruction performance

##### Control samples

The performance of the  $\cancel{E}_T$  detection has been studied comparing data and Monte Carlo simulations. Three main selection criteria were used to perform the comparisons. In all cases the object selections were done in the standard way as described in the previous sections. The event selection was done as follows:

1. semileptonic  $t\bar{t}$  decay:
  - exactly one electron or muon passing single lepton trigger;
  - electron channel:  $\cancel{E}_T > 30$  GeV,  $m_T^W > 30$  GeV;
  - muon channel:  $\cancel{E}_T > 20$  GeV,  $m_T^W > 60$  GeV;
  - at least four jets;
  - no b-tagging requirements.
2. Control sample with  $W \rightarrow l\nu$  ( $l = e, \mu$ ) plus jets:
  - same lepton selection requirements  $t\bar{t}$  semileptonic selection;
  - $\cancel{E}_T > 35$  GeV and  $M_T^W > 50$  GeV;
  - exactly two jets.

## Chapter 4. Object definitions and selection

---

3. Control sample with  $Z \rightarrow ll$  ( $l = e, \mu$ ):

- single lepton trigger;
- two oppositely charged, same flavor leptons;
- $|M_{ll} - M_Z| < 15 \text{ GeV}$ .

### Resolution of $\cancel{E}_T$

The resolution of  $\cancel{E}_T$  in semileptonic  $t\bar{t}$  events featuring real  $\cancel{E}_T$  has been studied using the simulated  $t\bar{t}$  sample and applying the selection described above. It is expected to be dependent on the scalar sum of the transverse energy of the cells in the calorimeter ( $\sum E_T$ ). For events with real  $\cancel{E}_T$ , one can define the “true” missing transverse energy originating from all the non-interacting particles in the event,  $E_{x,y}^{NonInt}$ .

The resolutions on  $\cancel{E}_x$  and  $\cancel{E}_y$  are thus estimated from a Gaussian fit to the  $\cancel{E}_x(\cancel{E}_y) - E_x^{NonInt}(E_y^{NonInt})$  distributions in bins of  $\sum E_T$ . The two resolutions  $\sigma(\cancel{E}_x)$  and  $\sigma(\cancel{E}_y)$ , as expected, are found to be equivalent, and the final resolution is taken from a Gaussian fit to the combined residual distribution. The resolutions for the  $t\bar{t}$  semileptonic sample in the electron and muon channels are shown in Fig. 4.9.

## 4.5 Trigger

In this section, a description of the triggers used to select the events for the analysis is presented.

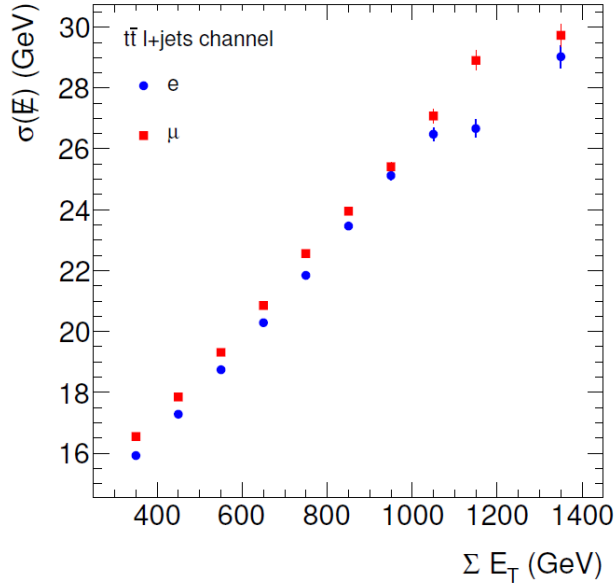


**Figure 4.9** – The  $\cancel{E}_{x,y}$  resolution in bins of  $\Sigma E_T$  for the  $t\bar{t}$  semileptonic selection in the electron and muon channels.

### 4.5.1 Electron trigger

The Level 1 (L1) electron triggers operate on reduced granularity ( $0.1 \times 0.1$  in  $\eta \times \phi$ ) calorimeter trigger towers which cover the range  $|\eta| < 2.5$ . A central cluster of four towers is formed in the electromagnetic and hadronic calorimeters, along with a ring of 12 towers around this central cluster. The ring is used to select candidates using isolation criteria (if needed) by cutting on the amount of energy deposited around the central cluster. At Level 2 (L2), electromagnetic clusters are formed, tracking is then performed for the first time, and, finally, the reconstructed cluster is matched to a track. In the final stage, the Event Filter (EF), tracking and cluster determination is performed with more accurate algorithms, further refining the trigger decision.

Because of different running conditions, different triggers are used for different data taking periods. In the selection used in this analysis, “EF-e20-medium”

## Chapter 4. Object definitions and selection

---

trigger chain has been chosen for periods from B to H, and “EF-e22-medium” for the I to M periods. The requirements are:

- an EM cluster at the L1, with  $E_T > 14$  GeV;
- a ID track match at L2;
- an EF electron with  $E_T > 20$  GeV (22 GeV in I-M data taking periods).

### 4.5.2 Muon trigger

The L1 muon trigger consists of fast electronics establishing coincidences between hits of different detector layers of the muon system inside programmed geometrical windows. The size of the window defines the transverse momentum interval corresponding to the deflection of the muon in the toroidal magnetic field. One of six programmable  $p_T$  thresholds is assigned to the candidate.

The L2 processing consists of three reconstruction steps applied to full granularity data of the region defined by L1. First, the muon candidate is reconstructed in the muon spectrometer. Then inner detector tracks are reconstructed around the muon candidate. Both are combined to form the L2 muons upon which the trigger decision is based. Currently only the  $p_T$  of the muon candidate is checked. The muon reconstruction in the Event Filter is done using offline algorithms.

For the muon channel the “EF-mu18” trigger chain is used. This requires the following prescriptions:

- a first trigger at L1 with a muon with  $p_T > 10$  GeV (L1\_MU10);
- a combination at L2 with an Inner Detector track;
- at the EF the event must have a combined muon with  $p_T < 18$  GeV.

### **Muon trigger scale factors**

The efficiency of the muon triggers (`mu18` and `mu18_medium`) is measured through the Tag-and-Probe method applied to  $Z$  data and Monte Carlo samples. This efficiency is parametrized as a function of muon  $\phi$  and  $\eta$  and the data-taking period, since it varies during the run because of hardware issues in individual trigger chambers. The measured scale factors are shown in Fig. 4.10 and Fig. 4.11. The scale factors are split into the three data taking periods: B-I, J-K and L-M.

The statistical uncertainty on these scale factors is typically 1% per bin and is due principally to the  $Z$  statistics. The systematic uncertainty is estimated by varying the Tag-and-Probe selections and is typically 1% per bin. Regarding the data taking period L, it is important to note that there is a set of data where the trigger efficiency in the barrel is systematically lower because of a timing problem in the RPC. The scale factors for the two different RPC configurations in period L are shown in Fig. 4.12.

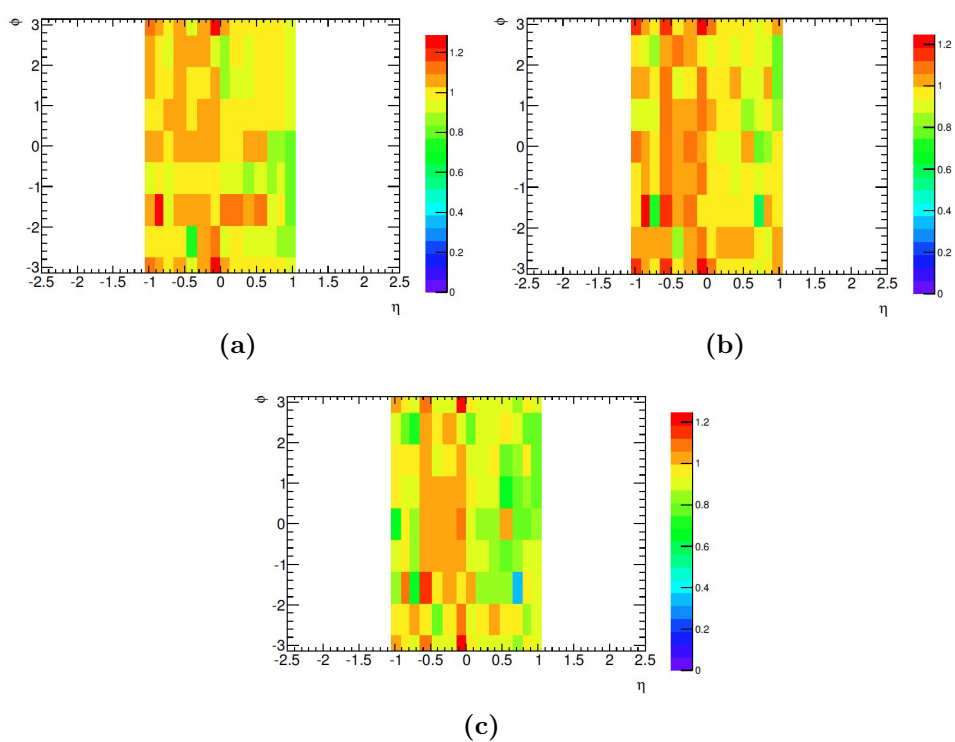


**Figure 4.10** – Trigger scale factors in the barrel for (a) mu18 trigger in periods B-I, (b) the mu18 medium trigger in periods J-K and (c) the mu18 medium trigger in periods L-M.

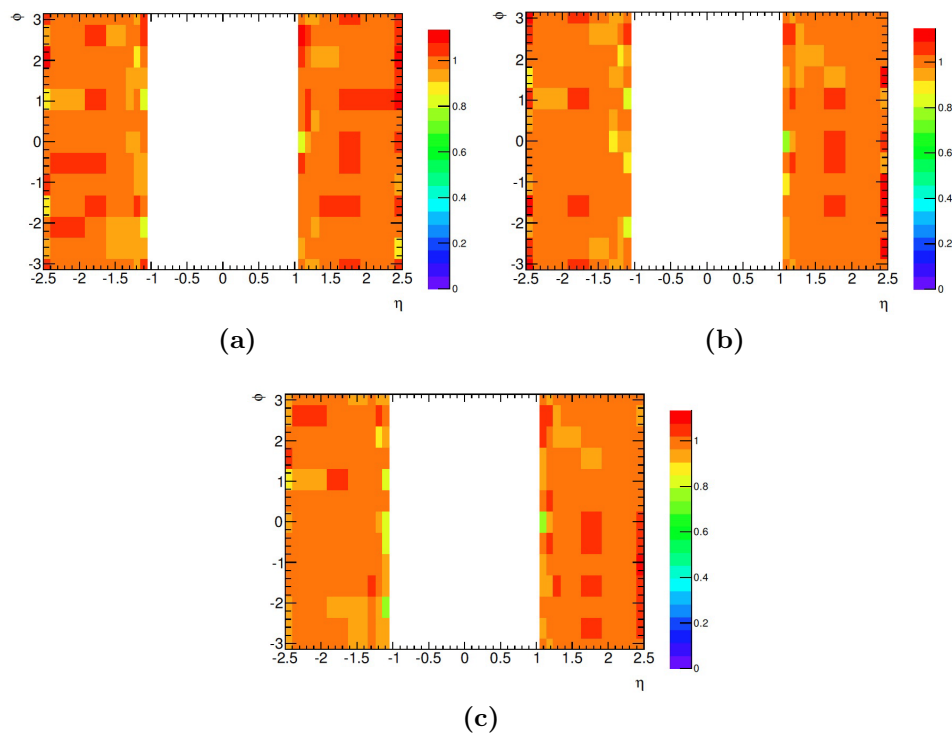


**Figure 4.11** – Trigger scale factors in the endcaps for (a) mu18 trigger in periods B-I, (b) the mu18 medium trigger in periods J-K and (c) the mu18 medium trigger in periods L-M.

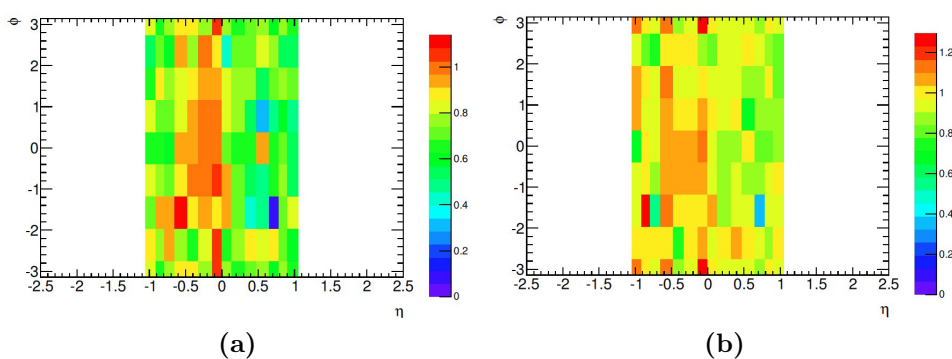


**Figure 4.12** – Trigger scale factors in the barrel for the mu18 medium trigger in (a) period L data with the wrong RPC timing configuration (runs 189205-189610) and (b) the remaining period L data.



---

---

## CHAPTER 5

---

# EVENT SELECTION AND SYSTEMATIC UNCERTAINTIES

After having discussed in Chapter 4 the reconstruction of the various objects entering the analysis, the trigger requirements and the signal and background Monte Carlo samples, the event selection requirements can be described.

The event selection cuts in the electron and muon channels have been “symmetrized” (with an exception for the trigger requirements) in order to produce comparable yields and distributions.

### 5.1 Selection cuts

Using the object definitions described in the previous sections, the event selection requirements for both electron and muon channels, after the trigger requirements, are:

- one primary vertex with more than four tracks coming from it;

## Chapter 5. Event selection and systematic uncertainties

---

- one, and only one, good electron/muon with  $p_T > 25$  GeV;
- no good lepton of the other flavor with  $p_T > 15$  GeV;
- lepton must match the corresponding leptonic trigger object;
- there must be no bad jet in the events;
- at least four jets;
- missing transverse energy greater than 30 GeV;
- $W$  boson transverse mass greater than 35 GeV;
- at least one jet tagged as b-jet.

The  $W$  boson transverse mass is a special variable, built using the neutrino and the lepton momentum on the transverse plane (for the neutrino,  $\cancel{E}_T$  is used), that helps to discriminate between the signal from the QCD background events, and it's defined as:

$$m_T(W) = \sqrt{2p_T^l p_T^\nu - \cos(\phi^l - \phi^\nu)}. \quad (5.1)$$

The choice to base the analysis on the one-btag selection, in stead of the more obvious two-tags selection, is due to the still poor knowledge of the uncertainties on the two-tags efficiencies. Some preliminary studies on this matter are presented in Appendix C.

Tab. 5.1 shows the yields for both channels, applying the pretag (no  $b$ -tag requirement) and tag selections.

## 5.2 Systematic uncertainties

Uncertainties can be classified into three main classes:

	Pretag		Tag	
	$e$ +jets channel	$\mu$ +jets channel	$e$ +jets channel	$\mu$ +jets channel
$t\bar{t}$ single lepton	16208	13964	19330	16628
$t\bar{t}$ dilepton	2019	1765	2332	2039
Single top	1434	1147	1699	1355
$W$ + jets	12943	2246	17985	3053
$Z$ + jets	2574	397	1247	206
Diboson	225	45	256	50
QCD	4996	3872	975	340
Total prediction	40339	21012	43827	23673
Data	38987	20910	45909	25063

**Table 5.1** – Event yield in the two channels (electron and muon) in the pretag (no  $b$ -tag requirement) and one tag selection. The  $t\bar{t}$  generator used is Mc@NLO.

- signal modeling, which are the systematics affecting the simulation of the hard-process, the parton shower and the PDF;
- background modeling, which are the systematics affecting the estimates made by the data-driven methods;
- detector modeling. All the uncertainties due to the non-perfect understanding of the detector belong to this class.

### 5.2.1 Signal modeling

As discussed in Sect. 3.3, different event generators with possible different settings are compared to check the dependence of the analysis on the specific event simulation. The following sources are considered as systematic uncertainties in the  $t\bar{t}$  sample generation:

**MC generation** The effect of using different NLO or LO MC generators is considered comparing the standard sample generated with MC@NLO, with samples generated with POWHEG and Alpgen. The same parton shower, Herwig, has been used for both the generators. The largest

## Chapter 5. Event selection and systematic uncertainties

---

difference between MC@NLO and Alpgen and MC@NLO and Powheg is taken as a (symmetric) systematic uncertainty.

**Parton shower** the effect of different showering models is taken into account by comparing the results using POWHEG+HERWIG and POWHEG+-PYTHIA. The full difference of those two predictions is symmetrized and taken as uncertainty.

**Initial and final state radiation** The uncertainty is estimated as 1/2 of the difference between the Acer+Pythia samples with the “up” and “down” parton shower settings, as shown in Sect. 3.3. These samples use the variations suggested by the data in the rapidity gap analysis [72].

**PDF** The impact of the choice of parton density functions (PDF) in simulation was studied by reweighting the events by different NLO PDF sets according to PDF4LHC working group recommendations [73]. For the calculation of uncertainties, the envelope provided by the central values and PDF+ $\sigma$ s errors from the MSTW08, CT10 and NNPDF2.0 PDFs has been used. The extremum (min and max) of all variations is taken and the half of the interval is taken as the uncertainty. This is also called the envelope Fig. 5.1. For the three main PDFs there exists also different methods to evaluate the PDF uncertainty:

- CTEQ66/CT10: symmetric Hessian, in addition reduce the uncertainty by 1.645 to correspond to 68% C.L. errors (these PDF sets are shipped with the 90% C.L. errors);
- MSTW2008nlo68cl: asymmetric Hessian;
- NNPDF20: sample Standard deviation.

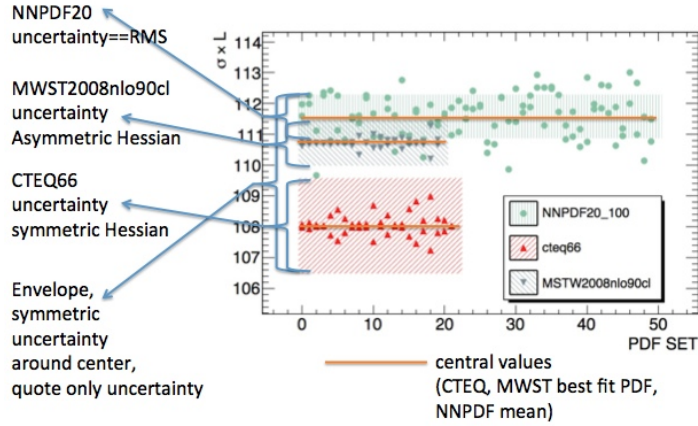


**Figure 5.1** – Definition of the PDF uncertainty envelope (data from the “dilepton” analysis in the  $ee$  channel).

For the Hessian method there is a symmetric and asymmetric version. The result for the cross section with both methods is similar, the choice was symmetric version for CTEQ and asymmetric for MSTW. The idea behind this is that a PDF has  $n$  (uncorrelated) parameters and hence each parameter can be varied independently by  $+/-1\sigma$  and a new PDF is calculated. This is basically what should be propagated then to the observable  $X$ . The outcome using the central value PDF is called  $X_0$ , the outcome of  $X$  using the error PDF is  $X_i^{+/-}$  where  $i$  is one of the parameters varied of  $+/-1\sigma$ . This uncertainty is calculated as follows:

- Symmetric Hessian:

$$\Delta X = \frac{1}{2} \sqrt{\sum (X_i^+ - X_i^-)^2}; \quad (5.2)$$

- Asymmetric Hessian:

$$\begin{aligned} \Delta X^+ &= \sqrt{\sum (X_i^+ - X_0)^2} & \text{if } X_i > X_0 \\ \Delta X^- &= \sqrt{\sum (X_i^- - X_0)^2} & \text{if } X_i < X_0. \end{aligned} \quad (5.3)$$

### 5.2.2 Background modeling

#### *W*+jets background

Systematics related to the modeling of the *W*+jets normalization are of several sources. In general, the shape is taken from tree-level Alpgen simulation, with additional hard-parton emission included, matched to the partons generated by the parton shower using some cone radius, which is varied as one systematic source. After applying theory scale-factors (with their uncertainties) accounting for the NLO/LO total cross-section difference, data-driven scale factor is applied, based on the measurement of the charge asymmetry on the *W*+jet events, as explained in Sect. 3.4.2. Those uncertainties are  $\pm 28\%$  in the muon channel and  $\pm 27\%$  for the electron channel.

#### QCD background

The QCD multijet has been evaluated by loosening the lepton isolation and using signal and fake efficiencies to pass the tight isolation criteria as shown in Sect. 3.4.1. The uncertainty on the normalization of this background component has been accounted for by varying its contribution by 20% and 50%, for the muon and the electron channel, respectively.

### 5.2.3 Detector modeling

#### Jets

**Jet energy scale** The determination of the JES is a rather challenging task in the difficult environment of an hadron-hadron collider. While several methods are proposed such as using  $\gamma$ +jet events to propagate the electromagnetic scale to the hadronic scale, the jet energy scale depends on a variety of detector and physics effects. This includes non-linearities

in the calorimeter response due, for example, to energy losses in dead material, hardware problems of the detector, and additional energy due to the underlying event and the pile-up. Energy lost outside the jet cone can also affect the measured jet energy. Effects due to the initial and final state radiation (ISR/FSR) modeling could also affect the jet energy scale but they are evaluated separately.

The uncertainty on the energy scale has been analyzed with the full 2011 dataset. It takes into account several sources, like the effect of dead material, the known area where the calorimeters is affected by hardware problems, but also the effect of the different behavior of jets with different energies.

This leads the uncertainty on JES to change with the transverse momentum of the jet, but also change from region to region of the calorimeter. In Fig. 5.2 there is an example of the  $p_T$  dependence of the JES for a fixed pseudorapidity value ( $\eta = 0.5$ ).

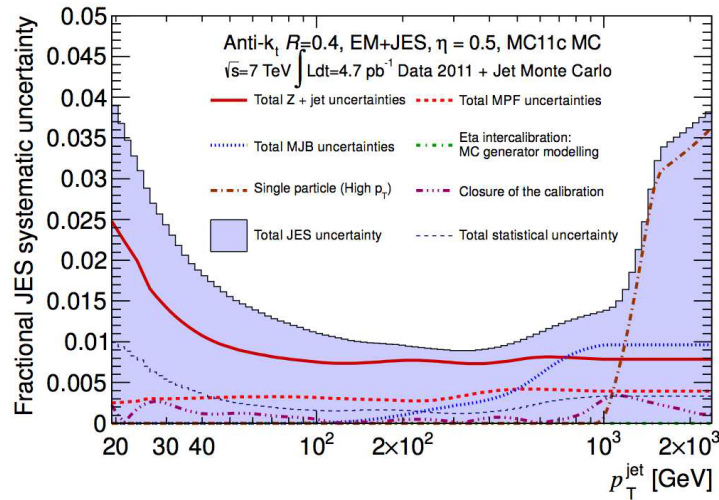


**Figure 5.2** – JES uncertainty for anti- $k_t$   $\Delta R = 0.4$  jets calibrated with the EM+JES scheme for the full 2011 dataset.

## Chapter 5. Event selection and systematic uncertainties

---

**Jet energy resolution** As shown in Sect. 4.1, the energy resolution of jets was measured in dijet events and agrees with predictions from simulations within 10%.

**Jet reconstruction efficiency** The jet reconstruction efficiency was estimated using minimum bias and QCD dijet events. An uncertainty of 2% was assigned based on the agreement between efficiencies measured in data and simulations.

***b*-tagging scale factors** The *b*-tagging efficiencies and mis-tag rates for the MV1-tagger have been measured in data [74, 75]. Jet  $p_T$ -dependent scale factors, applied to simulations to match the data, have uncertainties which range from 5% to 15%.

### Leptons

**Lepton reconstruction** The mis-modeling of muon (electron) trigger, reconstruction and selection efficiencies in simulations were corrected for by scale factors derived from measurements of the efficiency in data.  $Z \rightarrow \mu\mu$  ( $Z \rightarrow ee$  and  $W \rightarrow e\nu$ ) decays were used to obtain scale factors as functions of the lepton kinematics. The uncertainties were evaluated by varying the lepton and signal selections and from the uncertainty in the evaluation of the backgrounds. Systematic uncertainties at the level of a 1% were found for both cases.

**Lepton momentum scale and resolution** The  $Z \rightarrow ll$  processes were used to measure the lepton momentum scale and resolution. Correction factors and associated uncertainties were derived to match the simulation to observed distributions in collision data.

### Missing transverse energy

The uncertainties from the energy scale and resolution corrections on leptons and jets are propagated into the calculation of the missing transverse energy. Additional uncertainties are added from contributions of calorimeter cells not associated to any jets and soft jets ( $7 \text{ GeV} < p_T < 20 \text{ GeV}$ ) due to the uncertainty on the description of the pileup conditions.

### 5.2.4 Luminosity

The luminosity was measured from Van Der Meer scans. His uncertainty was estimated to be 3.7%. This uncertainty is applied on all non-normalized differential cross section measurements.

## 5.3 Control plots

In order to verify whether the measurements are well described by the Monte Carlo simulation and whether the analysis is done correctly it is useful to check the distribution of some physical quantities. Many control plots have been performed separately for the electron channel and for the muon channel. In the plots, the distribution obtained by the real data are represented by the black points, while the Monte Carlo simulation corresponds to a series of colored histograms. The uncertainty band is built from the systematic uncertainties described in Sect. 5.2. The binning for each plot has been calculated using the “quantile” approach: each bin is required to contain  $\approx 10\%$  of the total events; in this way the statistical uncertainties are almost the same in each bin. In order to avoid flat distributions, the bin content is then normalized to the bin width.

In the following plots, MC@NLO has been used to generate the signal

## Chapter 5. Event selection and systematic uncertainties

---

events. In Appendix A the same plots, using the Alpgen generator for the signal sample, are presented.

In general, the distributions are well described by the Monte Carlo simulation, as shown by the ratio present in the bottom part of each plot. In this ratio the black dots are the ratio between data and MC@NLO, while the green band represents the uncertainty.

### 5.3.1 Jet-related plots

The number of jets spectra have already been showed in Sect. 3.3.

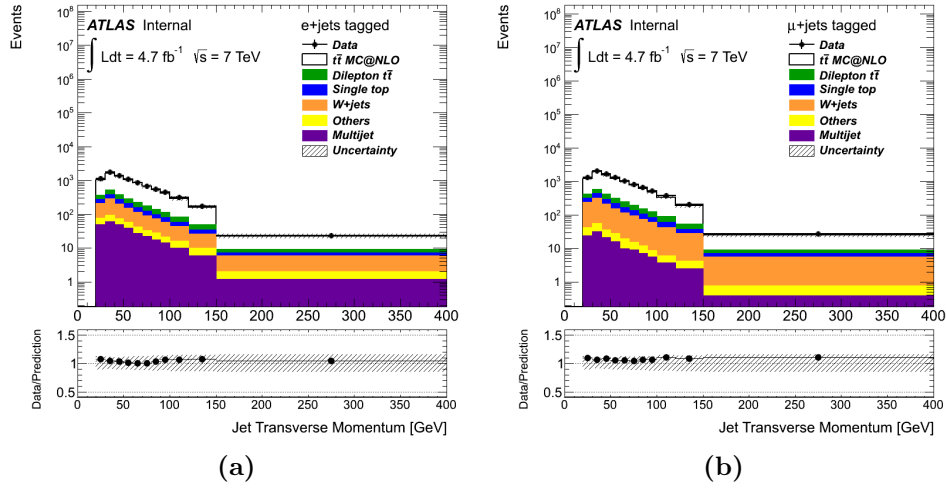


**Figure 5.3** – Jet  $p_T$  spectra for the electron (a) and muon channels (a) after the one-tag selection.

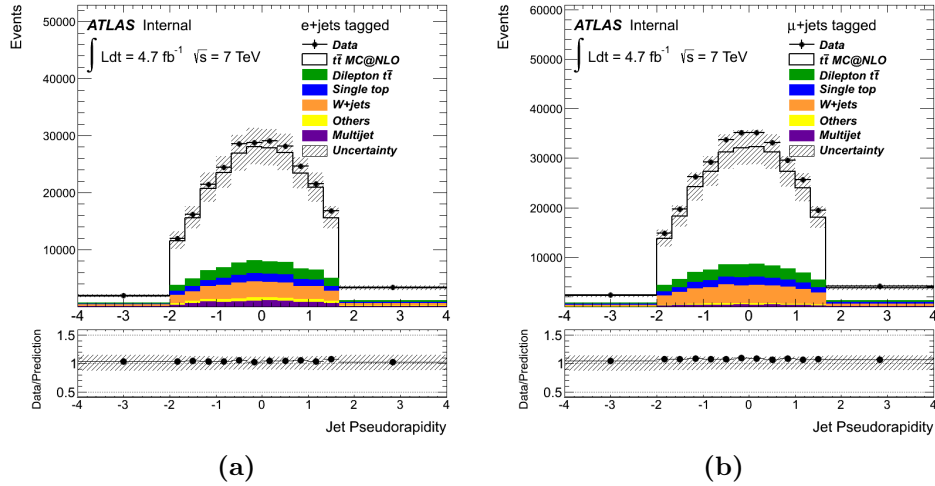


**Figure 5.4** – Jet  $\eta$  spectra for the electron (a) and muon channels (a) after the one-tag selection.

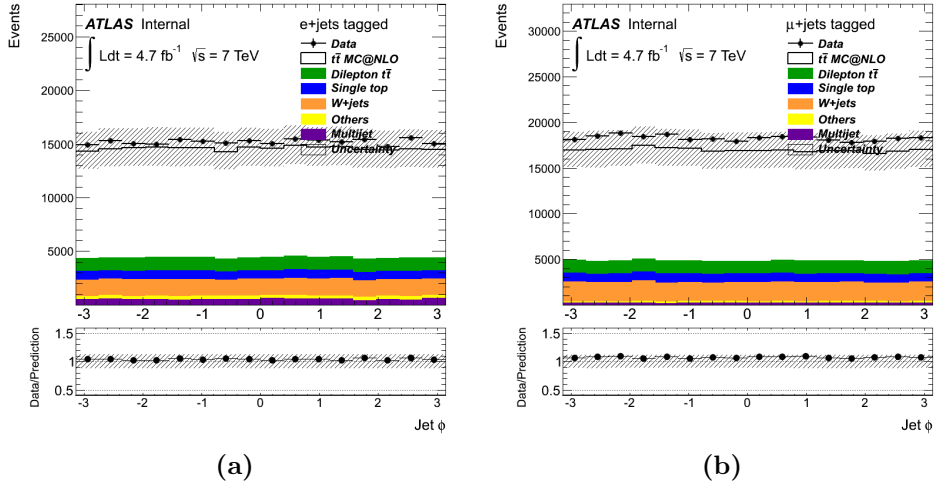
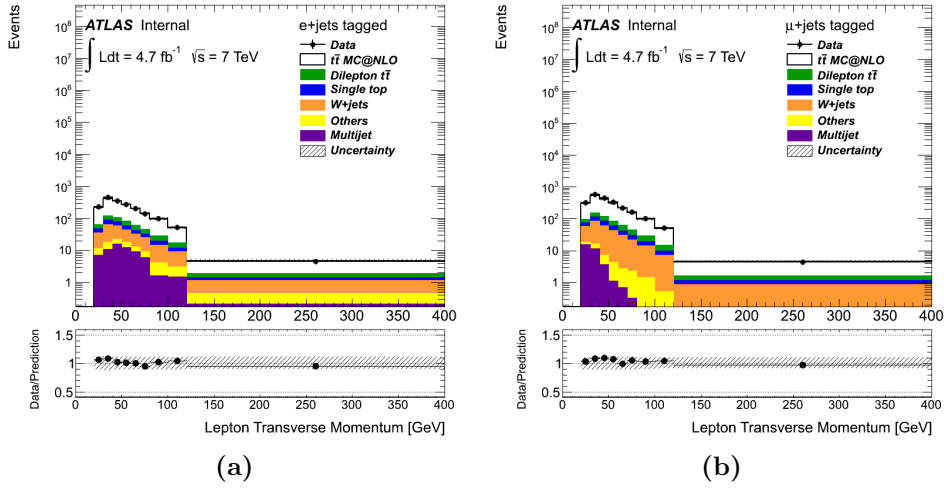
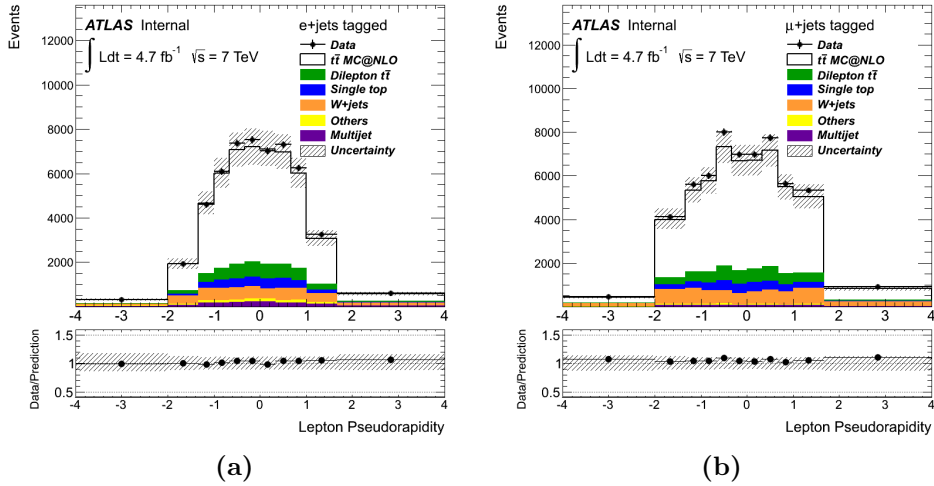


Figure 5.5 – Jet  $p_T$  spectra for the electron (a) and muon channels (a) after the one-tag selection.

### 5.3.2 Lepton-related plots



**Figure 5.6** – lepton  $p_T$  spectra for the electron (a) and muon channels (a) after the one-tag selection.



**Figure 5.7** – lepton  $\eta$  spectra for the electron (a) and muon channels (a) after the one-tag selection.

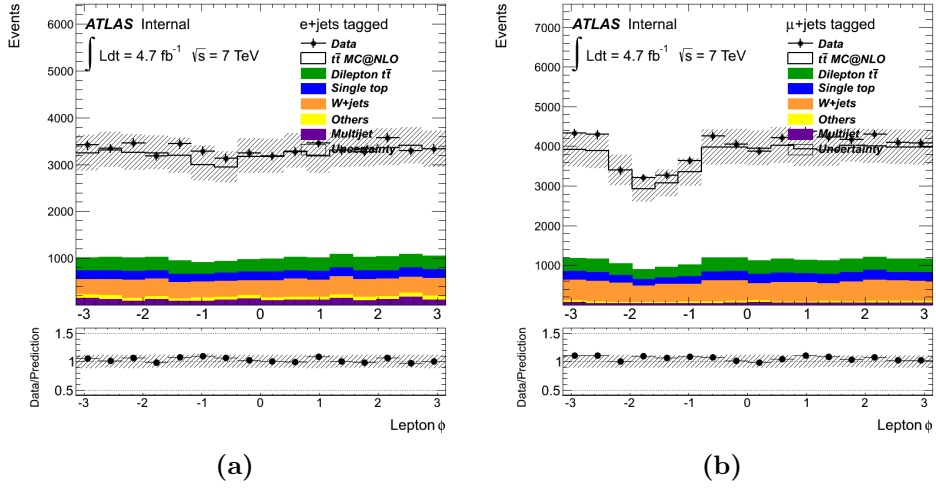
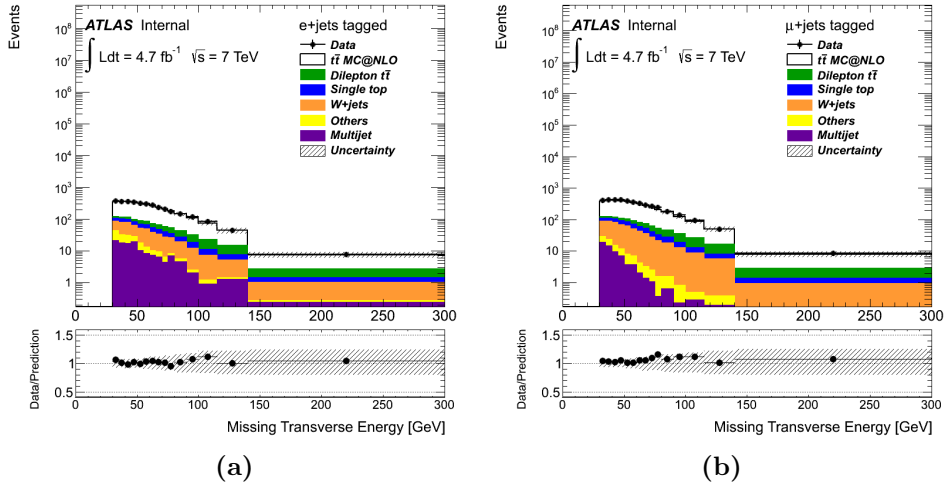
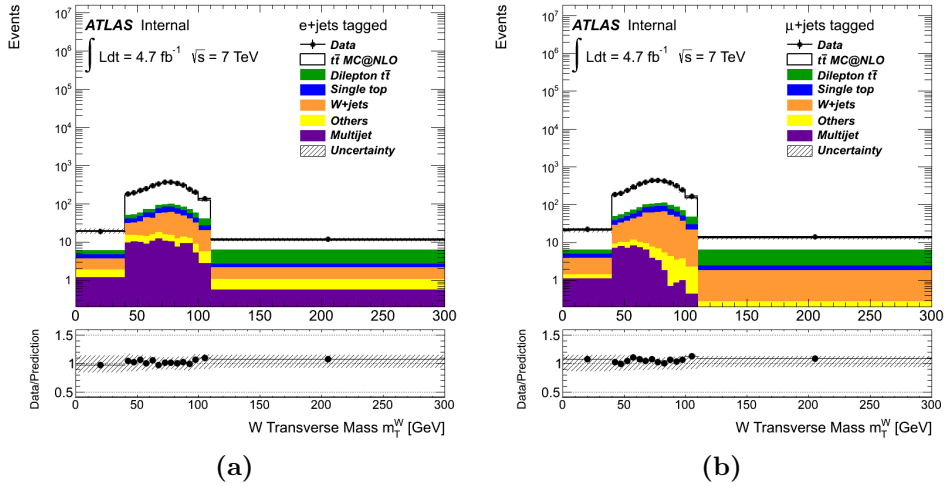


Figure 5.8 – lepton  $p_T$  spectra for the electron (a) and muon channels (a) after the one-tag selection.

### 5.3.3 $\cancel{E}_T$ -related plots



**Figure 5.9** – Missing transverse momentum spectra for the electron (a) and muon (b) channel after the one-tag selection.



**Figure 5.10** –  $W$  transverse mass (defined in (5.1)) spectra for the electron (a) and muon (b) channel after the one-tag selection.

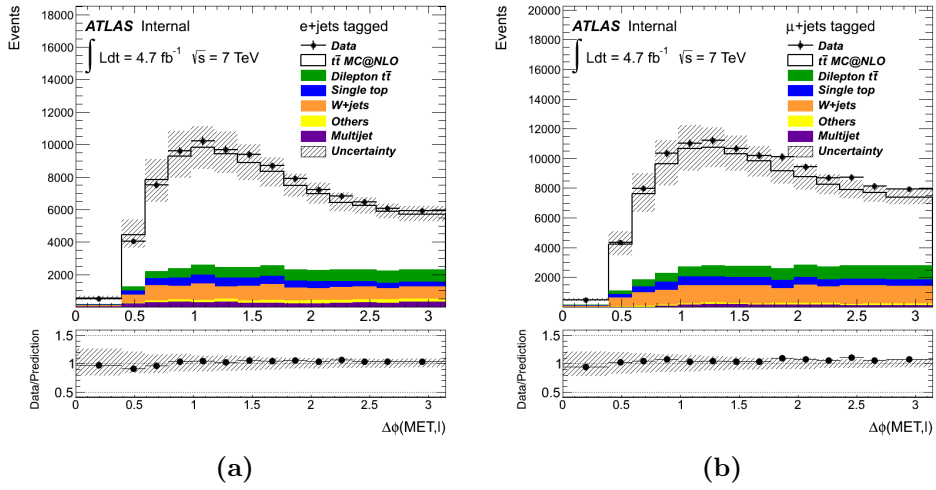


Figure 5.11 –  $\Delta\phi(\cancel{E}_T, \mathbf{p}_T^{lepton})$  spectra for the electron (a) and muon (b) channel after the one-tag selection.

---

---

## CHAPTER 6

---

### DESCRIPTION OF THE MEASUREMENT

Once the events are selected applying the requirements described in Chapter 5, the full  $t\bar{t}$  system can be reconstructed.

#### 6.1 $t\bar{t}$ system reconstruction

The  $t\bar{t}$  system reconstruction is performed through a kinematic fit that assesses the compatibility of the selected event with a typical top pair semi-leptonic decay, using a likelihood approach [76]. This method takes into account all the kinematic variables of the event: measured energies, pseudorapidities and azimuthal angles of the jets, the  $b$ -tag likelihoods for each jet, the energy of the lepton and the missing transverse momentum. The parton energies, the lepton  $p_T$  and the three components of the neutrino momentum are used as fit parameters. Through the likelihood, the measured jets are assigned to the decay products of the  $t\bar{t}$  system, taking into account all permutations with four out of the possible five leading jets. The non-Gaussian partonic energy

## Chapter 6. Description of the measurement

---

resolution of the final state objects, expressing the resolution of the particle jets with respect to the partons, is taken into account using object-specific transfer functions.

The likelihood can be expressed as

$$\begin{aligned}
 \mathcal{L} = & \mathcal{B}(\tilde{E}_{p,1}, \tilde{E}_{p,2} | m_W, \Gamma_W) \cdot \mathcal{B}(\tilde{E}_l, \tilde{E}_\nu | m_W, \Gamma_W) \cdot \\
 & \cdot \mathcal{B}(\tilde{E}_{p,1}, \tilde{E}_{p,2}, \tilde{E}_{p,3} | m_t, \Gamma_t) \cdot \mathcal{B}(\tilde{E}_l, \tilde{E}_\nu, \tilde{E}_{p,4} | m_t, \Gamma_t) \cdot \\
 & \cdot \mathcal{W}(\hat{E}_x^{miss} | \tilde{p}_{x,\nu}) \cdot \mathcal{W}(\hat{E}_y^{miss} | \tilde{p}_{y,\nu}) \cdot \mathcal{W}(\hat{E}_{lep} | \tilde{E}_{lep}) \cdot \\
 & \cdot \prod_{i=1}^4 \mathcal{W}(\hat{E}_{jet,i} | \tilde{E}_{p,i}) \cdot P(b \text{ tag} | \text{quark}), \tag{6.1}
 \end{aligned}$$

where:

- $\tilde{E}_{p,i}$  are the energies of partons associated to reconstructed jets' energy  $\hat{E}_{jet,i}$ ;
- $\mathcal{W}$  are the transfer functions associating the reconstructed quantities, represented by  $\hat{X}$ , to quark and leptons produced at generator level ( $\tilde{X}$ ). These transfer functions are derived from Monte Carlo simulations;
- $\mathcal{B}(\tilde{E}_{X,i} | m_Y, \Gamma_Y) = \frac{1}{[(\sum \tilde{E}_{X,i})^2 - m_Y^2]^2 + m_Y^2 \Gamma_Y^2}$ , where  $m_Y$  and  $\Gamma_Y$  are the mass and the decay width of the particle  $Y$  as in PDG. These are the Breit-Wigner functions, evaluated using invariant masses of sums of appropriate parton and lepton four-vectors at the generator level;
- $P(\text{tagged} - \text{parton flavor})$  are the  $b$ -tagging probability or the jet rejection efficiency, depending on the parton flavor, as obtained from Monte Carlo simulations.

The pole masses of the W boson and the top quark are fixed to  $m_W = 80.4$  GeV and  $m_t = 172.5$  GeV, while the width are  $\Gamma_W = 2.1$  GeV and  $\Gamma_t = 1.5$

GeV. This likelihood must be maximized with respect to the energy of the partons, the energy of the charged lepton, and the component of the neutrino momentum.

The transfer functions are fitted with a double Gaussian function

$$\mathcal{W}(E_{true}, E_{reco}) = \frac{1}{2\pi(p_2 + p_3 p_5)} \left( e^{-\frac{(\Delta E - p_1)^2}{2p_2^2}} + p_3 e^{-\frac{(\Delta E - p_4)^2}{2p_5^2}} \right) \quad (6.2)$$

where the parameters  $p_1, p_2, p_3, p_4$  and  $p_5$  are functions of the true energy of the correspondent particle and  $\Delta E = E_{true} - E_{reco}$ . Two examples of transfer functions are shown in Fig. 6.1.

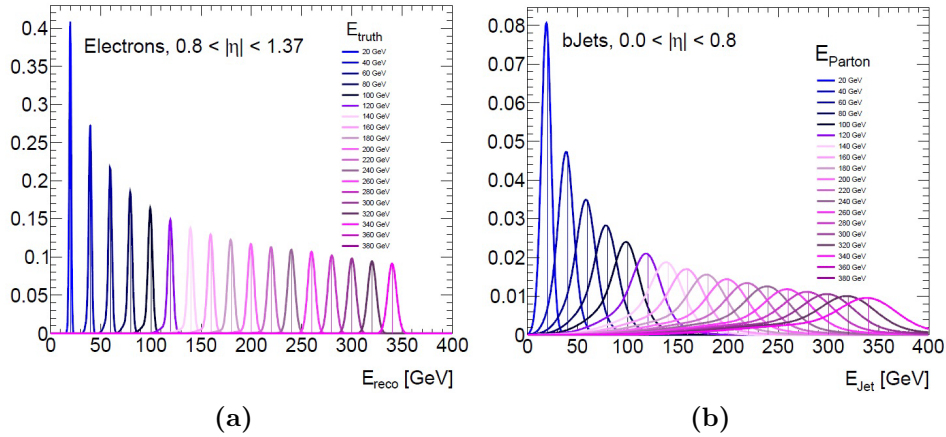


**Figure 6.1** – (a): the transfer functions mapping the measured electrons to the corresponding generated objects in the range  $0.8 < |\eta| < 1.37$ . (b): the transfer functions mapping the measured  $b$  jets to the corresponding partonic objects in the range  $|\eta| < 0.8$ .

Fig. 6.2 show the kinematic likelihood distribution after the one-tag selection. A cut on the fit likelihood can be used to avoid events with a badly reconstructed  $t\bar{t}$  system. A further requirement,  $\log \mathcal{L} > -52$ , has been applied on the selected samples. The performance of this cut will be discussed in the following section.

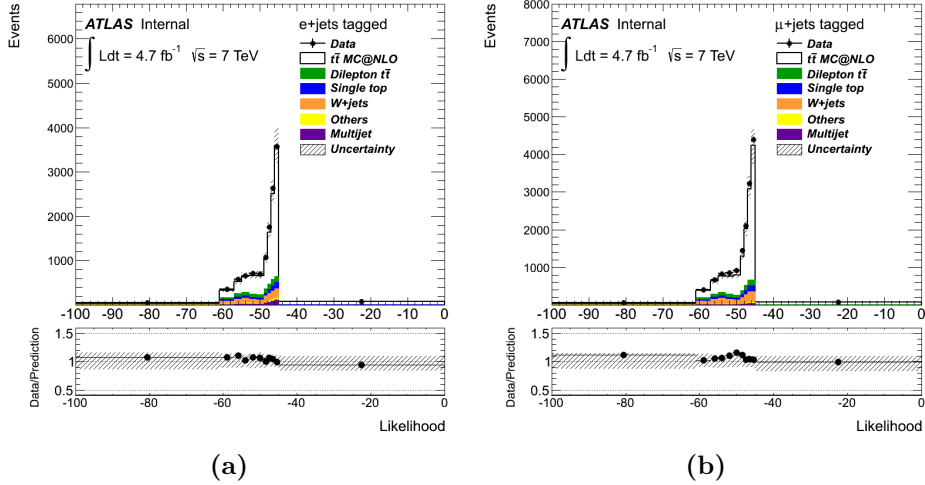


**Figure 6.2** – Kinematic fit likelihood distribution in the tagged sample for the electron channel (a) and muon channel (a).

### 6.1.1 Performance of the fit

The performance of the kinematic fit has been assessed by evaluating the resolution  $RMS(X_{reco} - X_{truth})$  in each  $X_{truth}$  bin, i.e. the “goodness” of the reconstruction of the  $t\bar{t}$  kinematic variable  $X$ . This quantity is strongly related to the kinematic fit likelihood. In Fig. 6.3-Fig. 6.8 it is shown how the overall resolutions improve when the “good likelihood cut” is applied. This improvement, however, is obtained at the cost of a loss in efficiency, especially at high  $t\bar{t}$   $p_T$ , as shown in Fig. 6.9.

### 6.1.2 Binning choice

The resolution studies for the  $t\bar{t}$  kinematic variables are crucial for the binning choice for the final distributions. This choice, infact, should grant a reasonable compromise between:

- the smaller is the bin, the better (it’s a “differential” measurement, after all);

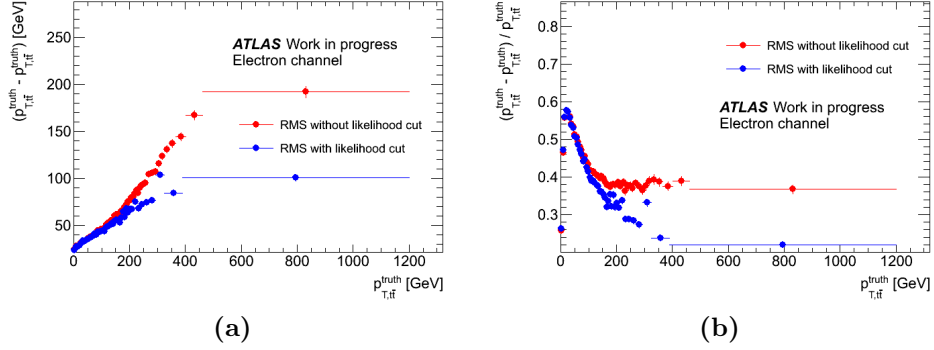


**Figure 6.3** – RMS of the absolute (a) and relative (b)  $p_T$  reconstruction discrepancy  $p_T^{reco} - p_T^{truth}$  in the electron channel.

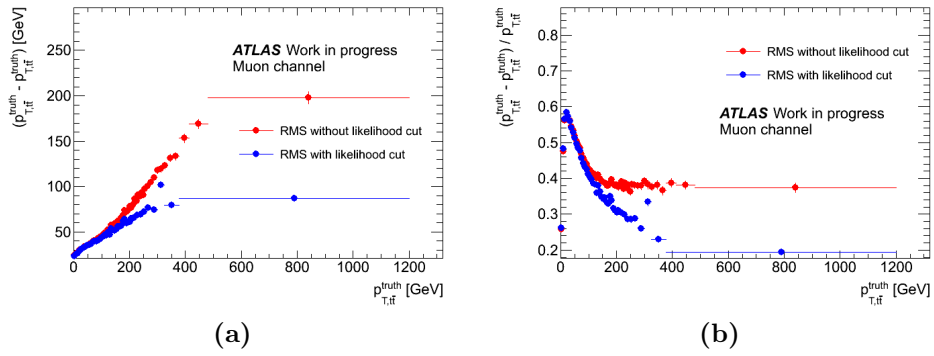


**Figure 6.4** – RMS of the absolute (a) and relative (b)  $t\bar{t}$   $p_T$  reconstruction discrepancy  $p_T^{reco} - p_T^{truth}$  in the muon channel.

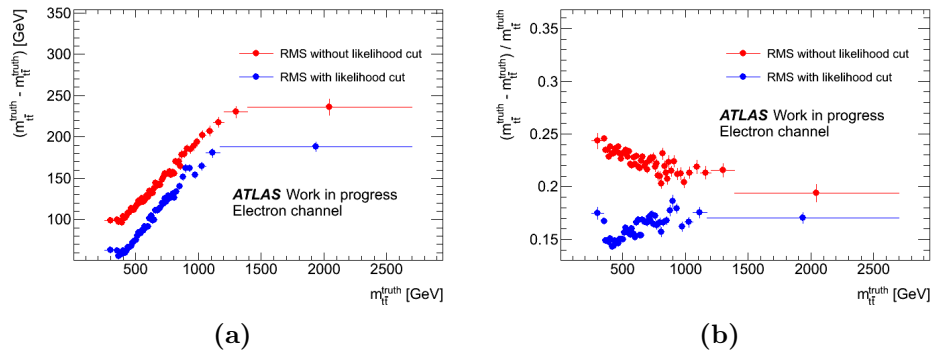


**Figure 6.5** – RMS of the absolute (a) and relative (b)  $t\bar{t}$  mass reconstruction discrepancy  $m^{reco} - m^{truth}$  in the electron channel.

## Chapter 6. Description of the measurement

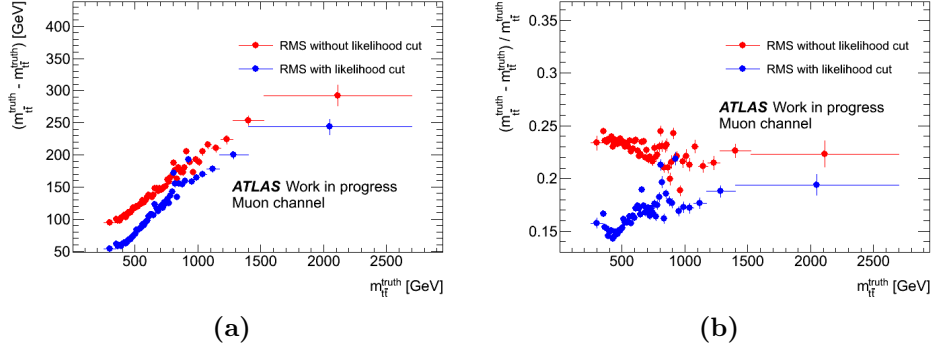


**Figure 6.6** – RMS of the absolute (a) and relative (b)  $t\bar{t}$  mass reconstruction discrepancy  $m^{reco} - m^{truth}$  in the muon channel.

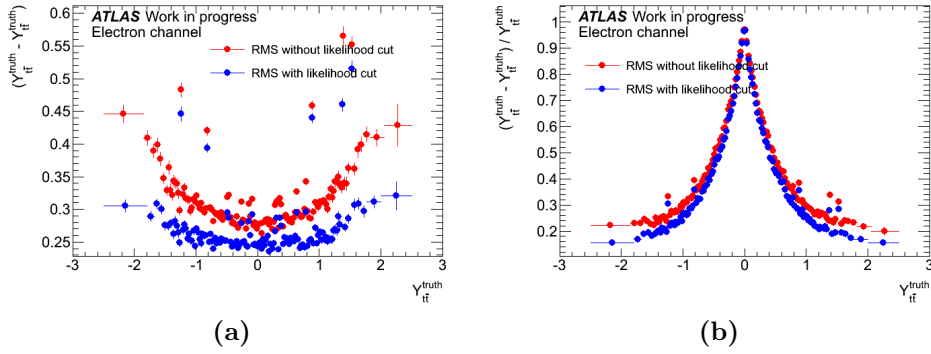


**Figure 6.7** – RMS of the absolute (a) and relative (b)  $t\bar{t}$  rapidity reconstruction discrepancy  $Y^{reco} - Y^{truth}$  in the electron channel.

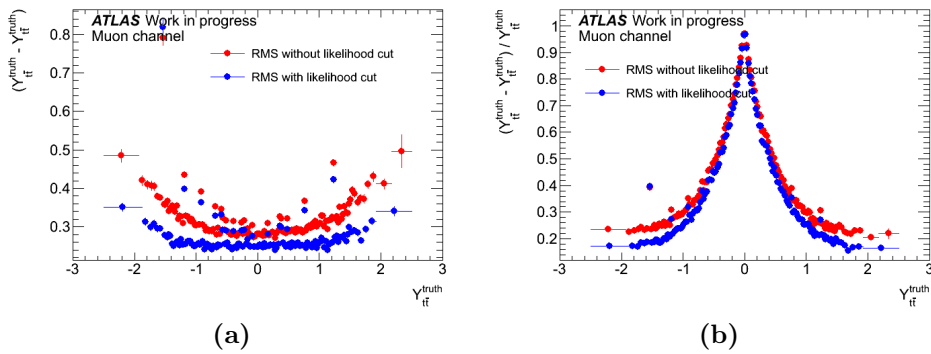


**Figure 6.8** – RMS of the absolute (a) and relative (b)  $t\bar{t}$  rapidity reconstruction discrepancy  $Y^{reco} - Y^{truth}$  in the muon channel.

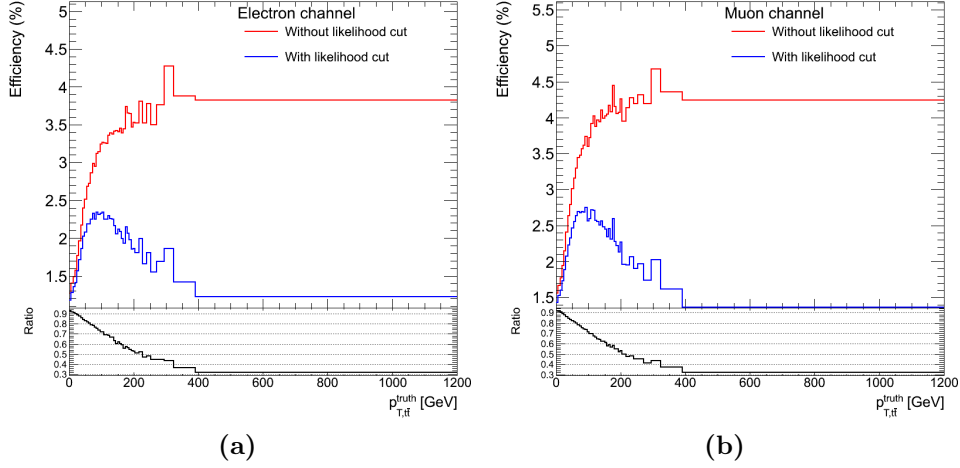


**Figure 6.9** – Efficiency for the  $t\bar{t} p_T$  variable without any likelihood requirement (red) and requiring  $\log \mathcal{L} > -52$  (blue) in the electron channel (a) and in the muon channel (b).

- stability against the migrations due to the reconstruction algorithm (the bin width should not be much lower than the reconstruction resolution);
- good statistics in each bin;
- stability against systematic fluctuations.

The current choice for the width of the bins is the same of the one used in the measurement using the first  $2 \text{ fb}^{-1}$  of data collected in 2011 [77], with an exception for the  $t\bar{t} p_T$ , where one bin has been added. This choice has been made in order to allow a direct comparison between the final results. The bins used for the variables under study are summarized in Tab. 6.1

For the  $t\bar{t} p_T$ , in particular, the number of bins have been increased from three [77] to four thanks to the improved description of the systematic effects and the higher statistics. Looking at Fig. 6.3 it seems reasonable, resolution-wise, to add another bin, by dividing the second bin (40-170 GeV) in two

## Chapter 6. Description of the measurement

Variable	Binning
$p_T(tt)$ [GeV]	0–40, 40–170, 170–340, 340–1200
Mass ( $t\bar{t}$ ) [GeV]	250–450, 450–550, 550–700., 700–960, 960–2700
Rapidity ( $t\bar{t}$ )	-2.5–-1, -1–-0.5, -0.5–0, 0–0.5, 0.5–1, 1–2.5

**Table 6.1** – Binning choice for the  $d\sigma/dX$  ( $X$  being the  $p_T$ , mass, rapidity of the  $t\bar{t}$  system and  $p_T$  of the individual top) measurement.

parts.

### 6.1.3 Reconstructed spectra

In this section the reconstructed spectra of the kinematic variables under study is presented (Fig. 6.10-Fig. 6.12). The binning is the one described in Tab. 6.1. For all the distributions the measurements are in good agreement with our MC predictions, at the level of the 10 % for both the channels, well inside the bands due to the systematic uncertainties.

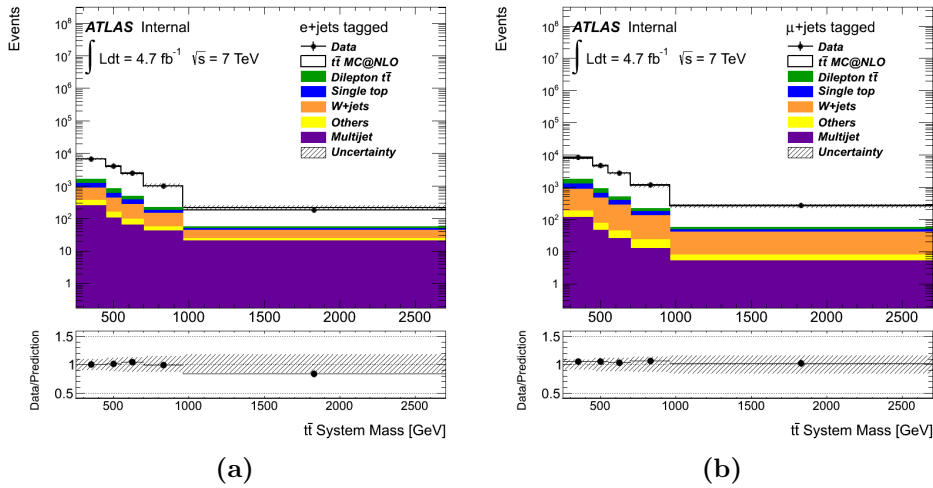


**Figure 6.10** –  $t\bar{t}$  mass spectra in the electron (a) and muon (b) channel after the one-tag selection.

## 6.1. $t\bar{t}$ system reconstruction

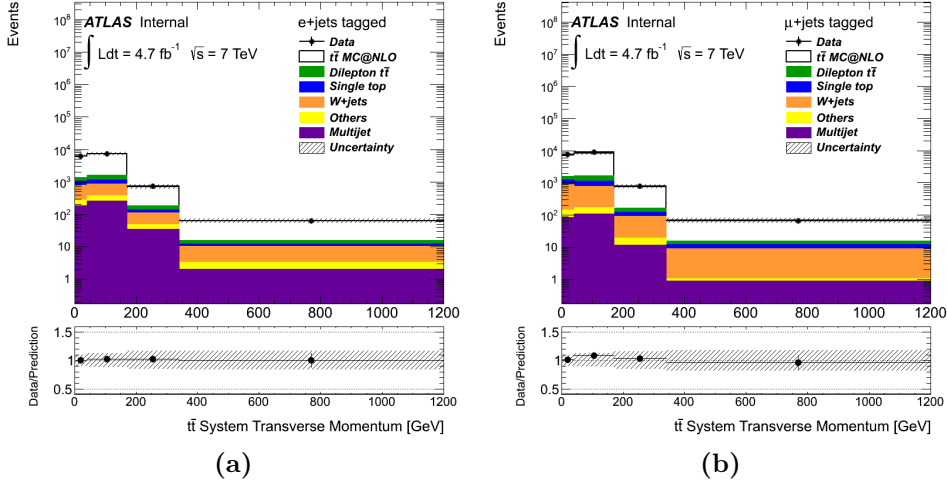


**Figure 6.11** –  $t\bar{t}$   $p_T$  spectra in the electron (a) and muon (b) channel after the one-tag selection.

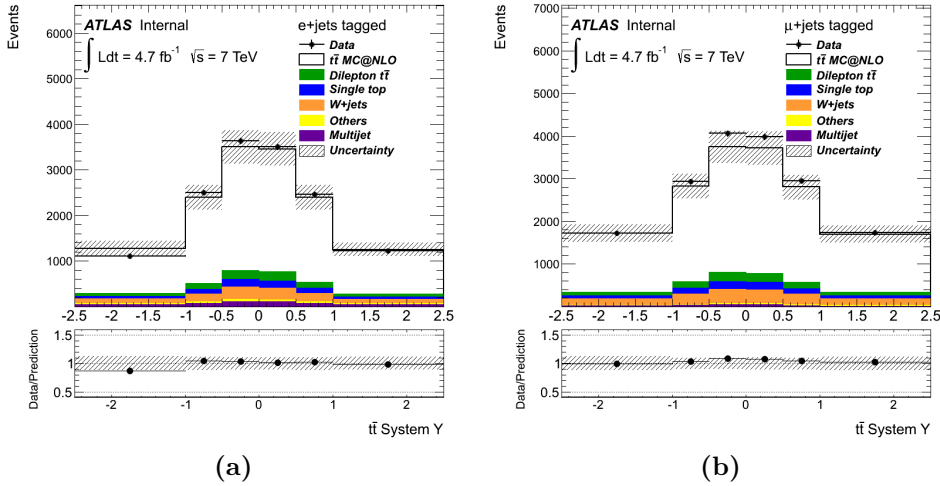


**Figure 6.12** –  $t\bar{t}$  rapidity spectra in the electron (a) and muon (b) channel after the one-tag selection.

## 6.2 Unfolding

One of the main problems in high-energy physics is the distortion of the measurements of the physical observables, due to the resolution and limited geometric acceptance of the detectors. Because of this, the reconstructed distributions of physical quantities can not be directly compared to theoretical predictions and distributions obtained by different experiments. So the data must be corrected for these detector effects before any comparison, with a procedure called “unfolding”. This kind of procedure returns a distribution  $f(x)$  of a certain physical quantity  $x$ , starting from the experimental measurement  $y$  with its distribution  $g(y)$ , different from the true distribution because of effects coming both from the detector and from the analysis methods.

The effects due to the detector has two aspects: a limited acceptance and a limited resolution of the observed physical quantities.

A limited acceptance means that non every event can be used to measure the physical quantity of interest, because of the geometrical acceptance or trigger efficiency or the selection efficiency. All these factors contribute to a total efficiency  $\epsilon$ .

A limited resolution means that it is impossible to measure any physical quantity with an infinite accuracy. The measured value  $y$  will be hence different from the “true” one  $x$ , leading to a smeared distribution  $g(y)$  with respect to the real  $f(x)$ . The real and measured quantities are linked by the folding integral

$$g(y) = \int A(y, x) f(x) dx \quad (6.3)$$

where  $A(y, x)$  is the function which describes all the smearing effects on the

measurement, i.e. the probability to reconstruct a true  $x$  value as  $y$ . An estimation of  $A(y, x)$  can be made through Monte Carlo simulations which allow to evaluate the detector effects on a known distribution  $f(x)$ , and so to determine the relation between  $g(y)$  and  $f(x)$ .

The unfolding procedure tries to infer the true distribution starting from the reconstructed one and is the inverse problem of the folding integral shown in (6.3). The problem solution become easier using discrete variables  $x$  and  $y$ , and representing  $f(x)$  and  $g(y)$  as histograms. In this way, the unfolding equation can be written as

$$\mathbf{g} = R\mathbf{f} \tag{6.4}$$

where  $\mathbf{f}$  is a  $n$ -dimensional vector (the true spectrum),  $g$  is a  $m$ -dimensional vector (the reconstructed spectrum), and  $R$  is a  $m \times n$  matrix called response matrix (containing the information on the acceptance and smearing of the reconstruction process).

The  $R$  matrix is generally not diagonal, because some events generated in bin  $j$  could be reconstructed in bin  $i \neq j$ : this phenomenon is called migration. From the response matrix is possible to build another matrix, called migration matrix, by factorizing out the acceptance of the detector:

$$M_{ij} = \frac{1}{A_j} R_{ij}, \tag{6.5}$$

where  $A_j$  is the efficiency of the reconstruction in the true  $j$ -th bin. The migration matrix expresses the probability that an event generated (and selected) in bin  $j$  is reconstructed in bin  $i$ . The migration matrix is built in such a way that the elements in the columns are normalized to unity, since, once the acceptance is accounted for, the probability to reconstruct an event

## Chapter 6. Description of the measurement

---

in any bin is 1.

In an ideal situation, with infinite resolution and no migrations between the bins, the response matrix is diagonal with the various elements representing the reconstruction efficiency of the  $x$  quantity in the  $j$ -th bin (and the migration matrix becomes the identity). In this ideal case, the “unfolded” spectrum  $\bar{\mathbf{f}}$  can be extracted for the reconstructed spectrum  $\bar{\mathbf{g}}$  simply by dividing each bin in  $\bar{\mathbf{g}}$  by the reconstruction efficiency. This method is called *bin-by-bin* unfolding. In realistic situations, with no-negligible migrations between bins, this approach is not viable. The most used approaches, which will be described in the following sections, are:

- the *simple matrix inversion* method;
- the *iterative Bayesian* method;
- the *single value decomposition* (SVD) method.

### 6.2.1 Simple matrix inversion

In presence of migrations, the  $M$  matrix is not diagonal. The simplest way to solve the unfolding problem is to perform a matrix inversion

$$\mathbf{f} = M^{-1}\mathbf{g}, \tag{6.6}$$

where  $M^{-1}$  is the inverse matrix of  $M$ . The Matrix Inversion method is conceptually the simplest one, but presents some disadvantages, mainly related to the stability of the solutions. Since the unfolding is inherently a statistical problem, small deviations from the input distribution could lead to large differences in the output unfolded results, and the solutions can have oscillations due to the measurement uncertainties.

### 6.2.2 Iterative Bayesian unfolding

The unfolding procedure can be seen as a cause and effect model based on the Bayes theorem [78]. Suppose that, for variable under study, there are  $n$  reconstructed bins and  $m$  truth bins. We can define the effect  $E_j$  as the  $n_j$  events in reconstructed bin  $j$ , while the cause  $C_i$  as the  $n_i$  events in the truth bin  $i$ .

While the effect is measured, it is impossible to unequivocally identify the cause, which has to be estimated. The probability for an effect to come from a particular cause  $P(E_j|C_i)$  can be estimated assuming some knowledge of the migration matrix, and a measurement efficiency and resolution calculated from Monte Carlo.

The unfolding procedure can be done performing a standard Bayesian inference analysis. The probability of a cause given a particular effect (the so-called posterior ) is given by the Bayes theorem

$$P(C_i|E_j) = \frac{P(E_j|C_i) \cdot P_0(C_i)}{\sum_{l=1}^{n_C} P(E_j|C_l) \cdot P_0(C_l)} \quad (6.7)$$

while the number of events in the  $i$ -th cause bin which is expected is

$$\hat{n}(C_i) = \frac{1}{\epsilon_i} \sum_{j=1}^{n_E} P(C_i|E_j) n(E_j), \quad (6.8)$$

where  $n(E_j)$  is number of events in the “effect” bin  $j$ ,  $P_0(C_i)$  is the *a priori* probability (prior) of the cause  $C_i$  and  $\epsilon_i$  is the efficiency of the selection in the bin  $i$ .

The population in the cause bins can be written in terms of the *unfold*

## Chapter 6. Description of the measurement

---

*matrix:*

$$\hat{n}(C_i) = \sum_{j=1}^{n_E} \mathcal{M}_{ij}^{-1} n(E_j). \quad (6.9)$$

In this case, the unfold matrix  $\mathcal{M}_{ij}^{-1}$  is not the algebraic inverse of the migration matrix  $M_{ij}$  but is defined as

$$\mathcal{M}_{ij}^{-1} = \frac{P(E_j|C_i) \cdot P_0(C_i)}{\sum_{l=1}^{n_E} P(E_l|C_i) \sum_{l=1}^{n_C} P(E_j|C_l) \cdot P_0(C_l)}. \quad (6.10)$$

It's then possible to evaluate the *posterior* probability of each cause  $C_i$

$$\hat{P}(C_i) = \frac{\hat{n}(C_i)}{\sum_j \hat{n}(C_j)}, \quad (6.11)$$

In order to stabilize the solution, the Bayesian method can be used iteratively, making a polynomial fit of the posterior solution and using it as the prior for the next iteration. Each iteration will give a better estimation of the actual distribution, until the algorithm reaches a certain stability in which each new result does not differ significantly from the previous one.

### 6.2.3 Single Value Decomposition

The Single Value Decomposition [79] is an extension to the simple matrix inversion, where direct solutions can lead to rapidly oscillating solution. This procedure is done making a single value decomposition of the migration matrix  $M$  and regularizing the solutions with a normalization term. The matrix  $M$  can be written as

$$M = USV^T \quad (6.12)$$

where  $U$  is an  $m \times m$  orthogonal matrix,  $V$  is an  $n \times n$  orthogonal matrix and  $S$  is an  $m \times n$  diagonal matrix with no negative diagonal elements, defined as

$$S_{ij} = 0 \text{ if } i \neq j, S_{ii} = s_i, s_i > 0. \quad (6.13)$$

The inverted migration matrix is, then

$$M_{ij}^{-1} = VS^{-1}U^T \quad (6.14)$$

This method greatly simplifies the inversion process but, on the other hand, finding the right decomposition matrices is in general a difficult task. The elements of the columns of this matrix are normalized to unity and, in order to reduce the oscillations of the obtained distribution, a regularization condition is extracted from the previous knowledge on the system, which can be expressed with a matrix. The weight of the regularization conditions on the final distribution depends on the regularization parameter  $k$ , which has to be set depending on the boundary conditions and typically has a value of  $k \equiv n/2$ , where  $n$  is the number of bins of the histogram.

#### 6.2.4 Migration matrices and efficiencies

As seen in the previous sections, all unfolding methods require three main ingredients:

- the reconstructed spectra (shown in Fig. 6.10-Fig. 6.12);
- the migration matrices;
- the selection efficiencies.

## Chapter 6. Description of the measurement

The migration matrices, for the three variables  $p_{T,t\bar{t}}$ ,  $m_{t\bar{t}}$ ,  $Y_{t\bar{t}}$  are shown in Fig. 6.13-Fig. 6.15. It's again evident that the likelihood cut improves the overall precision of the measurement (in this case, by increasing the “diagonality” of the matrices, especially for the  $p_T$  of the system, Fig. 6.14).

Fig. 6.16-Fig. 6.18 show the one-tag selection efficiency for the  $t\bar{t}$  mass,  $p_T$  and rapidity respectively, using both Mc@NLO and Alpgen as Monte Carlo generators. Alpgen shows an overall higher efficiency respect to Mc@NLO, such effect is due to the increased population in the high number of jets phase space region.

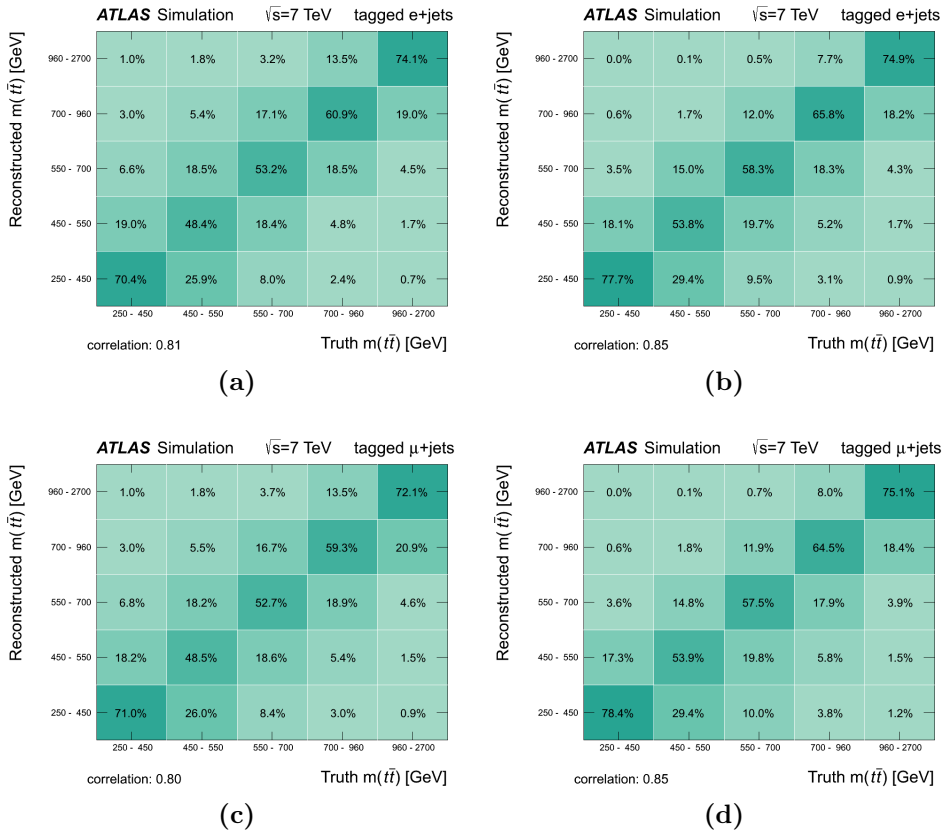


**Figure 6.13** – Migration matrices for  $m_{t\bar{t}}$  without likelihood cut (right) and with likelihood cut (left) for the electron (top) and muon (bottom) after the one-tag selection.

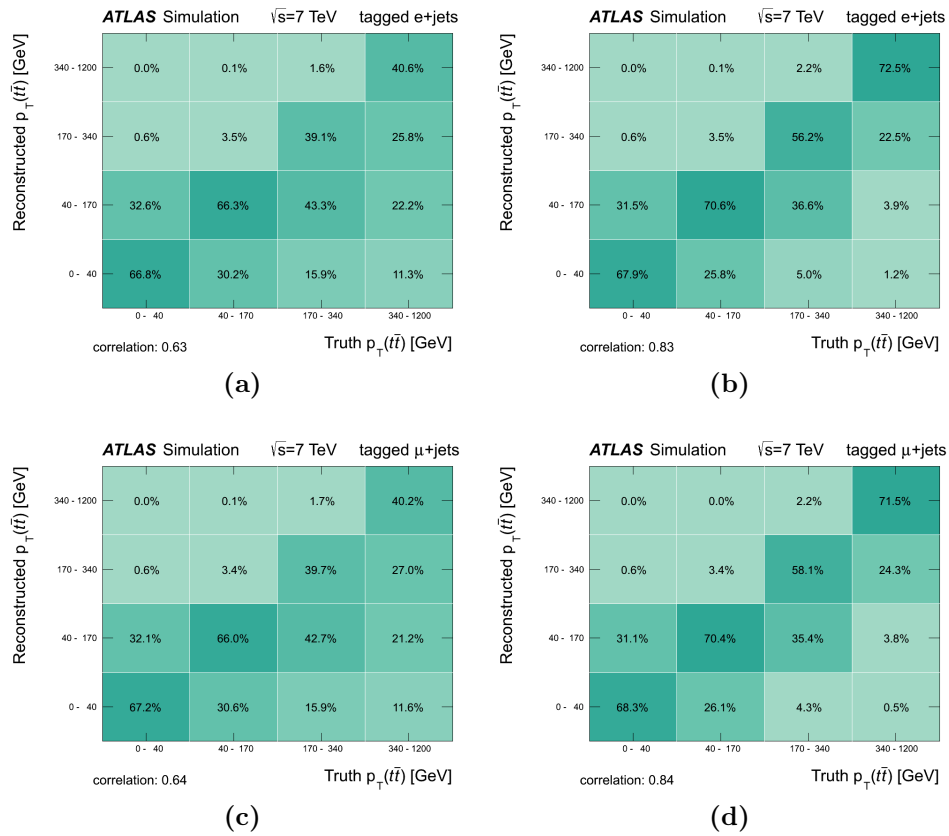


**Figure 6.14** – Migration matrices for  $p_{T,t\bar{t}}$  without likelihood cut (right) and with likelihood cut (left) for the electron (top) and muon (bottom) after the one-tag selection.

## Chapter 6. Description of the measurement

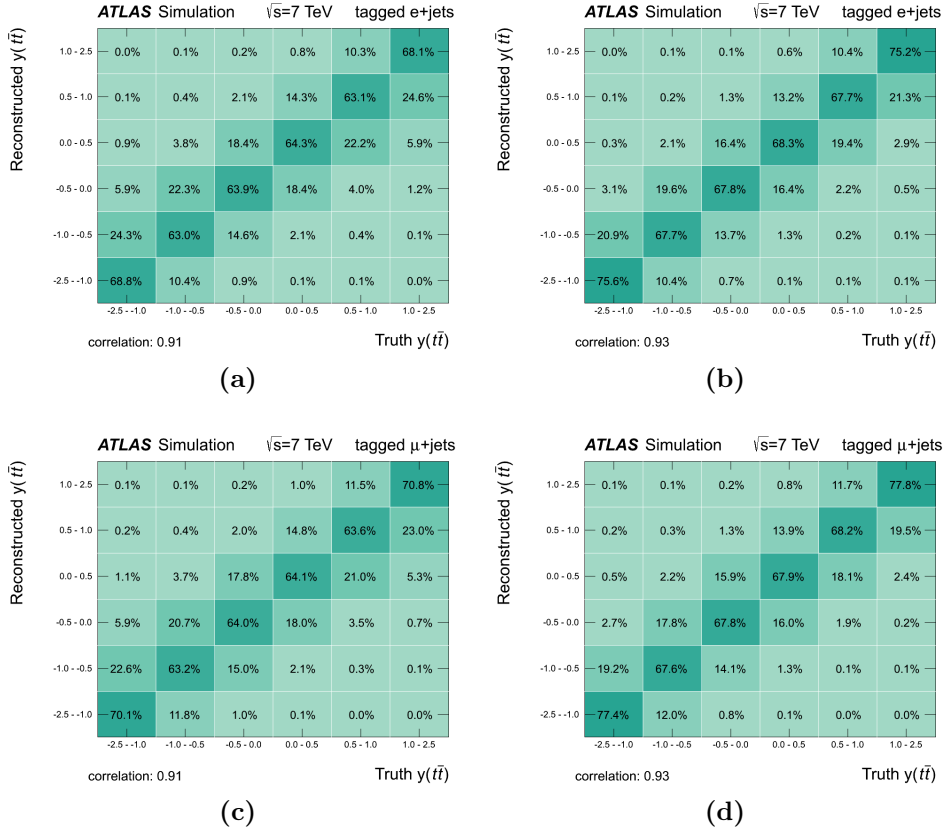


**Figure 6.15** – Migration matrices for  $Y_{t\bar{t}}$  without likelihood cut (right) and with likelihood cut (left) for the electron (top) and muon (bottom) after the one-tag selection.

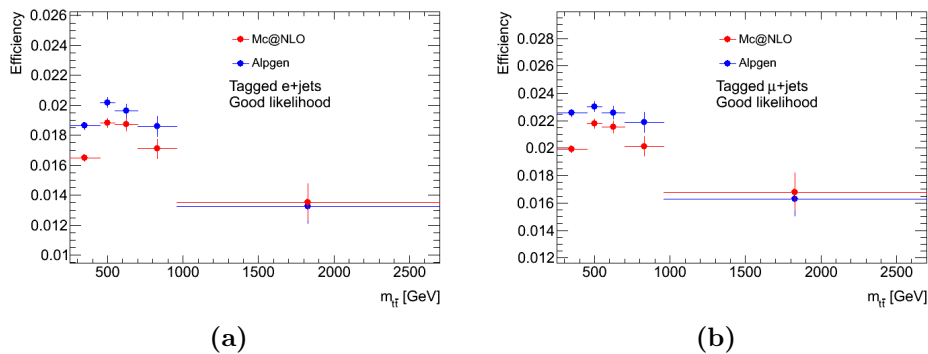


**Figure 6.16** – Efficiency for the  $t\bar{t}$  mass for the electron (a) and muon (b) channel, in the one-tag selection.

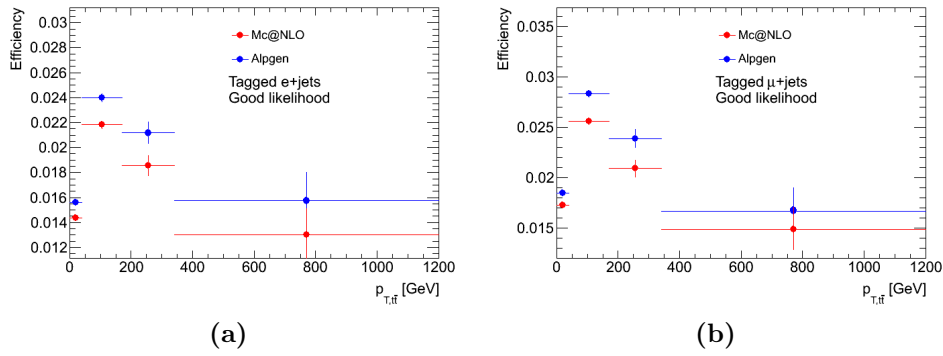


**Figure 6.17** – Efficiency for the  $t\bar{t}$   $p_T$  for the electron (a) and muon (b) channel, in the one-tag selection.

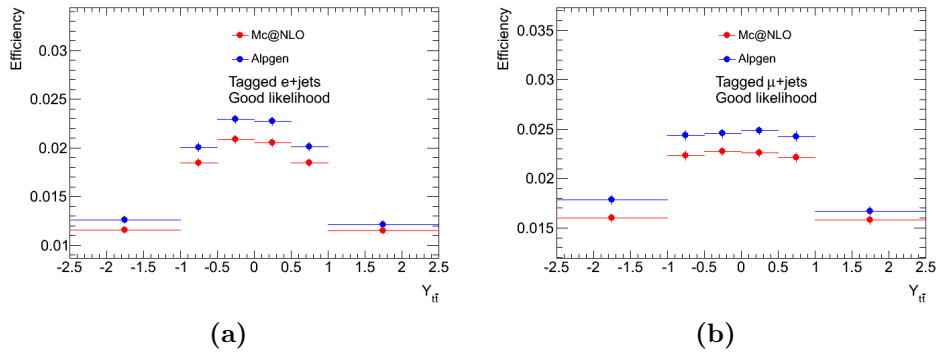


**Figure 6.18** – Efficiency for the  $t\bar{t}$  rapidity for the electron (a) and muon (b) channel, in the one-tag selection.

### 6.2.5 Propagation of the uncertainties through the unfolding

The effect of systematics on the unfolded spectrum have been evaluated by applying the systematic variation to the prediction (i.e. background, signal efficiency and migration matrix) and then unfolding the data using these ingredients instead of the central ones. The uncertainty on the measurement is then calculated as the difference between the actual unfolded result and the unfolded nominal one (with no systematic variation). The total systematic uncertainty in each bin is calculated adding all deviations in quadrature, depending on its sign (positive deviations contribute to the “up” uncertainty while negative to the “down” uncertainty). Only for the I/FSR systematic a different approach is used, since the corresponding samples have been generated with a LO generator, and thus not compatible with our NLO reference. In this case, the relative difference between the I/FSR up and I/FSR down (see Sect. 5.2.1) is considered, and the systematic is extracted by scaling up and down the central measurement.

In Appendix B there is a summary of the effects of the systematic uncertainties which have been considered in the analysis.

### 6.2.6 Combination of the channels

Once the measurement has been extracted for each channel, electron and muon, it’s possible to improve the final results by *combining* the two channels. In this thesis a basic approach is used: the results after the selection cuts, for both channels, have been summed up, and then unfolded as a unique sample.

Special care has to be taken when handling the systematics: the systematic variations have been applied simultaneously for both channels in the

case of “correlated” source of uncertainties (i.e. uncertainties, like the jet energy scale, that affect the two channels in the same way); in the case of “uncorrelated” systematics (i.e. variations whose sources and/or estimation procedures are different for the two channels, such as the QCD) the variations are applied to one channel keeping the other fixed.

In [77] the unfolded cross-sections from the two channels are combined using a weighted mean which includes the full covariance matrix between the channels. In this case, since the covariance matrix is used in the weighting, the estimate is a best linear unbiased estimator of the cross section. This second approach is currently under development for this analysis, and its results are not included in this thesis.

## 6.3 Results

Unfolding procedures start from reconstructed distributions ( $N_i$ ) where the backgrounds ( $B_i$ ) have been subtracted. The bins of the generated events are linked to the bins of the reconstructed events through the migration matrix  $M_{ij}$ , derived from the  $t\bar{t}$  signal simulations

$$N_i = \sum_j M_{ij} \epsilon_j \sigma_j \beta_{SL} \mathcal{L} + B_i \quad (6.15)$$

where  $\mathcal{L}$  is the integrated luminosity,  $\epsilon_j$  is the acceptance, and  $\beta_{SL}$  is the branching fraction of the decay channel under study, in our case the “Single Lepton” (electron or muon) channel. The cross section can be extracted solving by “inverting” (6.15)

$$\sigma_j = \frac{\sum_i M_{ij}^{-1} (N_i - B_i)}{\epsilon_j \beta_{SL} \mathcal{L}} \quad (6.16)$$

## Chapter 6. Description of the measurement

---

where  $M^{-1}$  is estimated through the unfolding procedures described in the previous sections. SVD has been chosen as main unfolding method, since it grants a better stability against statistical fluctuations, especially in the low population bins. The simple matrix inversion method has been used as a cross check.

The calculation of three differential cross sections has been performed with respect to the mass, transverse momentum and rapidity of the  $t\bar{t}$  system, using the binning presented in Tab. 6.1.

In order to improve the precision of the measurements, the relative differential cross section is evaluated, because many of the systematic uncertainties have a minimal effect on the shape of the distribution and cancel in the ratio  $\frac{1}{\sigma} \frac{d\sigma}{dX}$ .

The unfolded distributions obtained by the measured data are compared with the prediction from MC@NLO, MCFM [80] and Alpgen. The first two generators perform the full NLO matrix element calculation (MC@NLO including also the Parton Shower) of the  $pp \rightarrow t\bar{t}$  process, while Alpgen generates events at the leading order for the  $pp \rightarrow t\bar{t} + N$  jets.

### 6.3.1 $\frac{1}{\sigma} \frac{d\sigma}{dM}$

The resulting spectra of the unfolded normalized differential cross section as a function of the mass of the  $t\bar{t}$  system are shown in Fig. 6.19 and Tab. 6.2 using the SVD method and Fig. 6.20 and Tab. 6.3 using the simple matrix inversion method. The spectra for the combined sample are shown in Fig. 6.21 for the SVD unfolding and Fig. 6.22 for the matrix inversion unfolding.

The unfolded distribution, represented by the black dots, is in good agreement with the theoretical predictions: for every bin of the histogram describing the distribution, the ratio between the population from the unfolding of

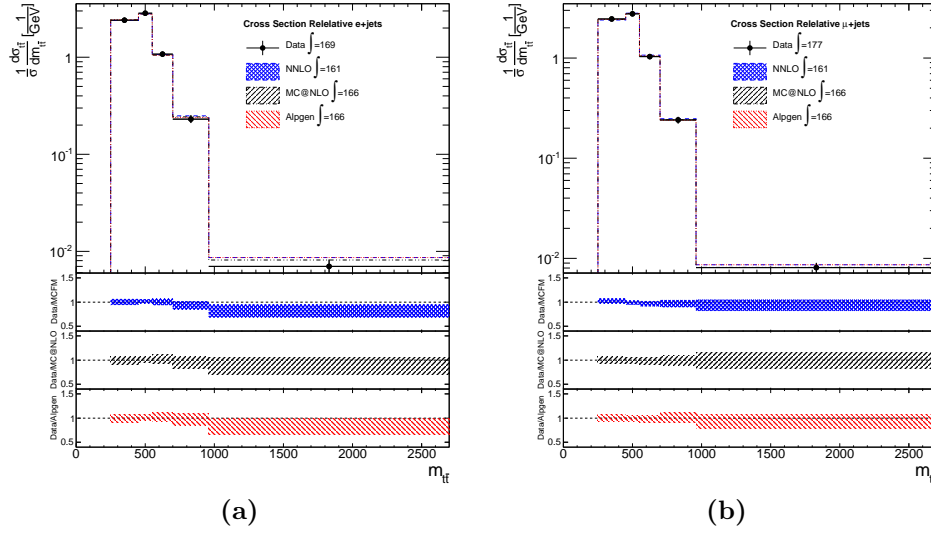


**Figure 6.19** –  $\frac{1}{\sigma} \frac{d\sigma}{dM}$  spectra in the electron (a) and muon (b), unfolded using the SVD method with regularization parameter  $k = 3$ .

$m_{t\bar{t}}$ [GeV]	$1/\sigma d\sigma_{t\bar{t}}/dm_{t\bar{t}}$ [1/TeV]		
	e+jets	$\mu$ +jets	l+jets
250 – 450	2.4 +0.14/-0.15	2.46 +0.13/-0.12	2.44±0.13
450 – 550	2.84 +0.13/-0.12	2.77 +0.11/-0.12	2.8±0.11
550 – 700	1.08±0.07	1.03 +0.05/-0.06	1.05±0.06
700 – 960	0.23±0.02	0.241±0.018	0.236 +0.017/-0.018
960 – 2700	0.007 +0.001/-0.0012	0.0081 +0.001/-0.0009	0.0076±0.0009

**Table 6.2** – Normalized differential  $t\bar{t}$  production cross section as a function of the mass of the system, unfolded using the SVD method with regularization parameter  $k = 3$ .

$m_{t\bar{t}}$ [GeV]	$1/\sigma d\sigma_{t\bar{t}}/dm_{t\bar{t}}$ [1/TeV]		
	e+jets	$\mu$ +jets	l+jets
250 – 450	2.4 +0.16/-0.18	2.46 +0.16/-0.15	2.44±0.15
450 – 550	2.8 +0.2/-0.19	2.79 +0.19/-0.2	2.79±0.17
550 – 700	1.14 +0.1/-0.09	0.99±0.07	1.06 +0.07/-0.06
700 – 960	0.23±0.03	0.26±0.03	0.24±0.02
960 – 2700	0.005 +0.0018/-0.002	0.0075±0.0019	0.0064 +0.0015/-0.0016

**Table 6.3** – Normalized differential  $t\bar{t}$  production cross section as a function of the mass of the system, unfolded using the simple matrix inversion method.

## Chapter 6. Description of the measurement

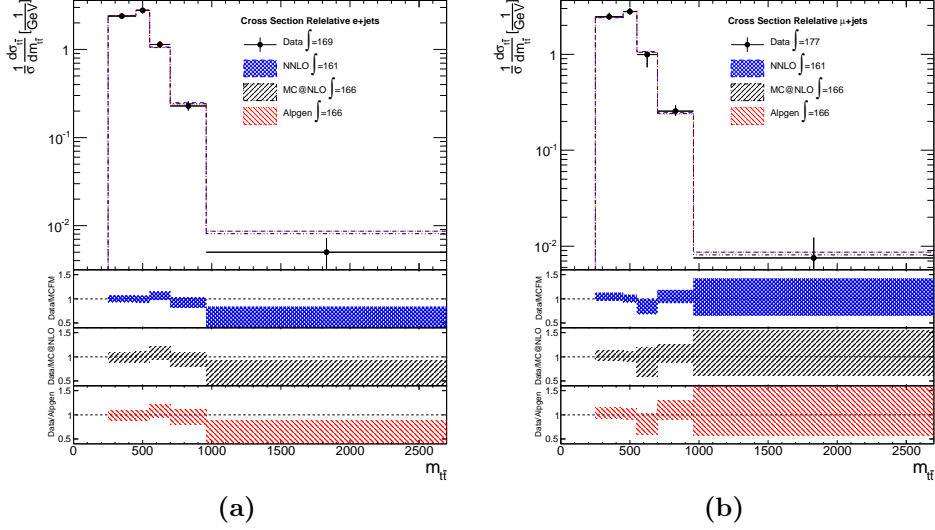


**Figure 6.20** –  $\frac{1}{\sigma} \frac{d\sigma}{dM}$  spectra in the electron (a) and muon (b), unfolded using the inversion method.

real data and the Monte Carlo simulations (shown in the bottom part of the plots) is within the theoretical uncertainties obtained using MCFM (the blue band is obtained by varying the scale  $\mu = 2m_{t\text{top}}$  in the range  $[\mu/2, 2\mu]$ ), MC@NLO and AlpGen (in these two cases the error band is obtained by propagating the systematic uncertainties to the unfolded result, as described in Sect. 6.2.5).

### 6.3.2 $\frac{1}{\sigma} \frac{d\sigma}{dp_T}$

The resulting spectra of the unfolded normalized differential cross section as a function of the transverse momentum of the  $t\bar{t}$  system is shown in Fig. 6.23 and Tab. 6.4 using the SVD method and Fig. 6.24 and Tab. 6.5 using the simple matrix inversion method. The spectra for the combined sample are shown in Fig. 6.25 for the SVD unfolding and Fig. 6.26 for the matrix inversion unfolding.

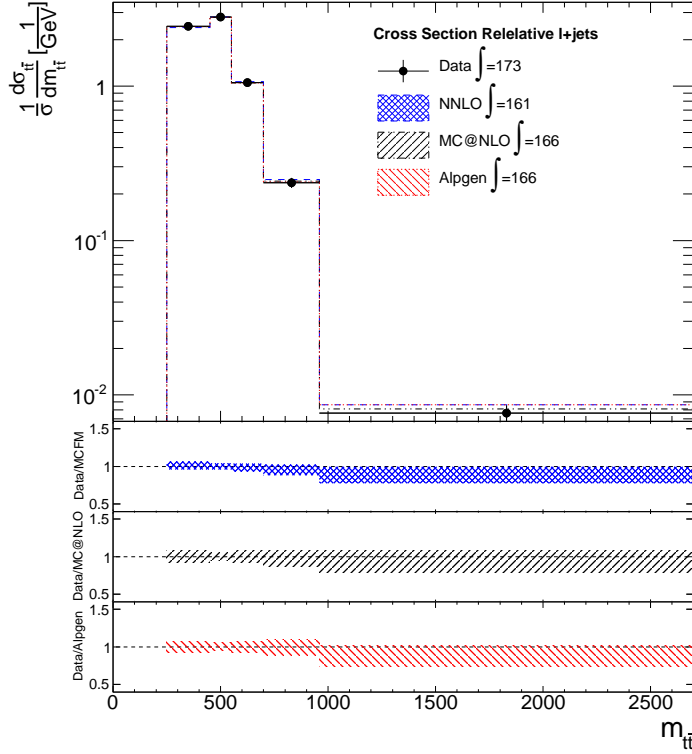


**Figure 6.21** – Normalized differential  $t\bar{t}$  production cross section as a function of the mass of the system for the combined sample, unfolded using the SVD method.

$p_{T,t\bar{t}}$ [GeV]	$1/\sigma d\sigma_{t\bar{t}}/dp_{T,t\bar{t}}$ [1/TeV]		
	e+jets	$\mu$ +jets	l+jets
0 – 40	$13.6 \pm 1.6$	$13.1 +1.7/-1.6$	$13.3 \pm 1.6$
40 – 170	$3.1 \pm 0.3$	$3.2 \pm 0.3$	$3.1 \pm 0.3$
170 – 340	$0.27 +0.05/-0.06$	$0.27 \pm 0.05$	$0.27 \pm 0.05$
340 – 1200	$0.0062 \pm 0.0016$	$0.0058 \pm 0.0015$	$0.0059 \pm 0.0015$

**Table 6.4** – Normalized differential  $t\bar{t}$  production cross section as a function of the Pt of the system, unfolded using the SVD method with regularization parameter  $k = 3$ .

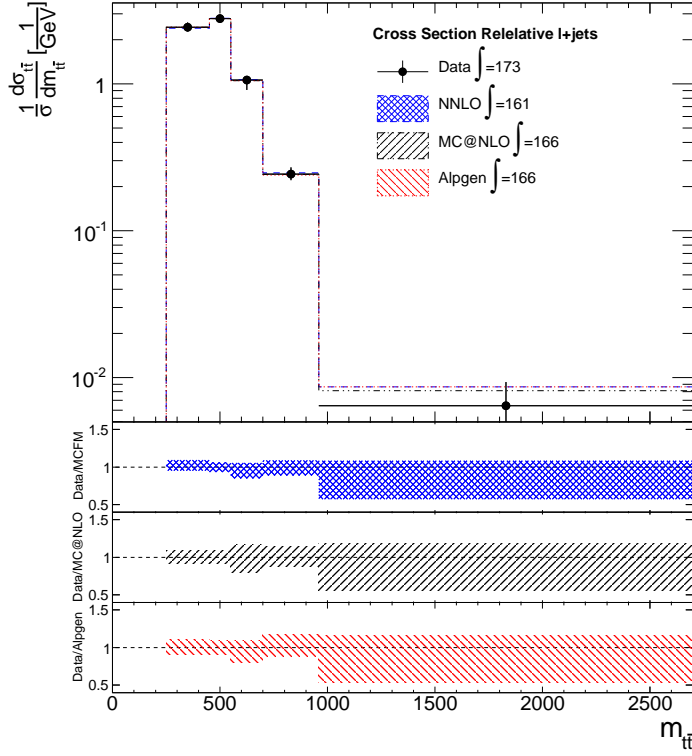


**Figure 6.22** – Normalized differential  $t\bar{t}$  production cross section as a function of the mass of the system for the combined sample, unfolded using the matrix inversion method.

$p_{T,t\bar{t}}$ [GeV]	$1/\sigma d\sigma_{t\bar{t}}/dp_{T,t\bar{t}}$ [1/TeV]		
	e+jets	$\mu$ +jets	l+jets
0 – 40	$13.5 \pm 2$	$13 + 2/-1.9$	$13 + 2/-1.9$
40 – 170	$3.1 \pm 0.3$	$3.3 + 0.3/-0.4$	$3.2 + 0.3/-0.4$
170 – 340	$0.27 + 0.07/-0.08$	$0.24 \pm 0.07$	$0.26 \pm 0.07$
340 – 1200	$0.006 \pm 0.0018$	$0.0053 \pm 0.0018$	$0.0056 \pm 0.0013$

**Table 6.5** – Normalized differential  $t\bar{t}$  production cross section as a function of the  $P_t$  of the system, unfolded using the simple matrix inversion method.

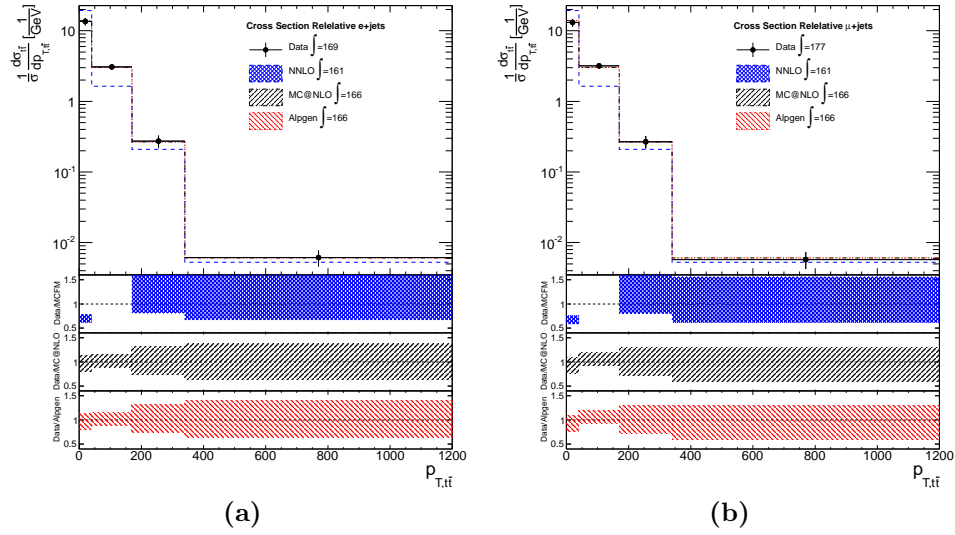


**Figure 6.23** –  $\frac{1}{\sigma} \frac{d\sigma}{dp_T}$  spectra in the electron (a) and muon (b), unfolded using the SVD method with regularization parameter  $k = 3$ .

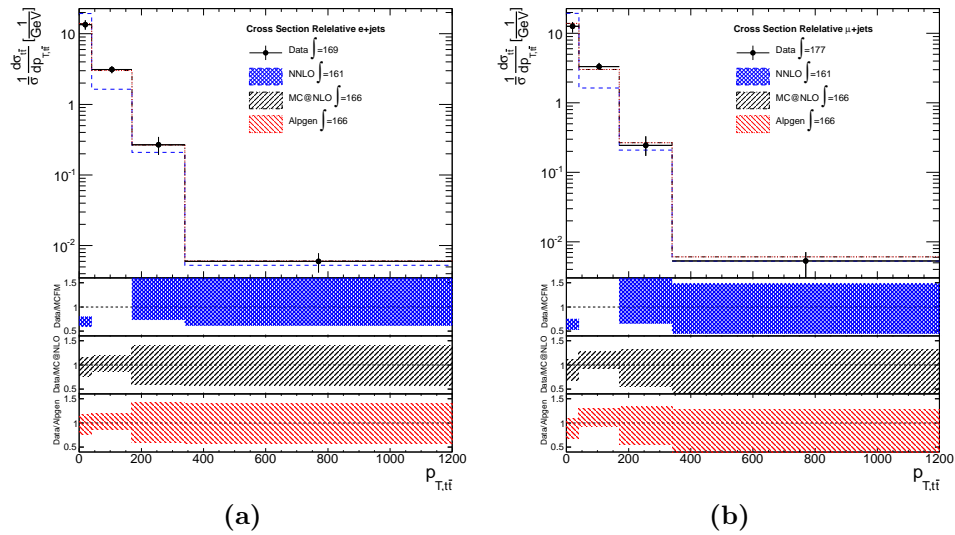


**Figure 6.24** –  $\frac{1}{\sigma} \frac{d\sigma}{dp_T}$  spectra in the electron (a) and muon (b), unfolded using the matrix inversion method.

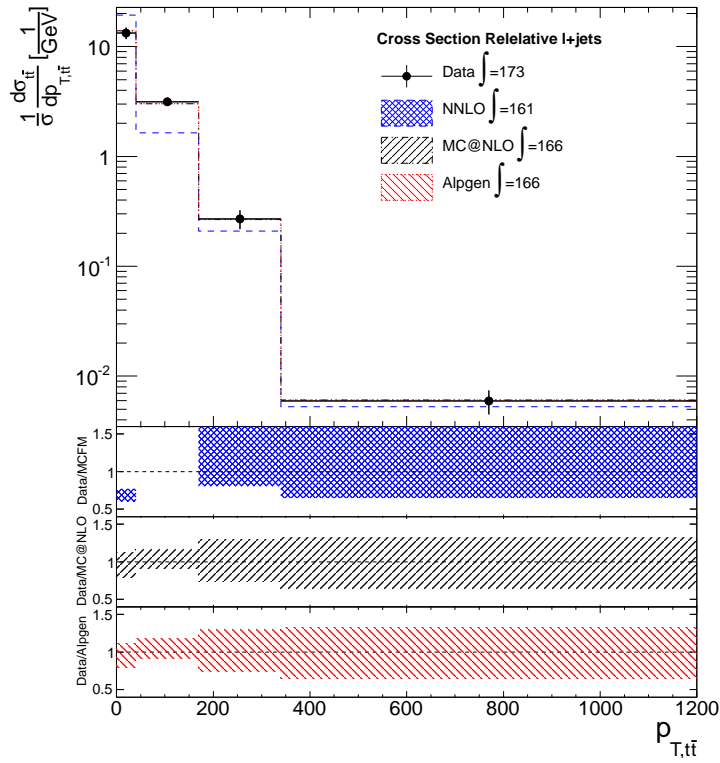


**Figure 6.25** – Normalized differential  $t\bar{t}$  production cross section as a function of the  $P_t$  of the system for the combined sample, unfolded using the SVD method.

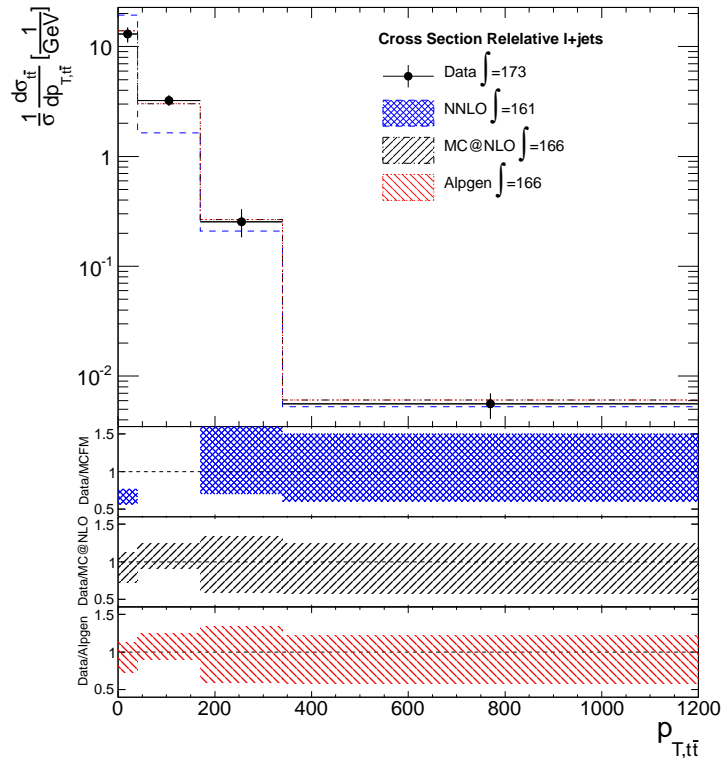


**Figure 6.26** – Normalized differential  $t\bar{t}$  production cross section as a function of the  $P_t$  of the system for the combined sample, unfolded using the matrix inversion method.

## Chapter 6. Description of the measurement

---

The unfolded distribution, represented by the black dots, is in good agreement with the theoretical description made by MC@NLO and Alpgen. On the contrary, the theoretical prediction from MCFM doesn't correctly describe the behavior in the first two bins within the provided uncertainties because, as already seen in Fig. 3.6, that region of the  $t\bar{t}$   $p_T$  spectra is strongly sensitive to the additional radiation due to the non-perturbative parton shower, that is not included in the calculation provided by MCFM.

### 6.3.3 $\frac{1}{\sigma} \frac{d\sigma}{dY}$

The resulting spectra of the unfolded normalized differential cross section as a function of the rapidity of the  $t\bar{t}$  system is shown in Tab. 6.6 using the SVD method and Tab. 6.7 using the simple matrix inversion method.

$y_{t\bar{t}}$	$1/\sigma d\sigma_{t\bar{t}}/dy_{t\bar{t}} [1/\text{TeV}]$		
	e+jets	$\mu$ +jets	l+jets
-2.5 – -1	0.078 +0.006/-0.007	0.085±0.005	0.083 +0.004/-0.005
-1 – -0.5	0.317±0.015	0.312±0.014	0.315±0.013
-0.5 – 0	0.43±0.02	0.423 +0.019/-0.018	0.424±0.017
0 – 0.5	0.416±0.02	0.421±0.018	0.418±0.017
0.5 – 1	0.318±0.015	0.316±0.014	0.317±0.013
1 – 2.5	0.088±0.006	0.088±0.005	0.088±0.005

**Table 6.6** – Normalized differential  $t\bar{t}$  production cross section as a function of the Rapidity of the system, unfolded using the SVD method with regularization parameter  $k = 3$ .

$y_{t\bar{t}}$ [GeV]	$1/\sigma d\sigma_{t\bar{t}}/dy_{t\bar{t}}$ [1/TeV]		
	e+jets	$\mu$ +jets	l+jets
-2.5 – -1	0.068 +0.007/-0.009	0.084 +0.005/-0.006	0.078 +0.005/-0.006
-1 – -0.5	0.35±0.02	0.308 +0.018/-0.017	0.326±0.015
-0.5 – 0	0.42 +0.03/-0.02	0.43±0.02	0.43±0.02
0 – 0.5	0.4±0.02	0.42±0.02	0.41±0.019
0.5 – 1	0.33±0.02	0.316±0.018	0.323±0.015
1 – 2.5	0.086 +0.006/-0.007	0.087±0.006	0.087±0.005

**Table 6.7** – Normalized differential  $t\bar{t}$  production cross section as a function of the Rapidity of the system, unfolded using the simple matrix inversion method.



---

## CONCLUSIONS

The aim of this analysis was to extract the measurement of the top pair production differential cross section, with respect to the mass, the transverse momentum and the rapidity of the  $t\bar{t}$  system.

The analysis has been performed in the single lepton decay channel on the data from proton-proton collisions made at LHC at  $\sqrt{s} = 7$  TeV and collected by the ATLAS detector during the 2011, corresponding to an integrated luminosity of  $\int \mathcal{L} = 4.7 \text{ fb}^{-1}$ .

The data have been compared with the prediction obtained through Monte Carlo generated events (in particular the  $t\bar{t}$  signal and the single top,  $Z$ +jets and diboson backgrounds) and data driven methods (the  $W$ +jets and QCD backgrounds).

In order to improve the signal-over-background ratios, a cut based analysis has been performed. The events have been selected to have one isolated lepton with high transverse momentum, missing transverse energy due to the presence of the neutrino, constraints on the transverse mass of the reconstructed leptonic  $W$  in order to reject the QCD multijet background, and at least four high energy jets, of which at least one compatible with the presence

## Conclusions

---

of a bottom quark.

Once the events have been selected with such criteria, the  $t\bar{t}$  system is reconstructed using a kinematic fit, based on a maximum likelihood approach, that assesses the compatibility of the selected event with a typical top pair semi-leptonic decay. The likelihood from the fit is used to further select the events, in order to reduce the events with a badly reconstructed  $t\bar{t}$  system.

Since the differential distributions of the reconstructed variables are affected by the resolution of the measurements, the acceptance of the detector and the efficiency of the selection, unfolding techniques have been used in order to remove such effects and to extend the measurement to the full phase space, so that the measurements can be directly compared with the theoretical predictions and results from other experiments. Two unfolding methods are compared, the single value decomposition (SVD) and the simple matrix inversion as a cross-check.

A detailed analysis of the sources of systematic uncertainties has been performed with the Jet Energy Scale being the dominant one (especially in the one-tag selection).

The unfolded normalized differential cross sections have been compared with the prediction obtained using MC@NLO, Alpgen and MCFM. All results are compatible with the predictions within the systematic uncertainties, with an exception for the differential cross section versus the  $p_T$  of the system in the low- $p_T$  range, which shows a significant incompatibility with the prediction provided by MCFM. This effect was expected, since the  $p_T$  of the system is strongly dependent on the description of the parton shower, that is not included in the calculation provided by MCFM.

A possible extension of this analysis would be the study of the so-called “boosted topology” of the top decay. Actually, when the top is highly

boosted, the jets produced by its decay tend to join in one large jet and the “resolved” approach used in this analysis becomes largely inefficient. Exploiting this boosted topology will allow hence to gain efficiency in the very interesting region of high  $t\bar{t}$  mass and  $p_T$ . Such study is going to be performed using the much larger data set collected in 2012 at  $\sqrt{s} = 8\text{ TeV}$  ( $\int \mathcal{L} \approx 24\text{ fb}^{-1}$ ).

In summary, the presented study, allowing detailed comparisons between data and MC predictions for several basic variables of the  $t\bar{t}$  system, gives important contributions to improve our knowledge of one of the crucial sectors of the Standard Model.



---

---

# APPENDIX A

---

## CONTROL PLOTS WITH THE ALPGEN GENERATOR

### A.1 Jet-related plots

The number of jets spectra have already been showed in Sect. 3.3.

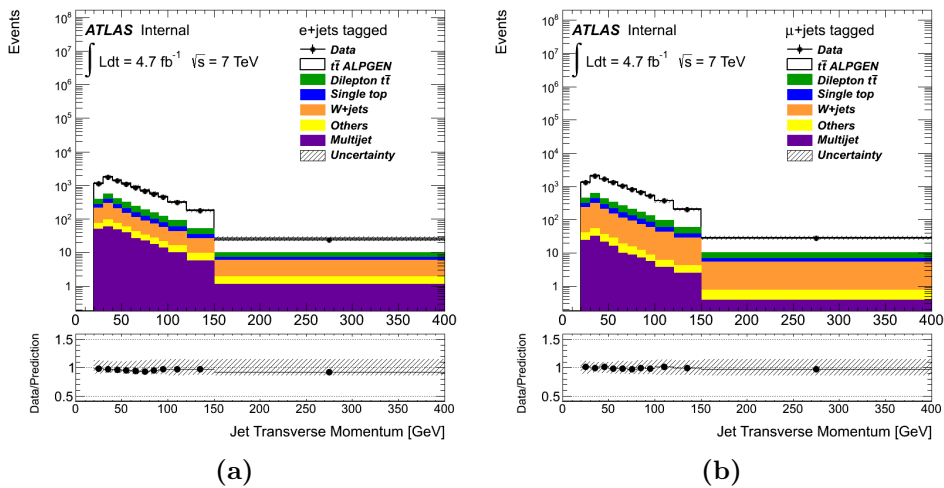


**Figure A.1** – Jet  $p_T$  spectra for the electron (a) and muon channels (a) after the one-tag selection.

## Appendix A. Control plots with the Alpgen generator

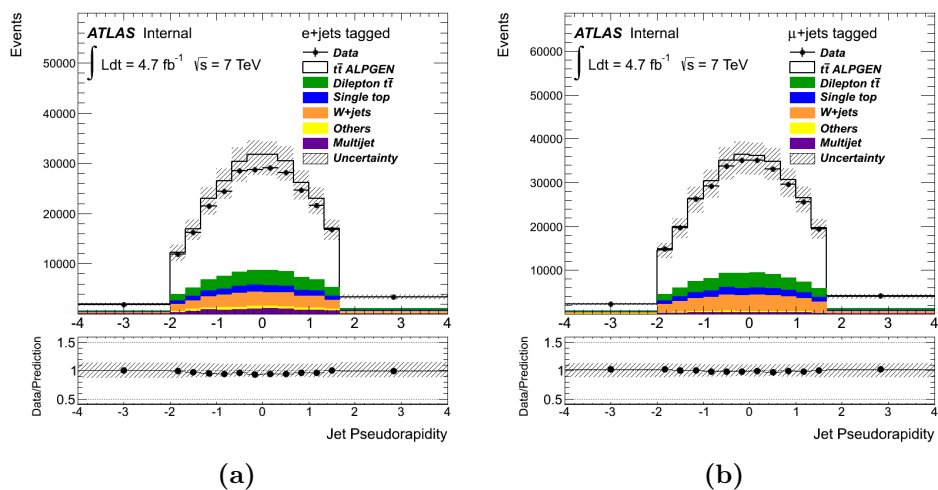


Figure A.2 – Jet  $\eta$  spectra for the electron (a) and muon channels (a) after the one-tag selection.

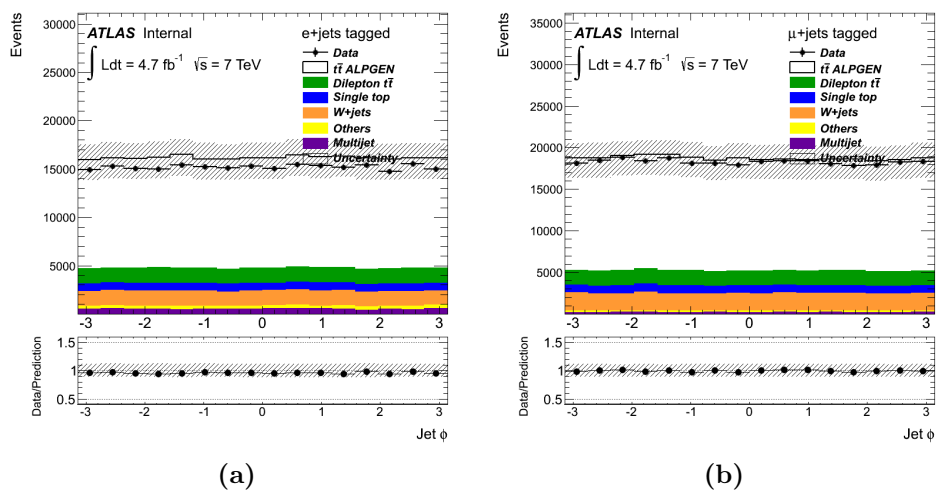
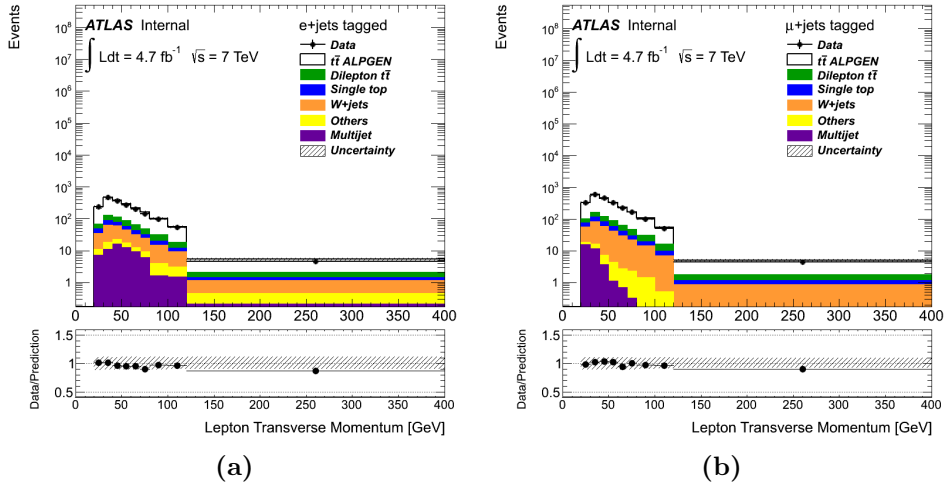


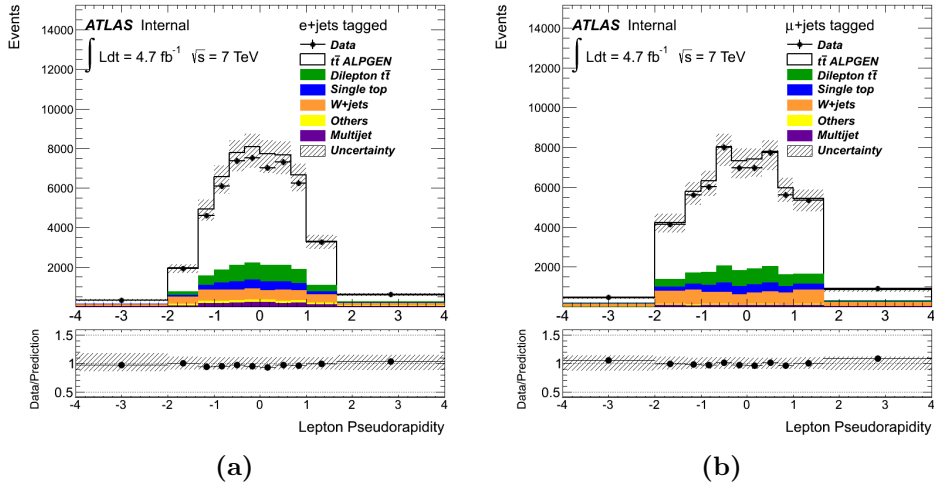
Figure A.3 – Jet  $p_T$  spectra for the electron (a) and muon channels (a) after the one-tag selection.

## A.2 Lepton-related plots

## A.2. Lepton-related plots

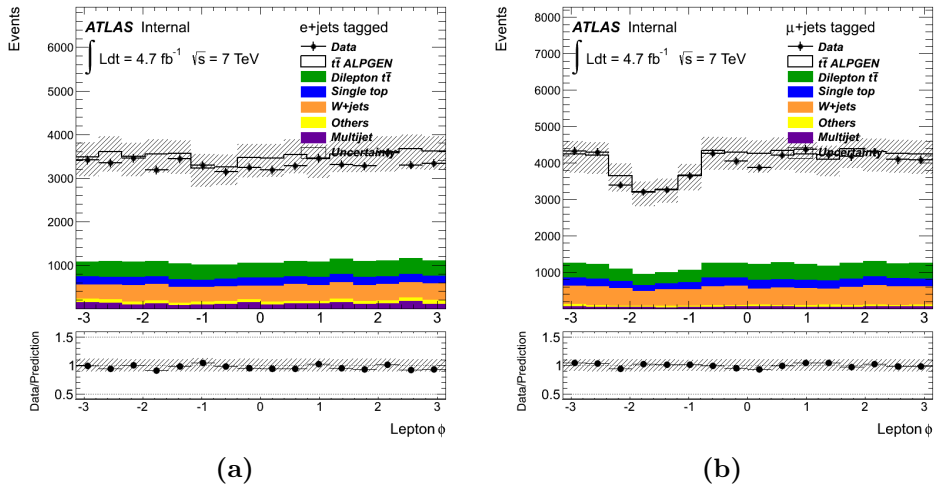


**Figure A.4** – lepton  $p_T$  spectra for the electron (a) and muon channels (a) after the one-tag selection.

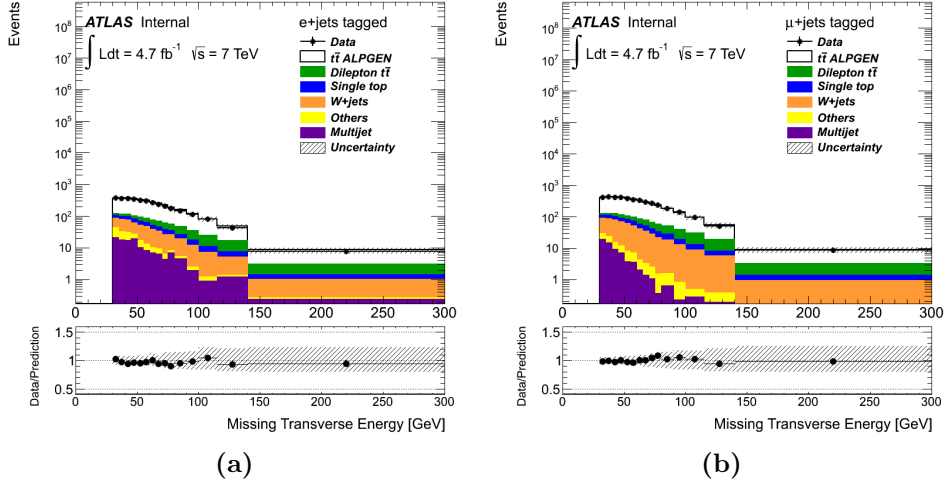


**Figure A.5** – lepton  $\eta$  spectra for the electron (a) and muon channels (a) after the one-tag selection.

## Appendix A. Control plots with the Alpgen generator



**Figure A.6** – lepton  $p_T$  spectra for the electron (a) and muon channels (a) after the one-tag selection.

A.3  $\cancel{E}_T$ -related plots

**Figure A.7** – Missing transverse momentum spectra for the electron (a) and muon (b) channel after the one-tag selection.

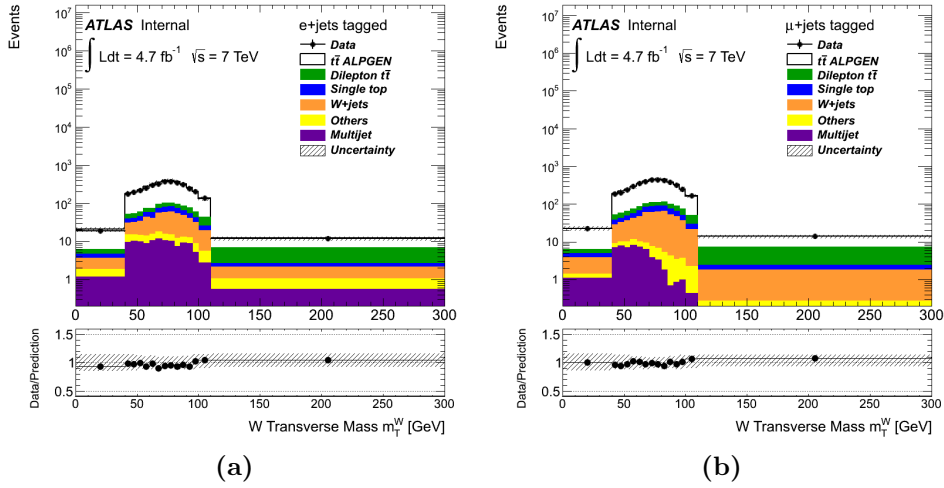


**Figure A.8** –  $W$  transverse mass (defined in (5.1)) spectra for the electron (a) and muon (b) channel after the one-tag selection.

## Appendix A. Control plots with the Alpgen generator

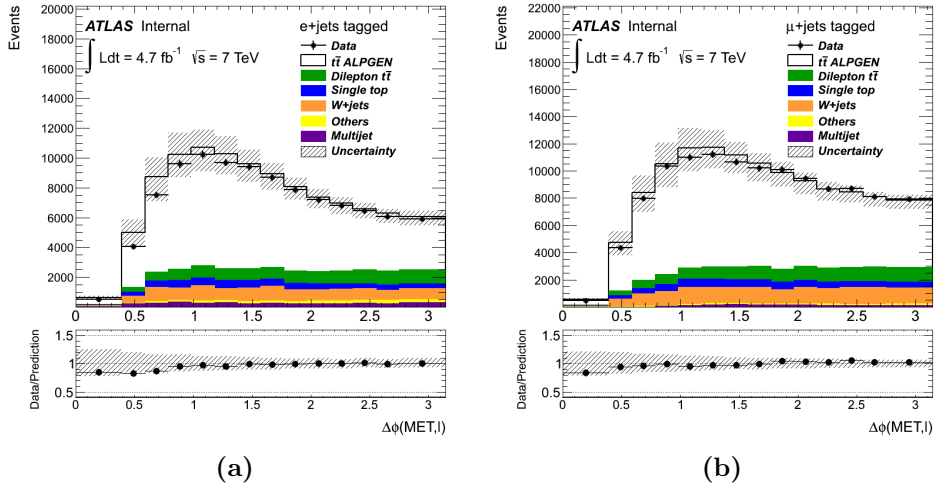


**Figure A.9** –  $\Delta\phi(\cancel{E}_T, \mathbf{p}_T^{lepton})$  spectra for the electron (a) and muon (b) channel after the one-tag selection.

---

---

## APPENDIX B

---

### UNCERTAINTIES TABLES

For the sake of compactness, the many systematic sources have been divided in five groups:

- jets (see Sect. 5.2.3);
- leptons (see Sect. 5.2.3);
- energy scale (affecting mainly the  $\cancel{E}_T$  measurement, see Sect. 5.2.3);
- fake-lepton and  $W$  background, containing the uncertainties on the data driven background estimation (see Sect. 5.2.2);
- monte Carlo gen., theory, IFSR and PDF, affecting both signal and background modeling (Sect. 5.2.1).

The uncertainty on the luminosity isn't included because, since this measurements are about the normalized cross section  $\frac{1}{\sigma} \frac{d\sigma}{dX}$ , the luminosity induced fluctuations on the  $\frac{1}{\sigma}$  systematically cancel with the ones on the  $d\sigma$  term.

## Appendix B. Uncertainties tables

### B.1 $\frac{1}{\sigma} \frac{d\sigma}{dm}$

Tab. B.1 and Tab. B.2 show the uncertainties on  $\frac{1}{\sigma} \frac{d\sigma}{dm}$  using the SVD unfolding method in the electron and muon channel, respectively. Tab. B.4 and Tab. B.5 show the same uncertainties, but obtained using the simple matrix inversion method. Tab. B.3 and Tab. B.6 show the uncertainty for the two channels, combined.

$1/\sigma d\sigma_{t\bar{t}}/dm_{t\bar{t}}$ Uncertainty [%]	$m_{t\bar{t}}, e + jets$				
	250 – 450	450 – 550	550 – 700	700 – 960	960 – 2700
Total	6/-6	5/-4	7/-6	9/-10	15/-17
Stat. only	$\pm 3$	$\pm 2$	$\pm 3$	$\pm 5$	$\pm 9$
Syst. only	5/-6	4/-4	6/-5	7/-8	12/-14
Jets	3/-3	1.2/-0.6	5/-4	5/-7	8/-12
Leptons	0.06/-0.09	0.08/-0.09	0.14/-0.02	0.04/-0.17	0/-0.7
Energy Scale	0.09/-0.05	0.07/-0.12	0.11/-0.015	0.2/-0.4	0.4/-1.4
Fake-lepton and W background	6/-6	5/-5	6/-5	4/-4	8/-9
Monte Carlo gen., theory, IFSR and PDF	1.6/-1.6	1.0/-1.0	2/-2	4/-4	10/-10

**Table B.1** – Systematic uncertainties for the normalized differential cross section with respect the mass of the system in the electron channel, using the SVD unfolding method with  $k = 3$ .

$1/\sigma d\sigma_{t\bar{t}}/dm_{t\bar{t}}$ Uncertainty [%]	$m_{t\bar{t}}, \mu + jets$				
	250 – 450	450 – 550	550 – 700	700 – 960	960 – 2700
Total	5/-5	4/-4	5/-6	7/-7	12/-12
Stat. only	$\pm 2$	$\pm 2$	$\pm 3$	$\pm 5$	$\pm 7$
Syst. only	5/-4	3/-4	4/-5	6/-6	9/-9
Jets	3/-2	1.2/-1.8	3/-4	5/-5	6/-6
Leptons	0/-0.04	0/-0.07	0.07/-0	0.11/-0.16	0.3/-0.04
Energy Scale	0.10/-0.2	0.3/-0.11	0.13/-0.10	0.15/-0.9	0.12/-1.8
Fake-lepton and W background	4/-4	4/-4	4/-4	4/-4	4/-4
Monte Carlo gen., theory, IFSR and PDF	1.1/-1.1	0.5/-0.5	1.7/-1.7	1.8/-1.8	7/-7

**Table B.2** – Systematic uncertainties for the normalized differential cross section with respect the mass of the system in the muon channel, using the SVD unfolding method with  $k = 3$ .

$1/\sigma d\sigma_{t\bar{t}}/dm_{t\bar{t}}$ Uncertainty [%]	$m_{t\bar{t}}, l + jets$				
	250 – 450	450 – 550	550 – 700	700 – 960	960 – 2700
Total	5/-5	4/-4	5/-5	7/-8	12/-12
Stat. only	$\pm 1.8$	$\pm 1.6$	$\pm 2$	$\pm 3$	$\pm 6$
Syst. only	5/-5	4/-4	5/-5	6/-7	10/-11
Jets	3/-3	1.2/-1.2	4/-4	5/-6	7/-8
Leptons	0/-0.02	0/-0.04	0.04/-0	0.06/-0.09	0.15/-0.019
Energy Scale	0.07/-0.08	0.2/-0.10	0/-0.04	0.18/-0.6	0.3/-0
Fake-lepton and W back- ground	5/-5	4/-4	4/-4	4/-4	5/-5
Monte Carlo gen., theory, IFSR and PDF	1.3/-1.3	0.7/-0.7	1.9/-1.9	3/-3	8/-8

**Table B.3** – Systematic uncertainties for the normalized differential cross section with respect the mass of the system in the lepton ( $e$  or  $mu$ ) + jets channel, using the SVD unfolding method with  $k = 3$ .

$1/\sigma d\sigma_{t\bar{t}}/dm_{t\bar{t}}$ Uncertainty [%]	$m_{t\bar{t}}, e + jets$				
	250 – 450	450 – 550	550 – 700	700 – 960	960 – 2700
Total	7/-8	8/-7	9/-8	11/-12	40/-40
Stat. only	$\pm 3$	$\pm 5$	$\pm 6$	$\pm 9$	$\pm 30$
Syst. only	6/-7	6/-5	7/-6	7/-8	20/-40
Jets	3/-4	4/-2	6/-5	5/-8	17/-30
Leptons	0.3/-0.10	0.008/-0.7	0.8/-0.06	0/-0.5	2/-0.8
Energy Scale	0/-0.3	0/-0.9	0.8/-0.06	1.3/-0.6	3/-9
Fake-lepton and W back- ground	7/-8	6/-6	6/-5	5/-5	20/-30
Monte Carlo gen., theory, IFSR and PDF	1.5/-1.5	3/-3	2/-2	3/-3	15/-15

**Table B.4** – Systematic uncertainties for the normalized differential cross section with respect the mass of the system in the electron channel, using the simple inversion unfolding method.

## Appendix B. Uncertainties tables

$d\sigma_{t\bar{t}}/dm_{t\bar{t}}$	$m_{t\bar{t}}, \mu + jets$				
	250 – 450	450 – 550	550 – 700	700 – 960	960 – 2700
Uncertainty [%]					
Total	14/-12	20/-19	17/-15	20/-19	30/-30
Stat. only	$\pm 2$	$\pm 4$	$\pm 6$	$\pm 7$	$\pm 16$
Syst. only	13/-12	20/-18	16/-14	21/-18	30/-20
Luminosity	4/-4	4/-4	4/-4	4/-4	4/-4
Jets	10/-8	18/-16	14/-12	20/-17	30/-30
Leptons	0/-0.07	0/-0.07	0.2/-0	0.3/-0.3	0/-0.3
Energy Scale	0.5/-0.6	0.08/-0.4	0/-0.6	0.7/-2	1.7/-1.7
Fake-lepton and W back-ground	9/-9	7/-7	8/-8	7/-7	11/-11
Monte Carlo gen., theory, IFSR and PDF	6/-6	6/-6	3/-3	8/-8	11/-11

**Table B.5** – Systematic uncertainties for the normalized differential cross section with respect the mass of the system in the muon channel, using the simple inversion unfolding method.

$d\sigma_{t\bar{t}}$	$m_{t\bar{t}}, l + jets$				
	250 – 450	450 – 550	550 – 700	700 – 960	960 – 2700
Uncertainty [%]					
Total	15/-14	20/-18	19/-16	20/-20	30/-30
Stat. only	$\pm 1.7$	$\pm 3$	$\pm 4$	$\pm 6$	$\pm 14$
Syst. only	15/-14	20/-18	18/-16	20/-20	30/-30
Luminosity	4/-4	4/-4	4/-4	4/-4	5/-5
Jets	10/-8	17/-14	16/-14	20/-18	30/-30
Leptons	0/-0.04	0/-0.04	0.12/-0	0.20/-0.17	0/-0.13
Energy Scale	0.5/-0.17	0.3/-0.3	0.6/-0.3	0.7/-1.2	1.9/-0
Fake-lepton and W back-ground	15/-15	11/-11	11/-11	12/-12	21/-21
Monte Carlo gen., theory, IFSR and PDF	6/-6	6/-6	3/-3	7/-7	9/-9

**Table B.6** – Systematic uncertainties for the normalized differential cross section with respect the mass of the system in the lepton ( $e$  or  $mu$ ) + jets channel, using the simple inversion unfolding method.

## B.2 $\frac{1}{\sigma}d\sigma/dp_T$

Tab. B.7 and Tab. B.8 show the uncertainties on  $\frac{1}{\sigma} \frac{d\sigma}{dp_T}$  using the SVD unfolding method in the electron and muon channel, respectively. Tab. B.10 and Tab. B.11 show the same uncertainties, but obtained using the simple matrix inversion method. Tab. B.9 and Tab. B.12 show the uncertainty for the two channels, combined.

$1/\sigma d\sigma_{t\bar{t}}/dp_{T,t\bar{t}}$ Uncertainty [%]	$p_{T,t\bar{t}}, e + jets$			
	0 – 40	40 – 170	170 – 340	340 – 1200
Total	12/-12	9/-9	20/-21	30/-30
Stat. only	$\pm 3$	$\pm 3$	$\pm 7$	$\pm 12$
Syst. only	12/-12	8/-8	19/-19	20/-20
Jets	8/-8	5/-6	13/-15	16/-19
Leptons	0.4/-0.2	0.2/-0.2	0.9/-0.15	1.8/-0.10
Energy Scale	3/-4	3/-3	3/-1.5	3/-0.3
Fake-lepton and W background	4/-4	4/-4	7/-7	8/-9
Monte Carlo gen., theory, IFSR and PDF	10/-10	7/-7	20/-20	20/-20

**Table B.7** – Systematic uncertainties for the normalized differential cross section with respect the Pt of the system in the electron channel, using the SVD unfolding method with  $k = 3$ .

$1/\sigma d\sigma_{t\bar{t}}/dp_{T,t\bar{t}}$ Uncertainty [%]	$p_{T,t\bar{t}}, \mu + jets$			
	0 – 40	40 – 170	170 – 340	340 – 1200
Total	13/-12	8/-9	20/-20	30/-30
Stat. only	$\pm 3$	$\pm 3$	$\pm 6$	$\pm 12$
Syst. only	13/-12	8/-9	19/-19	20/-20
Jets	10/-8	5/-7	14/-15	17/-17
Leptons	0.08/-0.02	0.013/-0.06	0.06/-0.08	0.3/-0.05
Energy Scale	4/-3	2/-3	1.7/-4	0.8/-1.7
Fake-lepton and W background	5/-5	4/-4	3/-3	4/-4
Monte Carlo gen., theory, IFSR and PDF	11/-11	7/-7	21/-21	30/-30

**Table B.8** – Systematic uncertainties for the normalized differential cross section with respect the Pt of the system in the muon channel, using the SVD unfolding method with  $k = 3$ .

## Appendix B. Uncertainties tables

$1/\sigma d\sigma_{t\bar{t}}/dp_{T,t\bar{t}}$	$p_{T,t\bar{t}}, l + jets$			
Uncertainty [%]	0 – 40	40 – 170	170 – 340	340 – 1200
Total	12/-12	8/-9	19/-20	20/-30
Stat. only	$\pm 2$	$\pm 1.9$	$\pm 5$	$\pm 9$
Syst. only	12/-12	8/-9	19/-19	20/-20
Jets	9/-8	5/-6	13/-15	17/-18
Leptons	0.05/-0.010	0.006/-0.04	0.03/-0.04	0.18/-0.02
Energy Scale	4/-3	3/-3	2/-3	2.0/-1.8
Fake-lepton and W background	4/-4	4/-4	5/-5	7/-7
Monte Carlo gen., theory, IFSR and PDF	11/-11	7/-7	20/-20	30/-30

**Table B.9** – Systematic uncertainties for the normalized differential cross section with respect the Pt of the system in the lepton ( $e$  or  $mu$ ) + jets channel, using the SVD unfolding method with  $k = 3$ .

$1/\sigma d\sigma_{t\bar{t}}/dp_{T,t\bar{t}}$	$p_{T,t\bar{t}}, e + jets$			
Uncertainty [%]	0 – 40	40 – 170	170 – 340	340 – 1200
Total	15/-15	11/-11	30/-30	30/-30
Stat. only	$\pm 3$	$\pm 3$	$\pm 10$	$\pm 30$
Syst. only	14/-15	11/-11	30/-30	12/-11
Jets	9/-10	6/-7	14/-16	6/-8
Leptons	0.4/-0.4	0.3/-0.4	0.8/-0.4	5/-0.18
Energy Scale	4/-5	5/-4	1.9/-1.7	6/-0
Fake-lepton and W background	4/-4	4/-4	9/-11	6/-6
Monte Carlo gen., theory, IFSR and PDF	12/-12	9/-9	30/-30	11/-11

**Table B.10** – Systematic uncertainties for the normalized differential cross section with respect the Pt of the system in the electron channel, using the simple inversion unfolding method.

$1/\sigma d\sigma_{t\bar{t}}/dp_{T,t\bar{t}}$	$p_{T,t\bar{t}}, \mu + jets$			
Uncertainty [%]	0 – 40	40 – 170	170 – 340	340 – 1200
Total	17/-15	10/-11	30/-30	30/-30
Stat. only	$\pm 3$	$\pm 3$	$\pm 9$	$\pm 30$
Syst. only	16/-15	10/-11	30/-30	20/-20
Jets	13/-10	6/-9	19/-16	20/-20
Leptons	0.12/-0.04	0.05/-0.10	0/-0.4	2/-0
Energy Scale	6/-5	4/-5	0.7/-2	6/-0
Fake-lepton and W background	5/-5	4/-4	5/-5	6/-7
Monte Carlo gen., theory, IFSR and PDF	14/-14	9/-9	30/-30	12/-12

**Table B.11** – Systematic uncertainties for the normalized differential cross section with respect the Pt of the system in the muon channel, using the simple inversion unfolding method.

$1/\sigma d\sigma_{t\bar{t}}/dp_{T,t\bar{t}}$	$p_{T,t\bar{t}}, l + jets$			
Uncertainty [%]	0 – 40	40 – 170	170 – 340	340 – 1200
Total	13/-12	8/-9	20/-20	30/-30
Stat. only	$\pm 2$	$\pm 1.9$	$\pm 5$	$\pm 9$
Syst. only	12/-12	8/-9	20/-19	30/-20
Jets	9/-8	5/-6	13/-15	17/-18
Leptons	0/-0	0/-0	0/-0	0/-0
Energy Scale	4/-3	3/-3	2/-3	2.0/-1.8
Fake-lepton and W background	4/-4	4/-4	5/-5	7/-7
Monte Carlo gen., theory, IFSR and PDF	11/-11	7/-7	20/-20	30/-30

**Table B.12** – Systematic uncertainties for the normalized differential cross section with respect the Pt of the system in the lepton ( $e$  or  $mu$ ) + jets channel, using the simple inversion unfolding method.

### B.3 $\frac{1}{\sigma}d\sigma/dY$

Tab. B.13 and Tab. B.14 show the uncertainties on  $\frac{1}{\sigma} \frac{d\sigma}{dm}$  using the SVD unfolding method in the electron and muon channel, respectively. Tab. B.16 and Tab. B.17 show the same uncertainties, but obtained using the simple matrix inversion method. Tab. B.15 and Tab. B.18 shows the uncertainty for the two channels, combined.

$1/\sigma d\sigma_{t\bar{t}}/dy_{t\bar{t}}$	$y_{t\bar{t}}, e + jets$					
Uncertainty [%]	-2.5 – -1	-1 – -0.5	-0.5 – 0	0 – 0.5	0.5 – 1	1 – 2.5
Total	7/-8	5/-5	5/-5	5/-5	5/-5	7/-7
Stat. only	$\pm 5$	$\pm 3$	$\pm 3$	$\pm 3$	$\pm 3$	$\pm 5$
Syst. only	6/-7	4/-4	4/-4	4/-4	4/-4	4/-5
Jets	3/-5	0.7/-0.9	1.5/-1.0	1.4/-1.3	0.4/-0.10	1.4/-1.8
Leptons	0.16/-0.7	0.3/-0.13	0.2/-0.08	0.014/-0.3	0.09/-0.08	0.5/-0.3
Energy Scale	0.02/-0.9	0.06/-0.2	0.016/-0.14	0.13/-0.09	0.5/-0	0.3/-0.3
Fake-lepton and W background	7/-8	4/-4	4/-4	4/-4	4/-4	4/-5
Monte Carlo gen., theory, IFSR and PDF	0.8/-0.7	1.3/-1.3	0.7/-0.7	0.9/-0.9	0.5/-0.5	2/-2

**Table B.13** – Systematic uncertainties for the normalized differential cross section with respect the Rapidity of the system in the electron channel, using the SVD unfolding method with  $k = 3$ .

## Appendix B. Uncertainties tables

$1/\sigma d\sigma_{t\bar{t}}/dy_{t\bar{t}}$	$y_{t\bar{t}}, \mu + jets$					
Uncertainty [%]	-2.5 - -1	-1 - -0.5	-0.5 - 0	0 - 0.5	0.5 - 1	1 - 2.5
Total	6/-6	4/-4	4/-4	4/-4	4/-4	6/-6
Stat. only	$\pm 4$	$\pm 3$	$\pm 2$	$\pm 2$	$\pm 3$	$\pm 4$
Syst. only	4/-4	4/-4	4/-4	3/-3	3/-3	4/-4
Jets	1.8/-3	0.3/-0.4	1.2/-1.1	0.8/-0.9	0.6/-0.6	2/-1.5
Leptons	0/-0.04	0.07/-0	0/-0.12	0.14/-0	0/-0.08	0.04/-0.07
Energy Scale	0.15/-0.6	0.19/-0.07	0.007/-0.06	0.18/-0.11	0.18/-0.016	0/-0.6
Fake-lepton and W background	4/-4	4/-4	3/-3	3/-3	3/-3	3/-3
Monte Carlo gen., theory, IFSR and PDF	1.0/-1.0	0.5/-0.5	0.3/-0.3	0.4/-0.4	0.4/-0.4	1.7/-1.7

**Table B.14** – Systematic uncertainties for the normalized differential cross section with respect the Rapidity of the system in the muon channel, using the SVD unfolding method with  $k = 3$ .

$1/\sigma d\sigma_{t\bar{t}}/dy_{t\bar{t}}$	$y_{t\bar{t}}, l + jets$					
Uncertainty [%]	-2.5 - -1	-1 - -0.5	-0.5 - 0	0 - 0.5	0.5 - 1	1 - 2.5
Total	5/-6	4/-4	4/-4	4/-4	4/-4	5/-5
Stat. only	$\pm 3$	$\pm 1.9$	$\pm 1.8$	$\pm 1.9$	$\pm 2.0$	$\pm 3$
Syst. only	4/-5	4/-4	4/-4	4/-4	4/-4	4/-4
Jets	2/-4	0.5/-0.6	1.1/-0.8	1.0/-1.0	0.5/-0.3	1.5/-1.3
Leptons	0/-0.02	0.04/-0	0/-0.07	0.08/-0	0/-0.04	0.03/-0.04
Energy Scale	0.08/-0.7	0.02/-0.05	0.07/-0.02	0.2/-0	0.3/-0	0.2/-0
Fake-lepton and W background	4/-5	4/-4	4/-4	4/-4	4/-4	4/-4
Monte Carlo gen., theory, IFSR and PDF	0.6/-0.6	0.9/-0.9	0.4/-0.4	0.7/-0.7	0.3/-0.3	1.8/-1.8

**Table B.15** – Systematic uncertainties for the normalized differential cross section with respect the Rapidity of the system in the lepton ( $e$  or  $mu$ ) + jets channel, using the SVD unfolding method with  $k = 3$ .

$1/\sigma d\sigma_{t\bar{t}}/dy_{t\bar{t}}$	$y_{t\bar{t}}, e + jets$					
Uncertainty [%]	-2.5 - -1	-1 - -0.5	-0.5 - 0	0 - 0.5	0.5 - 1	1 - 2.5
Total	11/-13	6/-6	6/-6	6/-6	6/-6	7/-8
Stat. only	$\pm 7$	$\pm 5$	$\pm 4$	$\pm 4$	$\pm 5$	$\pm 6$
Syst. only	8/-11	4/-4	4/-4	4/-4	4/-4	5/-5
Jets	5/-8	1.1/-0.7	1.8/-0.9	1.2/-2	1.6/-0.4	1.0/-2
Leptons	0.14/-0.5	0.4/-0.6	0.9/-0.15	0/-1.0	1.2/-0	0.8/-0.9
Energy Scale	0/-1.8	0.2/-0.08	0.08/-0.4	0.06/-0.3	0/-0.9	0.11/-0.5
Fake-lepton and W background	11/-13	6/-5	4/-4	4/-4	4/-4	5/-5
Monte Carlo gen., theory, IFSR and PDF	2/-2	0.9/-0.9	1.1/-1.1	1.5/-1.5	0.17/-0.17	2/-2

**Table B.16** – Systematic uncertainties for the normalized differential cross section with respect the Rapidity of the system in the electron channel, using the simple inversion unfolding method.

$1/\sigma d\sigma_{t\bar{t}}/dy_{t\bar{t}}$	$y_{t\bar{t}}, \mu + jets$					
Uncertainty [%]	-2.5 - -1	-1 - -0.5	-0.5 - 0	0 - 0.5	0.5 - 1	1 - 2.5
Total	6/-7	6/-6	5/-5	5/-5	6/-6	6/-6
Stat. only	$\pm 4$	$\pm 4$	$\pm 4$	$\pm 4$	$\pm 4$	$\pm 4$
Syst. only	4/-5	4/-4	4/-4	4/-3	4/-4	5/-5
Jets	3/-5	1.3/-1.0	2/-1.7	0.8/-0.6	3/-1.7	3/-2
Leptons	0/-0.05	0.07/-0.3	0/-0.4	0.5/-0	0.03/-0.05	0.04/-0.09
Energy Scale	0.2/-1.5	1.5/-0.04	0/-0.8	0.2/-0.3	0.5/-0.09	0/-1.1
Fake-lepton and W background	4/-4	4/-4	3/-4	4/-3	3/-3	3/-3
Monte Carlo gen., theory, IFSR and PDF	0.8/-0.8	0.3/-0.3	0.15/-0.15	0.6/-0.6	0.8/-0.8	2.0/-2.0

**Table B.17** – Systematic uncertainties for the normalized differential cross section with respect the Rapidity of the system in the muon channel, using the simple inversion unfolding method.

## Appendix B. Uncertainties tables

---

$1/\sigma d\sigma_{t\bar{t}}/dy_{t\bar{t}}$	$y_{t\bar{t}}, l + jets$					
Uncertainty [%]	-2.5 - -1	-1 - -0.5	-0.5 - 0	0 - 0.5	0.5 - 1	1 - 2.5
Total	6/-7	5/-5	5/-5	5/-5	5/-5	6/-6
Stat. only	$\pm 4$	$\pm 3$	$\pm 3$	$\pm 3$	$\pm 3$	$\pm 3$
Syst. only	5/-6	4/-3	4/-4	4/-4	4/-4	5/-5
Jets	3/-6	0.7/-0.4	1.9/-1.2	0.6/-1.4	0.3/-0.3	1.8/-2
Leptons	0/-0.04	0.03/-0.15	0/-0.2	0.2/-0	0.015/-0.03	0.02/-0.05
Energy Scale	0.12/-1.5	0.9/-0.03	0.007/-0.6	0.3/-0.18	0.7/-0	0.7/-0
Fake-lepton and W back-ground	6/-6	4/-4	4/-4	4/-4	4/-4	4/-4
Monte Carlo gen., theory, IFSR and PDF	0.8/-0.8	0.5/-0.5	0.6/-0.6	1.0/-1.0	0.3/-0.3	2/-2

**Table B.18** – Systematic uncertainties for the normalized differential cross section with respect the Rapidity of the system in the lepton ( $e$  or  $\mu$ ) + jets channel, using the simple inversion unfolding method.

---

---

## APPENDIX C

---

### DIFFERENTIAL CROSS SECTION USING THE TWO-TAGS SELECTION

In this appendix, the *very* preliminary results using the two-tags selection are presented. Requiring at least two jets tagged as coming from a  $b$  quark has the big advantage to drastically improve the signal-over-background ratio, since it eliminates a big fraction of the surviving  $W$  and QCD events, with minimal impact on the signal. The loss in statistics, on the other hand, it's not a big issue, since the measurement is dominated by systematic uncertainties, and can be overcome by combining the two channels (thus  $\approx$  doubling the statistics).

The real problem, that prevented the measurement to adopt this selection in the first place, is the still poor knowledge of the behavior of the tagger algorithm response when requiring two  $b$ -tags. This affects the systematic on the  $b$ -tag scale factors as well the evaluation of the data-driven backgrounds. The results presented in this appendix are thus to be considered preliminary,

## Appendix C. Differential cross section using the two-tags selection

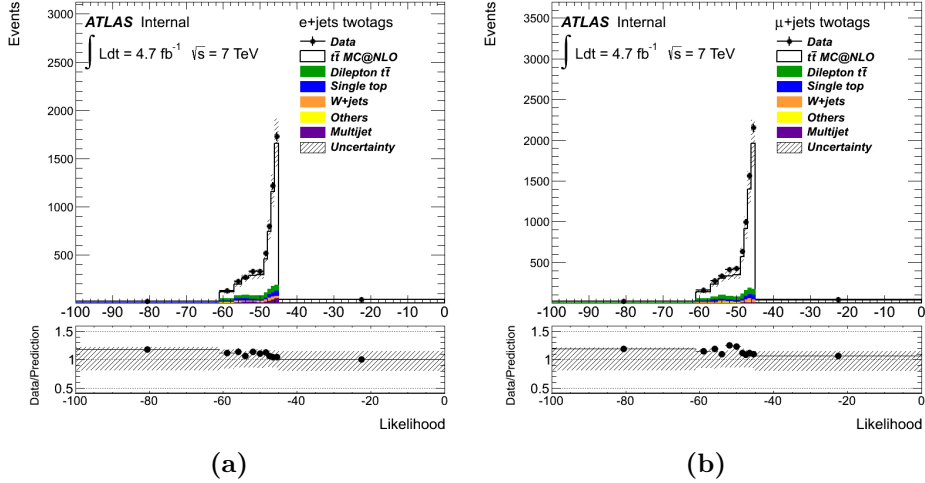


**Figure C.1** – Kinematic fit likelihood distribution in the two-tags sample for the electron channel (a) and muon channel (a).

since the one-tag recipes and methods for the evaluation of the systematics and data driven backgrounds are used. Even the likelihood cut is the same of the one-tag selection (in principle it should be re-optimized). Fig. C.1, anyway, shows no big changes in the likelihood distribution respect to the same distribution obtained in the one-tag selection (Fig. 6.2).

Only results from the combined sample, with the SVD unfolding, are presented.

### C.1 Reconstructed spectra, efficiencies and migration matrices

For the following spectra, the binning is the one described in Tab. 6.1. For all the distributions the agreement of the measurements with our MC predictions is worse than the one-tag selection, but still within the bands due to the systematic uncertainties.

## C.1. Reconstructed spectra, efficiencies and migration matrices

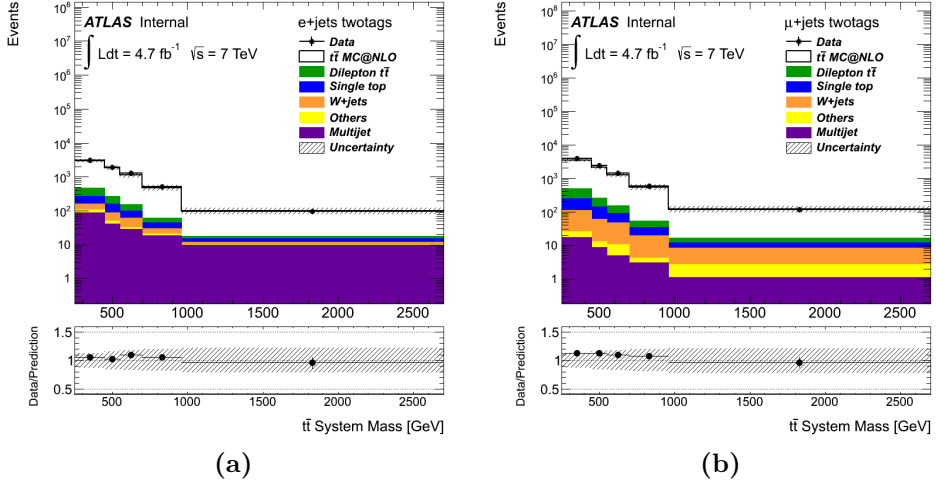


**Figure C.2** –  $t\bar{t}$  mass spectra in the electron (a) and muon (b) channel after the two-tags selection.

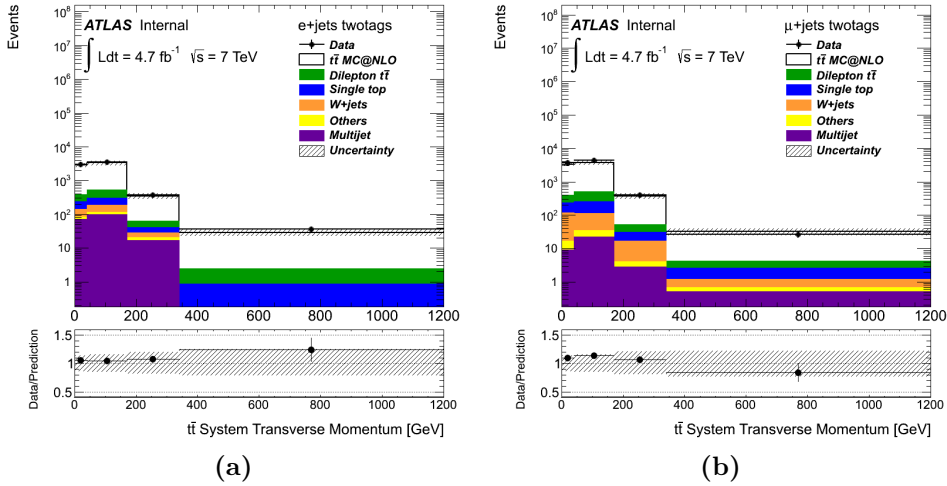


**Figure C.3** –  $t\bar{t}$   $p_T$  spectra in the electron (a) and muon (b) channel after the two-tags selection.

## Appendix C. Differential cross section using the two-tags selection

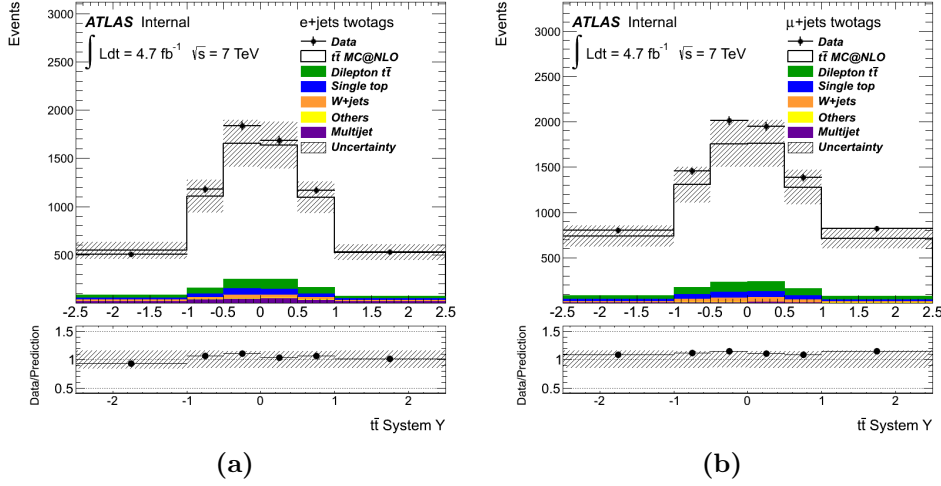


**Figure C.4** –  $t\bar{t}$  rapidity spectra in the electron (a) and muon (b) channel after the two-tags selection.

The migration matrices, in Fig. C.5-Fig. C.7, show a very slight, and probably not significant, improvement (a better “diagonality”) with respect those obtained in the one tag selection.

The efficiency plots, Fig. C.8-Fig. C.10, show a flat efficiency loss of the order of 50%, that can be compensated by combining the two channels.

## C.1. Reconstructed spectra, efficiencies and migration matrices

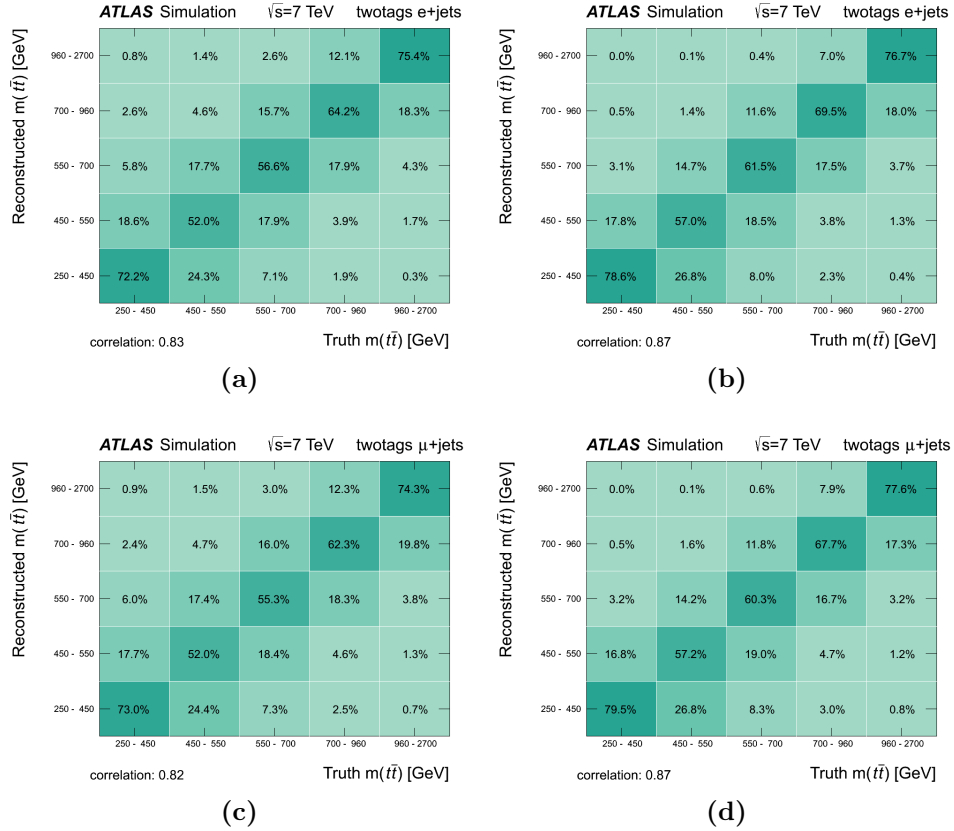


**Figure C.5** – Migration matrices for  $m_{t\bar{t}}$  without likelihood cut (right) and with likelihood cut (left) for the electron (top) and muon (bottom) after the two-tags selection.

## Appendix C. Differential cross section using the two-tags selection

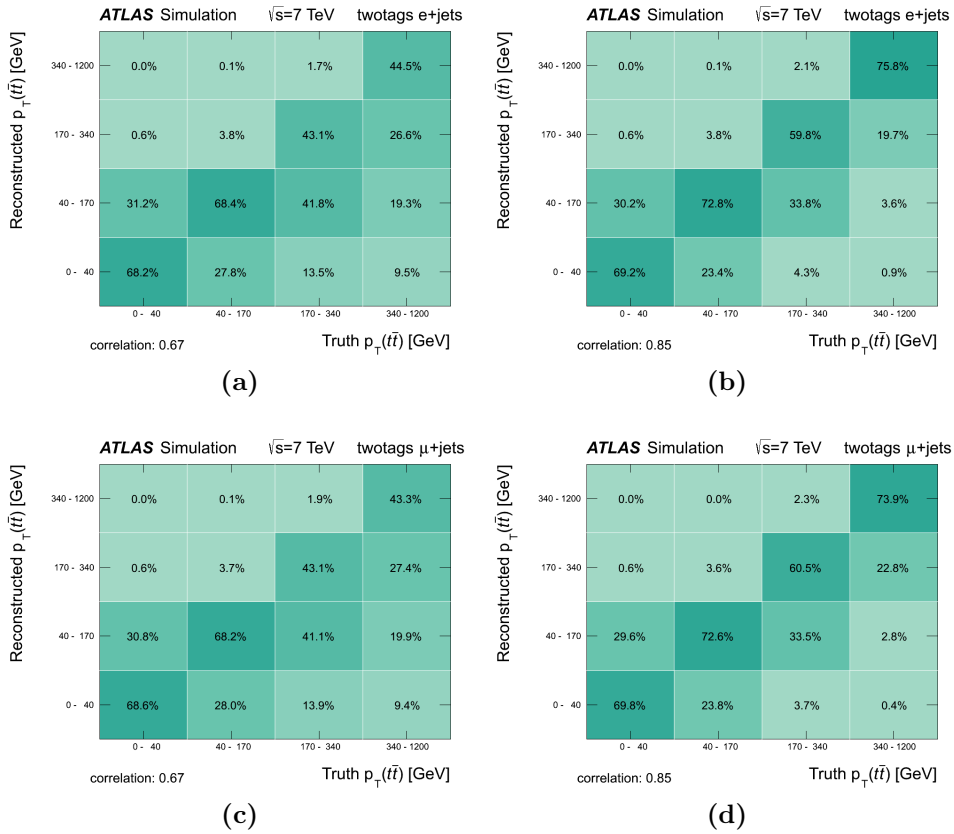


**Figure C.6** – Migration matrices for  $p_{T,t\bar{t}}$  without likelihood cut (right) and with likelihood cut (left) for the electron (top) and muon (bottom) after the two-tags selection.

## C.1. Reconstructed spectra, efficiencies and migration matrices

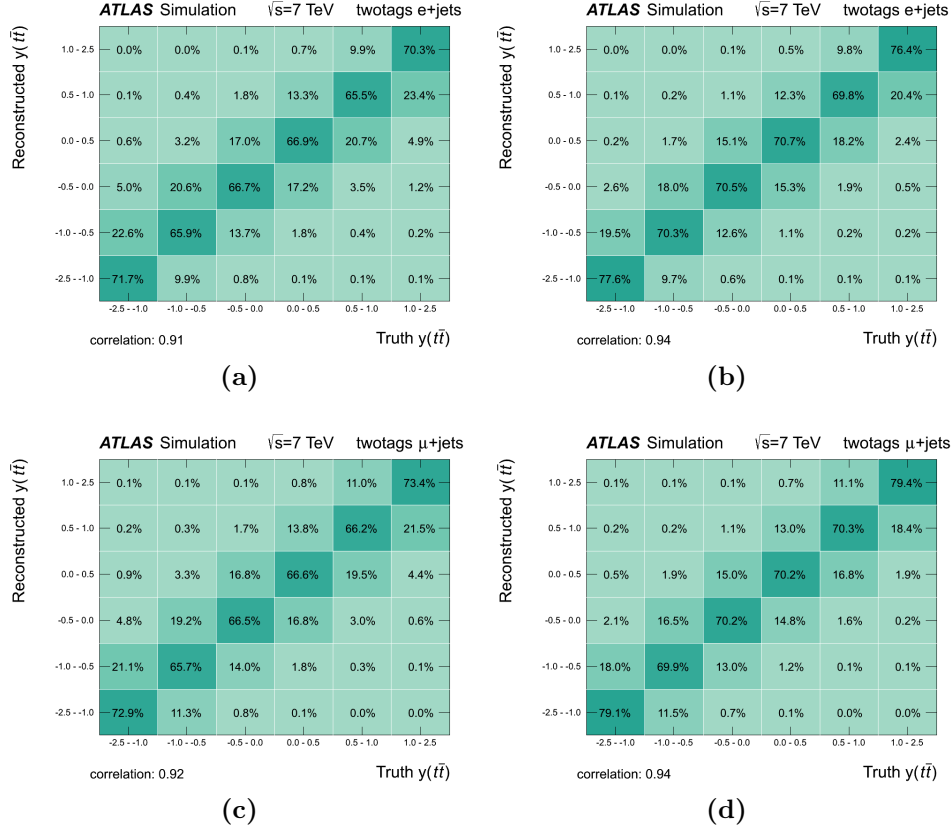


**Figure C.7** – Migration matrices for  $Y_{\bar{t}\bar{t}}$  without likelihood cut (right) and with likelihood cut (left) for the electron (top) and muon (bottom) after the two-tags selection.

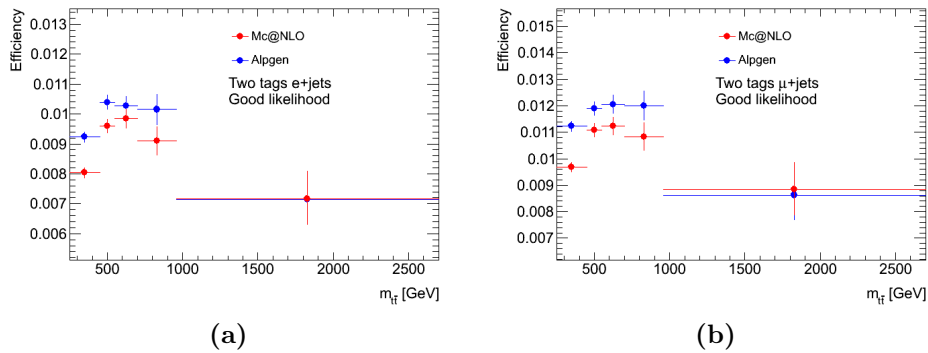


**Figure C.8** – Efficiency for the  $t\bar{t}$  mass for the electron (a) and muon (b) channel, in the two-tags selection.

## Appendix C. Differential cross section using the two-tags selection

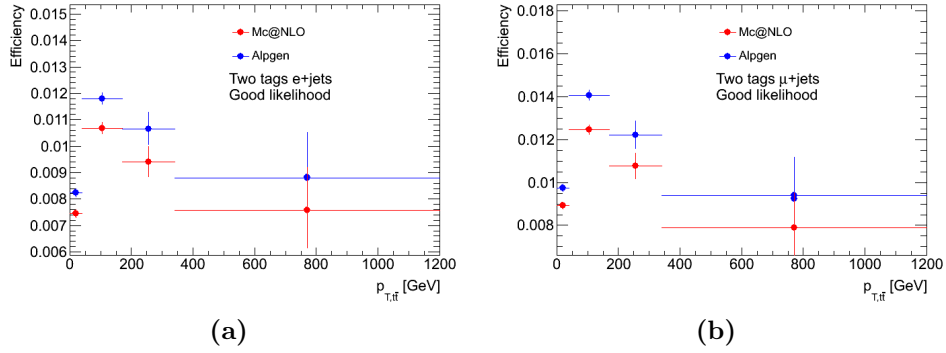


**Figure C.9** – Efficiency for the  $t\bar{t}$   $p_T$  for the electron (a) and muon (b) channel, in the two-tags selection.

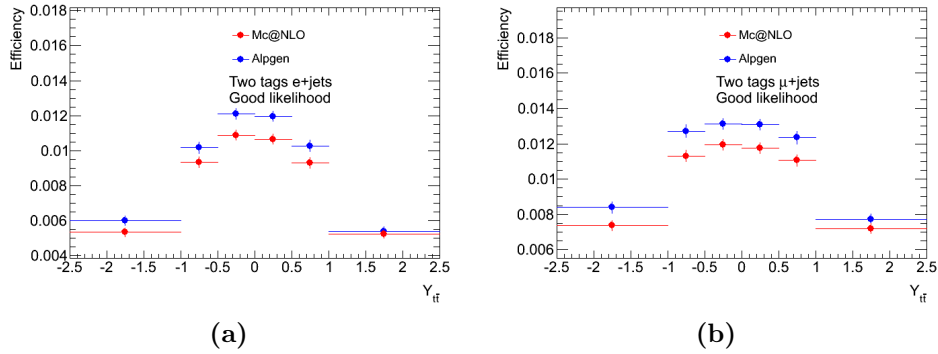


**Figure C.10** – Efficiency for the  $t\bar{t}$  rapidity for the electron (a) and muon (b) channel, in the two-tags selection.

## C.2 Results

In this section, the results obtained by applying the two-tags selections, are presented. The overall results are encouraging: even if there is a slight increase of the statistical error, there is a significant drop in the systematic uncertainties, especially those related to the QCD background. The only systematic that increases is the  $b$ -tag scale factor uncertainties, and it was expected since it becomes crucial when applying the two tags requirement.

### C.2.1 $\frac{1}{\sigma} \frac{d\sigma}{dM}$

The resulting spectrum of the unfolded normalized differential cross section as a function of the mass of the  $t\bar{t}$  system is shown in Fig. C.11 and Tab. C.1

$m_{t\bar{t}}$ [GeV]	$1/\sigma d\sigma_{t\bar{t}}/dm_{t\bar{t}}$ [1/TeV]		
	e+jets	$\mu$ +jets	l+jets
250 – 450	2.42 +0.13/-0.14	2.48 +0.18/-0.14	2.46 +0.13/-0.12
450 – 550	2.77±0.11	2.81 +0.09/-0.11	2.79 +0.08/-0.09
550 – 700	1.07±0.07	1.02 +0.08/-0.11	1.04 +0.06/-0.08
700 – 960	0.24±0.02	0.22 +0.04/-0.019	0.23 +0.03/-0.018
960 – 2700	0.0079±0.0012	0.0071 +0.0014/-0.001	0.0075 +0.0011/-0.0009

**Table C.1** – Normalized differential  $t\bar{t}$  production cross section as a function of the mass of the system, unfolded using the SVD method with regularization parameter  $k = 3$ .

## Appendix C. Differential cross section using the two-tags selection

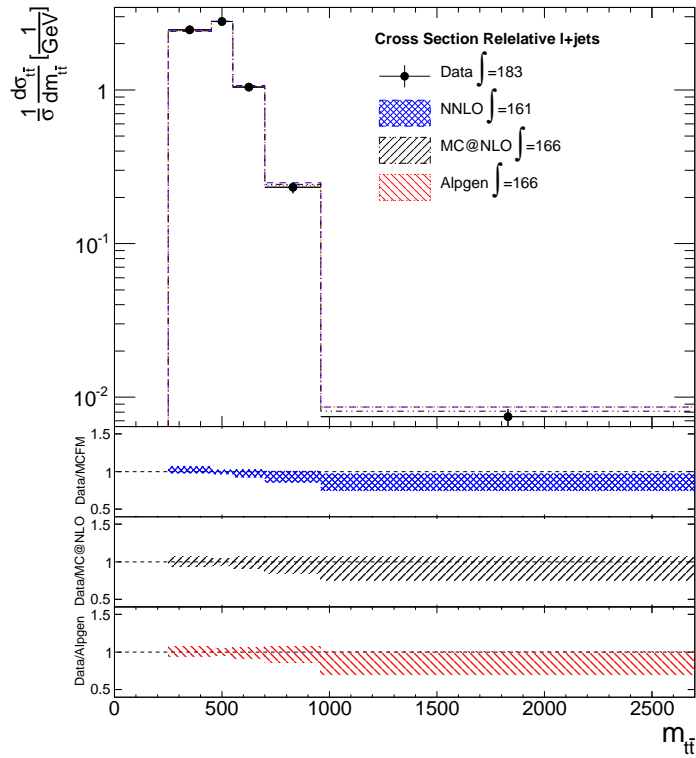


**Figure C.11** – Normalized differential  $t\bar{t}$  production cross section as a function of the mass of the system for the combined sample after the two-tags selection, unfolded using the SVD method.

### C.2.2 $\frac{1}{\sigma} \frac{d\sigma}{dp_T}$

The resulting spectrum of the unfolded normalized differential cross section as a function of the Pt of the  $t\bar{t}$  system is shown in Fig. C.12 and Tab. C.2

$p_{T,t\bar{t}}$ [GeV]	$1/\sigma d\sigma_{t\bar{t}}/dp_{T,t\bar{t}}$ [1/TeV]		
	e+jets	$\mu$ +jets	l+jets
0 – 40	$14 \pm 1.5$	$13.7 \pm 1.6$	$13.8 \pm 1.5$
40 – 170	$3 \pm 0.3$	$3.1 \pm 0.3$	$3 \pm 0.3$
170 – 340	$0.28 \pm 0.05$	$0.25 +0.06/-0.08$	$0.26 +0.05/-0.06$
340 – 1200	$0.0067 \pm 0.0015$	$0.005 +0.003/-0.0015$	$0.006 +0.002/-0.0014$

**Table C.2** – Normalized differential  $t\bar{t}$  production cross section as a function of the Pt of the system, unfolded using the SVD method with regularization parameter  $k = 3$ .

## Appendix C. Differential cross section using the two-tags selection

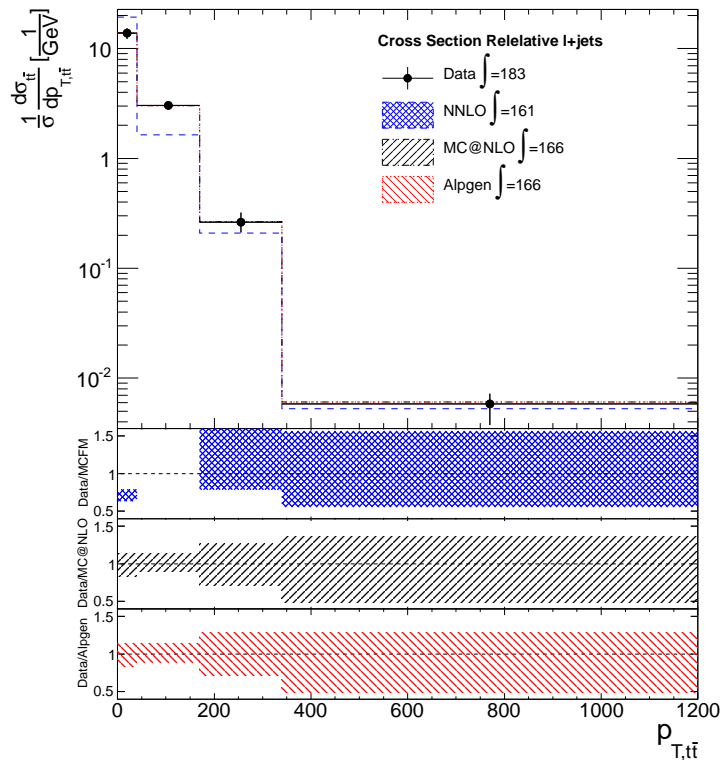


**Figure C.12** – Normalized differential  $t\bar{t}$  production cross section as a function of the  $P_t$  of the system for the combined sample after the two-tags selection, unfolded using the SVD method.

### C.2.3 $\frac{1}{\sigma} \frac{d\sigma}{dY}$

The resulting spectrum of the unfolded normalized differential cross section as a function of the rapidity of the  $t\bar{t}$  system is shown in and Tab. C.3

$y_{t\bar{t}}$	$1/\sigma d\sigma_{t\bar{t}}/dy_{t\bar{t}}$ [1/TeV]		
	e+jets	$\mu$ +jets	l+jets
-2 - -1	0.143±0.01	0.128 +0.019/-0.009	0.134 +0.012/-0.007
-1 - -0.5	0.343±0.019	0.32 +0.04/-0.017	0.33 +0.02/-0.015
-0.5 - 0	0.43±0.02	0.428 +0.019/-0.05	0.427 +0.018/-0.03
0 - 0.5	0.42±0.02	0.43 +0.04/-0.02	0.42 +0.03/-0.018
0.5 - 1	0.326±0.017	0.321±0.016	0.323±0.014
1 - 2	0.126±0.007	0.128 +0.006/-0.017	0.128 +0.005/-0.011

**Table C.3** – Normalized differential  $t\bar{t}$  production cross section as a function of the rapidity of the system, unfolded using the SVD method with regularization parameter  $k = 3$ .



---

## LIST OF FIGURES

1.1	The known fundamental fermions and gauge bosons . . . . .	2
1.2	Higgs self-interactions Feynman diagrams. . . . .	5
1.3	Feynman diagram leading to a triangular anomaly. . . . .	10
1.4	Leading-order Feynman diagrams for top-antitop pair production . . . . .	11
1.5	NLO Feynman diagrams for top-antitop pair production . . . . .	11
1.6	(a): $t\bar{t}$ production cross section as a function of top mass at the LHC. (b): $t\bar{t}$ production at the LHC as a function of the center of mass energy . . . . .	13
1.7	PDFs of some of the quarks and gluons inside the proton . . . . .	14
1.8	Single top production channels . . . . .	14
1.9	Examples of diagrams contributing to $Wt$ production at NLO . . . . .	15
1.10	Top and anti-top decay chains. . . . .	17
1.11	Virtual top quark loops contributing to the $W^-$ - and $Z$ -boson masses. . . . .	20
1.12	Overview of the $m_t$ measurements . . . . .	21

## LIST OF FIGURES

---

2.1	Schematic view of the CERN accelerator complex . . . . .	24
2.2	Online plot of the cumulative luminosity versus day delivered to, and recorded by ATLAS during stable beams and for pp collisions at 7 TeV center-of-mass energy 2011 . . . . .	26
2.3	Online plot of the cumulative luminosity versus day delivered to, and recorded by ATLAS during stable beams and for pp collisions at 7 TeV center-of-mass energy in 2011 . . . . .	27
2.4	Online plot of the cumulative luminosity versus day delivered to, and recorded by ATLAS during stable beams and for pp collisions at 7 TeV center-of-mass energy in 2012 . . . . .	28
2.5	Sliced view of the ATLAS detector, with the indications of the main sub-systems. . . . .	29
2.6	The ATLAS toroid magnetic system layout. . . . .	31
2.7	Longitudinal ((a)) and transversal ((b)) schematic view of the ATLAS inner systems. . . . .	32
2.8	Schematic view of the ATLAS calorimeter system. . . . .	36
2.9	A sliced view of the ATLAS Muons Spectrometer. . . . .	40
2.10	ATLAS trigger and data acquisition system. . . . .	43
3.1	Number of events per period divided by the luminosity of the period . . . . .	46
3.2	Schematic workflow of a typical Monte Carlo event generation. . . . .	49
3.3	Example of parton shower. . . . .	50
3.4	Number of jets spectra in the electron channel after the one-tag selection (as described in Chapter 5) using the MC@NLO generator (a) and the Alpgen generator (b) to model the signal. . . . .	60

3.5	Number of jets spectra in the muon channel after the one-tag selection (as described in Chapter 5) using the MC@NLO generator (a) and the Alpgen generator (b) to model the signal.	60
3.6	$t\bar{t}$ $p_T$ spectra using Madgraph [61] without (red) and with (blue) parton shower, Alpgen+Herwig (green) and MC@NLO+Herwig (black).	61
3.7	Meaning of the Pythia parameters used for the up and down variations.	61
4.1	Leading order Feynman diagram of the “semileptonic” $t\bar{t}$ topology.	76
4.2	Electron “tight++” scale factor as a function of the $\eta$ (a) and $E_T$ (b) of the electron.	84
4.3	Electron reconstruction efficiencies shown for different number of reconstructed primary vertices	85
4.4	Schematic representation of the different muon reconstruction methods.	86
4.5	Number of muons with respect to the <code>etcone20</code> (a) and <code>ptcone30</code> (b) variable.	89
4.6	Efficiency of the <code>etcone20</code> (requiring <code>ptcone30</code> < 2.5 GeV) (a) and <code>ptcone30</code> (requiring <code>etcone20</code> < 4 GeV) (b) selections, evaluated on the $t\bar{t}$ MC sample [66].	89
4.7	Efficiency of the possible $\Delta R(\mu, j)$ requirements as a function of the number of vertices in the event	90
4.8	Muon reconstruction efficiency as a function of $\eta$ .	91
4.9	The $\cancel{E}_{x,y}$ resolution in bins of $\sum E_T$ for the $t\bar{t}$ semileptonic selection in the electron and muon channels.	95

## LIST OF FIGURES

---

4.10	Trigger scale factors in the barrel for (a) mu18 trigger in periods B-I, (b) the mu18 medium trigger in periods J-K and (c) the mu18 medium trigger in periods L-M. . . . .	98
4.11	Trigger scale factors in the endcaps for (a) mu18 trigger in periods B-I, (b) the mu18 medium trigger in periods J-K and (c) the mu18 medium trigger in periods L-M. . . . .	99
4.12	Trigger scale factors in the barrel for the mu18 medium trigger in (a) period L data with the wrong RPC timing configuration (runs 189205-189610) and (b) the remaining period L data. . . . .	99
5.1	Definition of the PDF uncertainty envelope (data from the “dilepton” analysis in the $ee$ channel). . . . .	105
5.2	JES uncertainty for anti-kt $\Delta R = 0.4$ jets calibrated with the EM+JES scheme for the full 2011 dataset. . . . .	107
5.3	Jet $p_T$ spectra for the electron (a) and muon channels (a) after the one-tag selection. . . . .	111
5.4	Jet $\eta$ spectra for the electron (a) and muon channels (a) after the one-tag selection. . . . .	111
5.5	Jet $p_T$ spectra for the electron (a) and muon channels (a) after the one-tag selection. . . . .	112
5.6	lepton $p_T$ spectra for the electron (a) and muon channels (a) after the one-tag selection. . . . .	113
5.7	lepton $\eta$ spectra for the electron (a) and muon channels (a) after the one-tag selection. . . . .	113
5.8	lepton $p_T$ spectra for the electron (a) and muon channels (a) after the one-tag selection. . . . .	114
5.9	Missing transverse momentum spectra for the electron (a) and muon (b) channel after the one-tag selection. . . . .	115

---

5.10	$W$ transverse mass (defined in (5.1)) spectra for the electron (a) and muon (b) channel after the one-tag selection. . . . .	115
5.11	$\Delta\phi(\cancel{E}_{\mathbf{T}}, \mathbf{p}_T^{lepton})$ spectra for the electron (a) and muon (b) channel after the one-tag selection. . . . .	116
6.1	(a): the transfer functions mapping the measured electrons to the corresponding generated objects in the range objects in the range $0.8 <  \eta  < 1.37$ . (b): the transfer functions mapping the measured $b$ jets to the corresponding partonic objects in the range $ \eta  < 0.8$ . . . . .	119
6.2	Kinematic fit likelihood distribution in the tagged sample for the electron channel (a) and muon channel (a). . . . .	120
6.3	RMS of the absolute (a) and relative (b) $p_T$ reconstruction discrepancy $p_T^{reco} - p_T^{truth}$ in the electron channel. . . . .	121
6.4	RMS of the absolute (a) and relative (b) $t\bar{t}$ $p_T$ reconstruction discrepancy $p_T^{reco} - p_T^{truth}$ in the muon channel. . . . .	121
6.5	RMS of the absolute (a) and relative (b) $t\bar{t}$ mass reconstruction discrepancy $m^{reco} - m^{truth}$ in the electron channel. . . . .	121
6.6	RMS of the absolute (a) and relative (b) $t\bar{t}$ mass reconstruction discrepancy $m^{reco} - m^{truth}$ in the muon channel. . . . .	122
6.7	RMS of the absolute (a) and relative (b) $t\bar{t}$ rapidity recon- struction discrepancy $Y^{reco} - Y^{truth}$ in the electron channel. . .	122
6.8	RMS of the absolute (a) and relative (b) $t\bar{t}$ rapidity recon- struction discrepancy $Y^{reco} - Y^{truth}$ in the muon channel. . . .	122
6.9	Efficiency for the $t\bar{t}$ $p_T$ variable without any likelihood require- ment (red) and requiring $\log \mathcal{L} > -52$ (blue) in the electron channel (a) and in the muon channel (b). . . . .	123

## LIST OF FIGURES

---

6.10	$t\bar{t}$ mass spectra in the electron (a) and muon (b) channel after the one-tag selection. . . . .	124
6.11	$t\bar{t}$ $p_T$ spectra in the electron (a) and muon (b) channel after the one-tag selection. . . . .	125
6.12	$t\bar{t}$ rapidity spectra in the electron (a) and muon (b) channel after the one-tag selection. . . . .	125
6.13	Migration matrices for $m_{t\bar{t}}$ without likelihood cut (right) and with likelihood cut (left) for the electron (top) and muon (bottom) after the one-tag selection. . . . .	132
6.14	Migration matrices for $p_{T,t\bar{t}}$ without likelihood cut (right) and with likelihood cut (left) for the electron (top) and muon (bottom) after the one-tag selection. . . . .	133
6.15	Migration matrices for $Y_{t\bar{t}}$ without likelihood cut (right) and with likelihood cut (left) for the electron (top) and muon (bottom) after the one-tag selection. . . . .	134
6.16	Efficiency for the $t\bar{t}$ mass for the electron (a) and muon (b) channel, in the one-tag selection. . . . .	134
6.17	Efficiency for the $t\bar{t}$ $p_T$ for the electron (a) and muon (b) channel, in the one-tag selection. . . . .	135
6.18	Efficiency for the $t\bar{t}$ rapidity for the electron (a) and muon (b) channel, in the one-tag selection. . . . .	135
6.19	$\frac{1}{\sigma} \frac{d\sigma}{dM}$ spectra in the electron (a) and muon (b), unfolded using the SVD method with regularization parameter $k = 3$ . . . . .	139
6.20	$\frac{1}{\sigma} \frac{d\sigma}{dM}$ spectra in the electron (a) and muon (b), unfolded using the inversion method. . . . .	140

6.21	Normalized differential $t\bar{t}$ production cross section as a function of the mass of the system for the combined sample, unfolded using the SVD method. . . . .	141
6.22	Normalized differential $t\bar{t}$ production cross section as a function of the mass of the system for the combined sample, unfolded using the matrix inversion method. . . . .	142
6.23	$\frac{1}{\sigma} \frac{d\sigma}{dp_T}$ spectra in the electron (a) and muon (b), unfolded using the SVD method with regularization parameter $k = 3$ . . . . .	143
6.24	$\frac{1}{\sigma} \frac{d\sigma}{dp_T}$ spectra in the electron (a) and muon (b), unfolded using the matrix inversion method. . . . .	143
6.25	Normalized differential $t\bar{t}$ production cross section as a function of the Pt of the system for the combined sample, unfolded using the SVD method. . . . .	144
6.26	Normalized differential $t\bar{t}$ production cross section as a function of the Pt of the system for the combined sample, unfolded using the matrix inversion method. . . . .	145
A.1	Jet $p_T$ spectra for the electron (a) and muon channels (a) after the one-tag selection. . . . .	153
A.2	Jet $\eta$ spectra for the electron (a) and muon channels (a) after the one-tag selection. . . . .	154
A.3	Jet $p_T$ spectra for the electron (a) and muon channels (a) after the one-tag selection. . . . .	154
A.4	lepton $p_T$ spectra for the electron (a) and muon channels (a) after the one-tag selection. . . . .	155
A.5	lepton $\eta$ spectra for the electron (a) and muon channels (a) after the one-tag selection. . . . .	155

## LIST OF FIGURES

---

A.6	lepton $p_T$ spectra for the electron (a) and muon channels (a) after the one-tag selection. . . . .	156
A.7	Missing transverse momentum spectra for the electron (a) and muon (b) channel after the one-tag selection. . . . .	157
A.8	$W$ transverse mass (defined in (5.1)) spectra for the electron (a) and muon (b) channel after the one-tag selection. . . . .	157
A.9	$\Delta\phi(\cancel{E}_T, \mathbf{p}_T^{lepton})$ spectra for the electron (a) and muon (b) channel after the one-tag selection. . . . .	158
C.1	Kinematic fit likelihood distribution in the two-tags sample for the electron channel (a) and muon channel (a). . . . .	170
C.2	$t\bar{t}$ mass spectra in the electron (a) and muon (b) channel after the two-tags selection. . . . .	171
C.3	$t\bar{t}$ $p_T$ spectra in the electron (a) and muon (b) channel after the two-tags selection. . . . .	171
C.4	$t\bar{t}$ rapidity spectra in the electron (a) and muon (b) channel after the two-tags selection. . . . .	172
C.5	Migration matrices for $m_{t\bar{t}}$ after the two-tags selection . . . . .	173
C.6	Migration matrices for $p_{T,t\bar{t}}$ after the two-tags selection . . . . .	174
C.7	Migration matrices for $Y_{t\bar{t}}$ after the two-tags selection . . . . .	175
C.8	Efficiency for the $t\bar{t}$ mass in the two tags selection . . . . .	175
C.9	Efficiency for the $t\bar{t}$ $p_T$ in the two-tags selection . . . . .	176
C.10	Efficiency for the $t\bar{t}$ rapidity in the two tags selection . . . . .	176
C.11	Normalized differential $t\bar{t}$ production cross section as a function of the mass of the system for the combined sample after the two-tags selection, unfolded using the SVD method. . . . .	178

C.12 Normalized differential $t\bar{t}$ production cross section as a function of the Pt of the system for the combined sample after the two-tags selection, unfolded using the SVD method. . . . .	180
---	-----



---

## LIST OF TABLES

1.1	Expected single top quark production cross sections at $\sqrt{s} = 7\text{ TeV}$ . . . . .	16
1.2	Top decay branching ratios in the SM quarks. . . . .	16
1.3	$W$ boson decay modes. . . . .	18
2.1	Summary of the main characteristics of the three ATLAS ID sub-detectors. . . . .	33
2.2	Nominal detector performance specifics and coverage for the ATLAS calorimetric system. . . . .	39
3.1	The luminosity delivered by LHC divided per data period for the 2011 data taking. . . . .	47
3.2	Features and differences between the ME and PS generators. . . . .	52
3.3	$t\bar{t}$ samples which do not include all hadronic decays (No full-had). The 105200 sample is used for the nominal analysis, the others are used for systematic evaluation. . . . .	54
3.4	Single top samples. . . . .	54

## LIST OF TABLES

---

3.5	$Z/\gamma^*$ +jets samples with phase space cuts $10 \text{ GeV} < m_{ll} < 40 \text{ GeV}$ (left) and $m_{ll} > 40 \text{ GeV}$ (right). . . . .	55
3.6	Samples including $W$ + light jets, $W$ + charm (mass-less charm) and $W$ + $bb$ (where the $bb$ pair is produced in the parton shower). . . . .	56
3.7	Samples including $W$ + heavy quarks ( $c$ and $b$ ). “Inclusive” means that the $W$ can decay in either an electron, muon or tauon and a neutrino . . . . .	56
3.8	Samples including $WW/WZ/ZZ$ , filtered requiring one lepton with $p_T > 10 \text{ GeV}$ and $ \eta  < 2.8$ . . . . .	57
3.9	Binning definition in $p_T - \eta$ space for the determination of $\epsilon_{real/fake}$ . . . . .	67
3.10	Heavy flavor fraction in the $W$ +jets sample for the 2011 dataset. . . . .	72
3.11	Main uncertainties on the heavy flavor fraction in the $W$ +jets sample for the 2011 dataset. . . . .	73
5.1	Event yield in the two channels (electron and muon) in the pretag (no $b$ -tag requirement) and one tag selection. The $t\bar{t}$ generator used is Mc@NLO. . . . .	103
6.1	Binning choice for the $d\sigma/dX$ ( $X$ being the $p_T$ , mass, rapidity of the $t\bar{t}$ system and $p_T$ of the individual top) measurement. . . . .	124
6.2	Normalized differential $t\bar{t}$ production cross section as a function of the mass of the system, unfolded using the SVD method with regularization parameter $k = 3$ . . . . .	139
6.3	Normalized differential $t\bar{t}$ production cross section as a function of the mass of the system, unfolded using the simple matrix inversion method. . . . .	139

6.4	Normalized differential $t\bar{t}$ production cross section as a function of the $P_t$ of the system, unfolded using the SVD method with regularization parameter $k = 3$ . . . . .	141
6.5	Normalized differential $t\bar{t}$ production cross section as a function of the $P_t$ of the system, unfolded using the simple matrix inversion method. . . . .	142
6.6	Normalized differential $t\bar{t}$ production cross section as a function of the Rapidity of the system, unfolded using the SVD method with regularization parameter $k = 3$ . . . . .	146
6.7	Normalized differential $t\bar{t}$ production cross section as a function of the Rapidity of the system, unfolded using the simple matrix inversion method. . . . .	147
B.1	Systematic uncertainties for the normalized differential cross section with respect the mass of the system in the electron channel, using the SVD unfolding method with $k = 3$ . . . . .	160
B.2	Systematic uncertainties for the normalized differential cross section with respect the mass of the system in the muon channel, using the SVD unfolding method with $k = 3$ . . . . .	160
B.3	Systematic uncertainties for the normalized differential cross section with respect the mass of the system in the lepton ( $e$ or $\mu$ ) + jets channel, using the SVD unfolding method with $k = 3$ . . . . .	161
B.4	Systematic uncertainties for the normalized differential cross section with respect the mass of the system in the electron channel, using the simple inversion unfolding method. . . . .	161

## LIST OF TABLES

---

B.5	Systematic uncertainties for the normalized differential cross section with respect the mass of the system in the muon channel, using the simple inversion unfolding method. . . . .	162
B.6	Systematic uncertainties for the normalized differential cross section with respect the mass of the system in the lepton ( $e$ or $\mu$ ) + jets channel, using the simple inversion unfolding method. . . . .	162
B.7	Systematic uncertainties for the normalized differential cross section with respect the Pt of the system in the electron channel, using the SVD unfolding method with $k = 3$ . . . . .	163
B.8	Systematic uncertainties for the normalized differential cross section with respect the Pt of the system in the muon channel, using the SVD unfolding method with $k = 3$ . . . . .	163
B.9	Systematic uncertainties for the normalized differential cross section with respect the Pt of the system in the lepton ( $e$ or $\mu$ ) + jets channel, using the SVD unfolding method with $k = 3$ . . . . .	164
B.10	Systematic uncertainties for the normalized differential cross section with respect the Pt of the system in the electron channel, using the simple inversion unfolding method. . . . .	164
B.11	Systematic uncertainties for the normalized differential cross section with respect the Pt of the system in the muon channel, using the simple inversion unfolding method. . . . .	164
B.12	Systematic uncertainties for the normalized differential cross section with respect the Pt of the system in the lepton ( $e$ or $\mu$ ) + jets channel, using the simple inversion unfolding method.	165

B.13 Systematic uncertainties for the normalized differential cross section with respect the Rapidity of the system in the electron channel, using the SVD unfolding method with  $k = 3$ . . . . . 165

B.14 Systematic uncertainties for the normalized differential cross section with respect the Rapidity of the system in the muon channel, using the SVD unfolding method with  $k = 3$ . . . . . 166

B.15 Systematic uncertainties for the normalized differential cross section with respect the Rapidity of the system in the lepton ( $e$  or  $mu$ ) + jets channel, using the SVD unfolding method with  $k = 3$ . . . . . 166

B.16 Systematic uncertainties for the normalized differential cross section with respect the Rapidity of the system in the electron channel, using the simple inversion unfolding method. . . . . 167

B.17 Systematic uncertainties for the normalized differential cross section with respect the Rapidity of the system in the muon channel, using the simple inversion unfolding method. . . . . 167

B.18 Systematic uncertainties for the normalized differential cross section with respect the Rapidity of the system in the lepton ( $e$  or  $mu$ ) + jets channel, using the simple inversion unfolding method. . . . . 168

C.1 Normalized differential  $t\bar{t}$  production cross section as a function of the mass of the system, unfolded using the SVD method with regularization parameter  $k = 3$ . . . . . 177

C.2 Normalized differential  $t\bar{t}$  production cross section as a function of the Pt of the system, unfolded using the SVD method with regularization parameter  $k = 3$ . . . . . 179

## LIST OF TABLES

---

C.3	Normalized differential $t\bar{t}$ production cross section as a function of the rapidity of the system, unfolded using the SVD method with regularization parameter $k = 3$ . . . . .	181
-----	--	-----

---

## BIBLIOGRAPHY

- [1] M. GELL-MANN, *Phys. Lett.* **8**, 214 (1964).
- [2] G. ZWEIG, *CERN-TH-401* (1964).
- [3] S. GLASHOW, *Nucl. Phys.* **22**, 579 (1961).
- [4] S. WEINBERG, *Phys. Rev. Lett.* **19**, 1264 (1967).
- [5] A. SALAM, Weak and electromagnetic interactions, in *Proc. of the 8th Nobel Symposium on "Elementary Particle Theory, Relativistic Groups and Analyticity", Stockholm, Sweden, 1968*, edited by N. SVARTHOLM, p. 367, 1969.
- [6] P. W. HIGGS, *Phys. Rev. Lett.* **13**, 508 (1964).
- [7] N. CABIBBO, *Phys. Rev. Lett.* **10**, 531 (1963).
- [8] M. KOBAYASHI and T. MASKAWA, *Progress of Theoretical Physics* **49**, 652 (1973).
- [9] J. BERINGER et al., *Phys. Rev. D* **86**, 010001 (2012).

## BIBLIOGRAPHY

---

- [10] T. AALTONEN et al., *Phys. Rev. Lett.* **103**, 092002 (2009).
- [11] V. M. ABAZOV et al., *Phys. Rev. D* **84**, 112001 (2011).
- [12] ATLAS COLLABORATION, Measurement of the t-channel single top-quark production cross section in pp collisions at  $\sqrt{s} = 7$  TeV with the ATLAS detector, Submitted and accepted, 2012.
- [13] S. CHATRCHYAN et al., *Phys.Rev.Lett.* **107**, 091802 (2011).
- [14] B. PONTECORVO, *Sov. Phys. JETP* **26**, 984 (1968).
- [15] Z. MAKI, M. NAKAGAWA, and S. SAKATA, *Prog. Theor. Phys.* **28**, 870 (1962).
- [16] G. AAD et al., *Phys. Lett. B* **716**, 1 (2012).
- [17] S. CHATRCHYAN et al., *Phys. Lett. B* **716**, 30 (2012).
- [18] F. ABE et al., *Phys. Rev. Lett.* **74**, 2626 (1995).
- [19] S. ABACHI et al., *Phys. Rev. Lett.* **74**, 2632 (1995).
- [20] D. SOPER, *Nucl. Phys. Proc. Suppl.* **53**, 69 (1997).
- [21] J. COLLINS, *J. of Physics G* **17**, 1547 (1991).
- [22] A. MARTIN, W. STIRLING, R. THORNE, and G. WATT, *Phys. Lett.* **B652**, 292 (2007).
- [23] J. PUMPLIN, D. STUMP, J. HUSTON, H. LAI, P. M. NADOLSKY, et al., *JHEP* **0207**, 012 (2002).
- [24] U. LANGENFELD, S. MOCH, and P. UWER, New results for t anti-t production at hadron colliders, arXiv:hep-ex/0205019 [hep-ex], 2009.

- [25] H.-L. LAI et al., *Phys.Rev.* **D82**, 074024 (2010).
- [26] S. FRIXIONE, S. LAENEN, P. MOTYLINSKI, C. WHITE, and B. WEBBER, *Journal of High Energy Physics* **2008**, 029 (2008).
- [27] C. WHITE, S. FRIXIONE, E. LAENEN, and F. MALTONI, *Journal of High Energy Physics* **2009**, 074 (2009).
- [28] N. KIDONAKIS, *Phys. Rev.* **D83**, 091503 (2011).
- [29] N. KIDONAKIS, *Phys. Rev.* **D82**, 054018 (2010).
- [30] N. KIDONAKIS, *Phys. Rev.* **D81**, 054028 (2010).
- [31] A. QUADT, *Eur. Phys. J. C* **48**, 835 (2006).
- [32] Combination of CDF and D0 results on the mass of the top quark using up to 5.8 fb<sup>-1</sup> of data, Technical Report FERMILAB-TM-2504-E, 2011.
- [33] Combination of ATLAS and CMS results on the mass of the top quark using up to 4.9 fb<sup>-1</sup> of data, Technical Report ATLAS-CONF-2012-095, CERN, Geneva, 2012.
- [34] Precision Electroweak Measurements and Constraints on the Standard Model, Technical Report CERN-PH-EP-2008-020, 2008.
- [35] L. R. EVANS and P. BRYANT, *J. Instrum.* **3**, S08001. 164 p (2008), This report is an abridged version of the LHC Design Report (CERN-2004-003).
- [36] THE ATLAS COLLABORATION, *Journal of Instrumentation* **3**, S08003 (2008).

## BIBLIOGRAPHY

---

- [37] THE CMS COLLABORATION, *Journal of Instrumentation* **3**, S08004 (2008).
- [38] THE LHCb COLLABORATION, *Journal of Instrumentation* **3**, S08005 (2008).
- [39] THE ALICE COLLABORATION, *Journal of Instrumentation* **3**, S08002 (2008).
- [40] THE ATLAS COLLABORATION, *ATLAS detector and physics performance: Technical Design Report, 1*, Technical Design Report ATLAS, CERN, Geneva, 1999, <http://cdsweb.cern.ch/record/391176/>.
- [41] THE ATLAS COLLABORATION, *ATLAS detector and physics performance: Technical Design Report, 2*, Technical Design Report ATLAS, CERN, Geneva, 1999, <http://cdsweb.cern.ch/record/391177/>.
- [42] THE ATLAS COLLABORATION, *European Physical Journal C* **70**, 875 (2010).
- [43] Luminosity Determination Using the ATLAS Detector, Technical Report ATLAS-CONF-2010-060, CERN, Geneva, 2010.
- [44] Luminosity Determination in pp Collisions at  $\sqrt{s} = 7$  TeV using the ATLAS Detector in 2011, Technical Report ATLAS-CONF-2011-116, CERN, Geneva, 2011.
- [45] B. P. KERSEVAN and E. RICHTER-WAS, *Comput.Phys.Commun.* **149**, 142 (2003).
- [46] M. MANGANO et al., *JHEP* **0307**, 001 (2003).
- [47] S. FRIXIONE and B. WEBBER, *JHEP* **0206**, 029 (2002).

- [48] S. FRIXIONE, P. NASON, and B. WEBBER, *JHEP* **0308**, 007 (2003).
- [49] S. FRIXIONE, P. NASON, and C. OLEARI, *JHEP* **0711**, 070 (2007).
- [50] T. SJOSTRAND et al., *Comput.Phys.Commun.* **135**, 238 (2001).
- [51] G. CORCELLA et al., *JHEP* **0101**, 010 (2001).
- [52] J. BUTTERWORTH and J. FORSHAW, *Journal of Physics G* **19**, 1657 (1993).
- [53] M. DOBBS et al., Les Houches guidebook to Monte Carlo generators for hadron collider physics, 2004.
- [54] B. WEBBER, Parton shower Monte Carlo event generators, 2011.
- [55] B. ANDERSSON, *The Lund Model*, Cambridge monographs on particle physics, nuclear physics, and cosmology, Cambridge Univ. Press, Cambridge, 1998.
- [56] M. MANGANO et al., Matching parton showers and matrix elements, 2006, arXiv:hep-ph/0602031.
- [57] S. AGOSTINELLI et al., *Nuclear Instruments and Methods in Physics Research A* **506**, 250 (2003).
- [58] THE ATLAS COLLABORATION, *European Physical Journal C* **70**, 823 (2010).
- [59] M. ALIEV et al., *Computer Physics Communications* **182**, 1034 (2011).
- [60] S. ALLWOOD-SPIRES et al., Monte Carlo samples used for top physics, Technical Report ATL-PHYS-INT-2010-132, CERN, Geneva, 2010.

## BIBLIOGRAPHY

---

- [61] J. ALWALL, M. HERQUET, F. MALTONI, O. MATTELAER, and T. STELZER, *JHEP* **1106**, 128 (2011).
- [62] P. SKANDS, *Phys.Rev.* **D82**, 074018 (2010).
- [63] V. ABAZOV et al., *Phys.Rev.* **D76**, 092007 (2007).
- [64] THE ATLAS COLLABORATION, *JHEP* **1205**, 059 (2012).
- [65] C.-H. KOM and W. STIRLING, *Eur.Phys.J.* **C69**, 67 (2010).
- [66] B. ACHARYA et al., Object selection and calibration, background estimations and MC samples for the Autumn 2012 Top Quark analyses with 2011 data, Technical Report ATL-COM-PHYS-2012-1197, CERN, Geneva, 2012.
- [67] M. CACCIARI, G. SALAM, and G. SOYEZ, *Journal of High Energy Physics* **2008**, 063 (2008).
- [68] Calibrating the b-Tag Efficiency and Mistag Rate in 35 pb<sup>-1</sup> of Data with the ATLAS Detector, Technical Report ATLAS-CONF-2011-089, CERN, Geneva, 2011.
- [69] W. LAMPL et al., Calorimeter Clustering Algorithms: Description and Performance, Technical Report ATL-LARG-PUB-2008-002. ATL-COM-LARG-2008-003, CERN, Geneva, 2008.
- [70] S. HASSANI et al., *Nuclear Instruments and Methods in Physics Research A* **572**, 77 (2007).
- [71] T. LAGOURI et al., *IEEE Transactions on Nuclear Science* **51**, 3030 (2004).

- [72] THE ATLAS COLLABORATION, *The European Physical Journal C* **72**, 1 (2012).
- [73] M. BOTJE et al., (2011), arXiv:hep-ph/1101.0538 [hep-ph].
- [74] Measuring the b-tag efficiency in a top-pair sample with 4.7/fb of data from the ATLAS detector, Technical Report ATLAS-CONF-2012-097, CERN, Geneva, 2012.
- [75] Measurement of the Mistag Rate with 5 /fb of Data Collected by the ATLAS Detector, Technical Report ATLAS-CONF-2012-040, CERN, Geneva, 2012.
- [76] THE ATLAS COLLABORATION, *Eur.Phys.J.* **C72**, 2039 (2012).
- [77] THE ATLAS COLLABORATION, Measurements of top quark pair relative differential cross-sections with ATLAS in  $pp$  collisions at  $\sqrt{s} = 7$  TeV, 2012, arXiv:1207.5644[hep-ex]. Accepted by EPJC.
- [78] G. D'AGOSTINI, *Nuclear Instruments and Methods in Physics Research Section A* **362**, 487 (1995).
- [79] A. HOCKER and V. KARTVELISHVILI, *Nucl.Instrum.Meth.* **A372**, 469 (1996).
- [80] J. CAMPBELL and R. ELLIS, *Nucl.Phys.Proc.Suppl.* **205-206**, 10 (2010).